Displacement and Geometrical Characteristics of Earthquake Surface Ruptures: Issues and Implications for Seismic Hazard Analysis and the Process of the Earthquake Rupture.

Steven G. Wesnousky
Center for Neotectonic Studies
Mail Stop 169
University of Nevada, Reno
Reno, Nevada 89557
stevew@seismo.unr.edu

Abstract

There now exist about 3 dozen historical earthquakes for which investigators have constructed maps of earthquake rupture traces accompanied by data describing the coseismic slip observed along fault strike. The compilation of that data presented here places observational bounds on aspects of both seismic hazard analysis as well as fault mechanics. Analysis leads to an initial statistical basis to predict the endpoints of rupture and the amount of surface slip expected at sites along strike during earthquakes on mapped faults. The observations also give support to the ideas that there exists a process zone or volume of about 3-4 km dimension at the fronts of large laterally propagating earthquake ruptures within which stress changes may be sufficient to trigger slip on adjacent faults, and that the ultimate length of earthquake ruptures is controlled primarily by the geometrical complexity of fault traces and variations in accumulated stress levels along faults that arise due to the location of past earthquakes. To this may be added the observation that the form of earthquake surface slip distributions is better described by asymmetric rather than symmetric curve forms and that earthquake epicenters do not appear to correlate in any systematic manner to regions of maximum surface slip observed along strike.

Introduction

It has become standard practice since *Clark*'s [1972] early study of the 1968 Borrego Mountain earthquake to map the geometry of rupture traces and assess the surface-slip distribution of large earthquakes that break the ground surface. The results of such studies have been a constant source of reference and use in development of seismic

hazard methodologies [*Frankel et al.*, 2002; *Petersen and Wesnousky*, 1994; *SCEC*, 1994; *Wesnousky*, 1986; *Wesnousky et al.*, 1984], engineering design criteria for critical facilities [*Fuis and Wald*, 2003; *Kramer*, 1996; *Pezzopane and Dawson*, 1996], and development and discussion of mechanical models to understand physical factors that control the dynamics of the earthquake source as well as the resulting strong ground motions [*Bodin and Brune*, 1996; *Heaton*, 1990; *King and Wesnousky*, 2007; *Romanowicz*, 1994; *Scholz*, 1982a; 1982b; *Scholz*, 1994]. There now exist about 3 dozen historical earthquakes for which investigators have constructed maps of earthquake rupture traces accompanied by data describing the coseismic slip observed along fault strike. Here I put forth a compilation of that data set with the aim of placing observational bounds on aspects of seismic hazard analysis and fault mechanics.

Data Set

I limit my attention to the larger surface rupture earthquakes of length dimension greater than about 15 km and for which there exist both maps and measurements of coseismic offset along strike of the rupture (**Table 1**). The map and slip distribution of the April 8, 1968 M6.4 Borrego Mountain earthquake of California illustrate the manner of data compilation (**Figure 1**). The surface slip distribution is placed below and at the same map scale as the map of the surface rupture trace. Nearby active fault traces that did not rupture during the earthquake are also shown. The location and dimension of fault steps along and at the ends of the earthquake ruptures and the distances to nearest neighboring active fault traces from the endpoints of surface rupture traces are annotated. The size of steps in fault trace are generally taken as the distance between en-echelon strands measured perpendicular to average fault strike. Steps in fault trace are also labeled as restraining or releasing depending on whether volumetric changes within the step resulting from fault slip would produce contractional or dilational strains within the steps, respectively [e.g. *Segall and Pollard*, 1980]. The epicenter of the earthquake is also shown by a star. The maps and slip distributions for all the earthquakes in **Table 1** are presented in the same manner and collected in **Appendix 1**. The resolution of the available maps generally limits observations to discontinuities of about 1 km and greater.

I have digitized and linearly interpolated between each of the original points in the slip distributions to form slip distribution curves at a resolution sufficient to reflect

the details of the original slip measurements, at either 0.1 km or 1 km intervals (e.g. **Figure 1**). The original and interpolated points of the slip curves for all earthquakes in **Table 1** are presented both graphically and in tabular form in **Appendix 2**.

The seismic moment Mo = μLWS is used here as the primary measure of earthquake size, where μ = crustal rigidity of the rocks in which the earthquake occurs, L and W are the length and width of the fault plane producing the earthquake, and S = average coseismic slip during the earthquake [*Aki and Richards*, 1980]. The value of Mo may be determined from seismological or geodetic measures of seismic waves or ground deformations resulting from an earthquake, respectively. In such analyses, the value of rigidity μ is assumed independently from seismic velocity models that describe the crust in the vicinity of the earthquake source, and the depth D to which rupture extends is generally assigned as the depth of aftershocks or regional background seismicity. The value Mo may also be determined primarily from geological observations where estimates of S and L have been obtained from field measurements of offsets along the surface expression of the causative fault. In this case, the measurement is limited to earthquakes large enough to break the ground surface and to those for which independently derived values of μ and W can be drawn from seismological observations. For convenience of discussion, estimates of Mo determined in this latter manner are here labeled Mo^{G} and referred to as geologic moments. Similarly, estimates of moment derived primarily from instrumental measurements are denoted Mo^{inst}.

The estimates of geologic moment Mo^{G} and the parameters from which the estimates are calculated are listed for each event in **Table 1**. Specifically, the digitized slip curves (**Figure 1 and Appendix 2**) are used to calculate the average S and maximum S^{max} coseismic surface slip and rupture length L for each listed event. The investigations on which values of the depth extent of rupture D, the rigidity μ, and fault type (mechanism and dip δ) used to estimate the respective geologic moments are also referenced in **Table 1.** The basis for assigning the values of μ and rupture depth D for the respective earthquakes are described in further detail in the notes of **Table 1**. The value of rupture width W used in calculating Mo^{G} is D/sin(δ), where δ is depth and listed in the *Type* column. Because of uncertainties in estimates of μ used in seismic moment calculations, it has been suggested that geometrical moment or seismic potency (Po =

Mo/μ) may provide a more fundamental scaling parameter for comparing the relative size of earthquakes [*Ben-Menahem and Singh*, 1981; *Ben-zion*, 2001]. To examine this idea, I calculate and list a value Po for each event.

Instrumentally derived estimates of the seismic moment Mo^{inst} of each event are when available listed in **Table 2**. The sources of the estimates are cited and each denoted according to whether it was derived from seismic body-waves, surface waves, or geodetic measurements. For each, I have also attempted to extract the value of rigidity μ used by investigators in calculating the seismic moment values. The values of rigidity μ are then used to convert the measures of seismic moment to potency Po. The original references and notes describing the basis for the values of rigidity used in each of the moment calculations are provided in the notes accompanying **Table 1**. It is these data that are also the basis for the values of μ used in calculating the geologic moments of the respective earthquakes in **Table 1**.

Observations

The data set is limited to continental earthquakes. Thirty-seven earthquakes are listed in **Table 1**. Twenty-two are primarily strike-slip, 7 are normal, and the remaining 8 are reverse. The following section presents the observations summarized in **Tables 1** and **2** graphically. The plots are designed to illustrate how variables in the data set scale with one another. Curves are fit when applicable to the observations to quantify the relationships. For each plot the type of curve (e.g. linear, log-linear, power-law), the parameters leading to the best fit of the curve to the data, and the number of data points are defined within the plot space. The quality of curve fits are also variously described by values of Pearson's regression coefficient R, Chi-square, and standard deviation [*Press et al.*, 1992].

Fault Width and Aspect Ratio

Rupture width W is plotted versus surface rupture length and both the geologic and instrumental moment in **Figures 2**. Each plot shows the widths of strike-slip ruptures are generally assigned values between 10 and 15 km, the width of the seismogenic layer in continental environments, and appear independent of rupture length. Because normal faults dip through the seismogenic layer the rupture widths tend to be larger and reach

~20 km width, with the exception of the 1987 Edgecumbe earthquake (event 27) which occurred in the Taupo Zone of New Zealand, a region of particularly high heat flow [e.g., *Rowland and Sibson*, 2004]. The range of fault widths is greater for reverse faults, ranging from about 5 to 20 km. Three of the 8 reverse faults in the data set occurred in the intraplate environment of Australia (events 19, 23, and 26) where rupture depths have been observed to be particularly shallow [*Choy and Bowman*, 1990; *Fredrich et al*., 1988; *Langston*, 1987]. The Australian intraplate events define the lower end of the range in both W and L and appear responsible for the apparent positive relationship between L and W.

The same data are recast in a plots of the aspect ratio (rupture length L / rupture width W) versus rupture length in **Figure 3a**. The best-fitting curve of form Aspect Ratio = A * L^B to the strike-slip data is characterized by a value of B=1, indicating a linear relationship between aspect ratio and rupture length, and that which would be expected by limiting the depth extent of earthquake ruptures to a seismogenic layer of relatively constant thickness. The normal fault ruptures are similarly characterized but tend to fall below the strike-slip events. This latter difference arises because the events share a seismogenic layer of about the same thickness but the normal faults dip through the layer in contrast to the vertical planes of strike-slip ruptures. The reverse fault data show a similar tendency for aspect ratio to increase with length but the scatter in the fewer data yield a poorly fit regression. The aspect ratio is also plotted and similarly fit to regression curves as a function of Mo^G and Mo^{inst} in **Figures 3b and c**, respectively. In these cases, the same patterns arise but the increased scatter in the data leads to poorer curve fits. The greater scatter is because estimates of Mo also incorporate uncertainties and variations in estimates of coseismic displacement S and rigidity μ between the respective earthquakes. The comparison of Mo^G to aspect ratio in **Figure 3b** is somewhat circular in reasoning in that both Mo^G and aspect ratio are functions of L. Nonetheless, limiting comparison of rupture length to instrumental moment Mo^{inst} does not appear to significantly decrease the scatter in the relationship (**Figure 3c**).

Instrumental vs. Geologic Measures of Earthquake Size: Moment and Potency

The range of instrumentally derived values of seismic moment Mo^{inst} and potency Po^{inst} generally span a range of a factor of 2 to 3 for the earthquakes listed in **Table 2**

(Figure 4). Geological estimates of Mo^G generally fall within the range of instrumental estimates for the larger events in the data set (**Figure 4**). The same is also illustrated in **Figures 5** where the geologic estimates of seismic moment and potency are plotted as a function of the instrumentally derived values for the respective events. A solid line of slope 1 is drawn on each plot. The bounding dashed parallel lines fall a factor of 2 in geologic moment from the line of slope 1. Data points falling on the solid line of slope 1 would indicate perfect agreement between the geological and instrumental measures. The vertical error bars with each data point span a factor of 3 about the value of geologic moment. The horizontal error bars for each data point encompass the spread of instrumentally derived values given for each event and plotted in **Figure 4**. The majority of the geologic estimates fall within a factor of 2 of the instrumental measures. Those with the greatest discrepancy tend to fall well below the respective instrumental measures, indicating that coseismic slip was probably concentrated at depth for the particular events. For only one event, the 1915 Pleasant Valley earthquake (event 5), do the geologic estimates fall well above the instrumental estimates. *Doser* [1988] points out the discrepancy may be due in part to problems in instrumental magnification or that energy release during that earthquake occurred at longer periods than recorded by the few seismograms available for analysis of the event.

Maximum versus Average Coseismic Slip

The ratio of the average to maximum values of slip listed in **Table 1** are plotted as a function of event number and rupture length in **Figure 6**. The ratio for all events regardless of mechanism is characterized by an average value of 0.41 with a standard deviation of 0.14. The subsets of strike-slip, reverse and normal mechanisms show ratios of 0.44±.14, 0.35±.11, and 0.34±.10, respectively (**Figure 6b**). No clear dependence of the ratio on rupture length is observed.

Coseismic Slip versus Rupture Length (Average and Maximum)

The average and maximum values of coseismic slip as a function of surface rupture length are shown in **Figures 7**. Linear curve fits are applied separately to each of the reverse, normal, and strike-slip earthquakes. The slopes of the linear curve fits are increasingly greater for the strike-slip, normal, and reverse faults, respectively. While the reverse and normal fault observations appear reasonably well-fit by a straight line, the

strike-slip data are not. For this reason, I have further fit log-linear [slip S (m)=-C + C * Log (Length(km)] and power law [slip S (m)= C * Length(km)^D] curves to the strike-slip data. The log-linear fit is formulated to constrain the curve to intersect the point where both L and S are zero. These latter curves result in a significant reduction in formal uncertainties of the curve fit to the strike-slip data as compared to a straight line. The formal measures of uncertainty for the power-law and log-linear curve fits are virtually equal. The slopes of the lines describing the increase of slip show a decrease in slope as a function of rupture length without apparently reaching a plateau.

Instrumental Moment and Moment-Magnitude Versus Rupture Length

Figure 8 shows the relationships of Moment Mo and moment-magnitude Mw to rupture length L for the subset of events studied by instrumental means. Each shows a systematic increase with rupture length though with significant scatter when viewing the entirety of the data set. The fewer number of observations and limited range of rupture lengths is viewed insufficient to lend confidence to similar regressions for the subset of normal and reverse earthquakes as compared to strike-slip earthquakes.

Shape of Surface Slip Distributions

To examine whether or not earthquake surface slip distributions are characterized by any regularities in shape I have fit various regression curves to the digitized slip distributions of the earthquakes listed in **Table 1**. The approach is illustrated in **Figure 9** where 3 of the digitized surface slip distributions are displayed along with a set of 6 best-fit regression curves. The simplest curve form is that of a *flat line* and yields the average displacement of the slip distribution. Additionally curves of the form of a *sine* and *ellipse* are fit to the data. In these latter cases the length is defined by the length of the surface rupture, the curve-fits by form are symmetric, and the only free variable in fitting the curves to the observed slip distribution is the amplitude or maximum slip of the curve. Finally I fit 3 curves allowing the shape of the fit to be asymmetric. These include a *triangle*, an *asymmetric sine*, and an *asymmetric ellipse* curve. The asymmetric sine and ellipse curves are defined by the shapes of the respective functions multiplied by a value $(1 - m * (x/L))$ where x is the distance along the fault, L is the rupture length, and m is a variable of regression. The value modifies the sine and ellipse functions in a manner that

reduces the amplitude in a linear manner as a function of distance along the slip curve. In each of the asymmetric curve fits there are then two variables of regression. For the triangle the two variables of regression may be viewed as the slopes of the two lines that form the triangle, and it is the parameter *m* and the amplitude of the ellipse and sine functions for the *asymmetric ellipse* and *asymmetric sine* functions. Similar plots are provided for the digitized slip distributions of all events in **Appendix 3**.

Each of the curve-fits may be characterized by a standard deviation about the predicted value. Division of the standard deviation by the average value of the surface slip distribution for the respective slip curves defines the Coefficient of Variation (COV) along fault strike. The higher the value of COV the poorer the curve-fit. The normalization by the average slip provides a measure of normalization that allows a more valid comparison of the quality of fit of the respective curves. The COVs of the curve fits to each slip distribution are presented for comparison in **Figure 10**. The solid symbols represent values for the asymmetric curve fits and the open symbols are values for the flat line and symmetric sine and ellipse curves. The plots show that the asymmetric functions consistently yield a better fit to the observations and the flat-line consistently yields the worst fit. Among the various asymmetric curve fits, none provide a consistently better fit to the data than the other. In sum, one may infer that surface slip distributions are in general characterized by some degree of asymmetry, with the recognition that the relatively better fit of the asymmetric functions overall is largely the result of allowing the variation of two rather than one variable in the process of fitting curves to the observations.

The asymmetry of the resulting curve functions is depicted in **Figure 11**. Asymetry is here defined as the ratio A/L, where A is the shortest distance from a rupture endpoint to the point of maximum slip (or median value of Mo in the case of **Figure 11d**) and L is the length of the rupture. It is observed that the degree of asymmetry one associates with a rupture is dependent on the shape of the curve assumed to best reflect the shape. The triangular function (**Figure 11a**) tends to often enhance or increase the apparent asymmetry as compared to the asymmetric ellipse (**Figure 11b**) and asymmetric sine functions (**Figure 11c**). The same may be said for asymmetric ellipse as compared to the asymmetric sine functions. Finally, yet generally lesser values of asymmetry are

defined when the reference to asymmetry is taken as the median value of Mo (**Figure 11d).**

Location of Epicenter in Relation to Shape of Slip Distribution

The spatial relationship of the location of earthquake epicenters to the shape of the slip distributions is illustrated with the plots in **Figure 12**. As in **Figure 11**, the asymmetry of the surface slip (solid symbols) is defined as the ratio A/L, where A is the shortest distance from a rupture endpoint to the peak slip (or median value of Mo, **Figure 12d**) and L is the respective rupture length. Additionally, the relative location of the epicenter (open symbols) is defined by the ratio E/L, where E is the distance of the epicenter from the same respective rupture endpoint used to define A. In this manner the ratio A/L is limited to between 0 and 0.5 whereas the ratio of E/L is limited between 0 and 1. The design of the plot is such that the open and closed symbols fall close together when the epicenter falls close to the maximum value of the slip function. Conversely, separation of the symbols indicates rupture initiated well away from the maximum value of the slip functions or the median value of Mo in the case of **Figure 12d**. Values of E/L (open symbols) near zero or one indicate primarily unilateral rupture. Regardless of the shape of curve-fit assumed there is not a systematic correlation of epicenter with the maximum slip value observed along strike.

Shape of Surface Slip Distribution as a Function of Rupture Length

Plots of the peak amplitudes of the various curves fit to the surface slip distributions versus rupture length shown in **Figure 13** provide another manner to characterize the shapes of the slip distributions. The plots show the same characteristics as observed in the earlier plots of surface slip versus rupture length (**Figure 7**). Specifically, the fewer number of normal and reverse earthquake data may be fit by a straight line but the strike-slip earthquakes which cover a wider range of rupture lengths cannot. The observations for the strike-slip earthquakes or the entire data set overall are better fit by a curve that decreases with slope as a function of increasing rupture length. The slope reflects the ratio of amplitude to length of the assumed slip functions. In this regard, the average shape (or ratio of dimensions) of the prescribed slip distributions is not constant, varies across the magnitude spectrum of the observed earthquakes, and thus is not self-similar.

Fault Trace Complexity and Earthquake Rupture Length

Strike-Slip earthquakes

Examining maps of the earthquake surface rupture trace and nearby active fault traces that did not rupture during the earthquake such as shown for the 1968 Borrego Mountain event (**Figure 1a**) provides a basis to examine the relationship between earthquake rupture length and fault trace complexity. The 1968 earthquake rupture for example (1) propagated across a 1.5 km restraining step, (2) stopped at a 2.5 km restraining step or 7 km releasing step at its northwestern (left) limit, and (3) died at its southeastern (right) limit in the absence of any geometrical discontinuity and at a point where the active trace can be shown to continue uninterrupted for 20 km or more past the end of the rupture. **Figure 14** is a synopsis of the relationship between the length of rupture and geometrical discontinuities for all strike-slip earthquakes listed in **Table 1** and is largely the same as presented in *Wesnousky* [2006].

The vertical axis in **Figure 14** is the dimension distance in kilometers. Each of the strike-slip earthquakes listed in **Table 1** is spaced evenly and ordered by increasing rupture length along the horizontal axis. A dotted line extends vertically from each of the labeled earthquakes. Various symbols that summarize the size and location of geometrical steps within and at the endpoints of each rupture as well as where earthquake ruptures have terminated at the ends of active faults are plotted along the dotted lines. The symbols denote the dimension (km) of steps in surface rupture traces along strike or the closest distance to the next mapped active fault from the terminus of the respective ruptures. Separate symbols are used according to whether the steps are releasing or restraining in nature, and whether they occur within (open green symbols - rupture continues through) or at the endpoints of the rupture trace (red solid symbols). In certain instances, the endpoints of rupture are not associated with a discontinuity in fault strike, in which case the endpoint of rupture is denoted by a separate symbol (open yellow circles) and annotated with the distance that the active trace continues beyond the endpoint of rupture. Because of the complexity of some ruptures and presence of subparallel and branching fault traces, some earthquakes have more than two ‘ends’. Thus in the case of the 1968 earthquake it is accordingly depicted in **Figure 14** that the fault ruptured through a 1.5 km restraining step, stopped on one end at either a 2.5 km

restraining step or 7 km releasing step, and stopped at the other end along an active trace that continues for 20 km or more in the absence of any observable discontinuity. The color scheme of symbols follows that of a conventional red-yellow-green stop light: Ruptures appear to have ended at the discontinuities colored red, jumped across the discontinuities colored green, and simply died out along strike in the absence of any discontinuities for the cases colored yellow. The observations show that about two thirds of terminations of strike-slip ruptures are associated with geometrical steps in fault trace or the termination of the active fault on which they occurred, a transition exists between step dimensions of 3 and 4 km above which rupture fronts have not been observed to propagate through, and that steps of lesser dimension ruptures appear to cease propagating only about 40% of the time (**Figure 15**).

Earthquakes of Normal Mechanism

The approach followed for strike-slip events is applied to normal type earthquakes and summarized in in **Figures 16** and **17**. The smaller data set makes it difficult to arrive at generalizations. That withstanding, the observations show the endpoints of historical normal ruptures occur at discontinuities in fault trace about 70% of the time. Historical normal fault ruptures have continued across steps in surface trace of 5 to 7 km, larger than observed for the strike-slip earthquakes.

Earthquakes of Reverse Mechanism

The data for thrust faults is limited to 8 earthquakes. Again ordered by increasing rupture length, I have plotted the discontinuities through which ruptures have propagated or stopped, respectively (**Figure 18**). There are three recorded instances of thrust ruptures propagating through mapped steps of 2 and 6 km dimension. In only one case is it clear that rupture terminated in the absence of a discontinuity at the rupture endpoint. The remaining cases appear to show termini associated with geometrical discontinuities, though in several cases and particularly for the Australian earthquakes the mapping available to me is insufficient to lend any confidence in the observation.

Implications and Applications

Seismic Hazard

Estimation of Surface Rupture Hazard

The regression curves in **Figure 7** provide an initial basis to estimate the expected amount of surface displacement during an earthquake as a function of rupture length. The values of slip plotted in **Figure 7** are derived from the digitized slip distributions for the respective events as shown in **Figure 1c**. Each average value is also characterized by a standard deviation about the average. Division of the two (standard deviation / average slip) defines the Coefficient of Variation (COV) along strike of each event. The COV provides a measure of the roughness of the surface slip distributions that is in effect normalized to rupture length. The value of the COV about the average value of slip for each event is displayed in **Figure 10**. The average of all values is also listed in the plot and equals 0.63±0.18. Given the expected rupture length of an earthquake, an average value of surface offset may be calculated from the regressions in **Figure 7**, and a standard deviation to associate with this latter estimate may in principle be calculated by multiplying the expected average slip by the COV.

The assessment of expected coseismic surface slip may be improved by assuming the surface slip is described by a particular shape such as the *sine*, *ellipse*, *triangle*, *asymmetric sine* or *asymmetric ellipse* curve forms illustrated in **Figure 9**. Assuming these curve forms consistently yields a better fit to the observed slip distributions than the average value of slip or, equivalently, a flat line (**Figure 10**). One may thus choose an alternate approach of, for example, assuming that surface slip will follow the form of a *sine* or *ellipse* function. Doing so, the amplitude of expected distribution may be estimated as a function of length using the regression curves for the *sine* and *ellipse* functions in **Figure 13d** and **13e**, respectively. Multiplication of the average value of the COV for the *sine (0.57±0.19)* and *ellipse* (0.54±0.19) curve-fits by the predicted slip at any point along the fault length yields a standard deviation that may be attached to the estimate.

The earthquake slip distributions are yet better fit by the use of curves that allow an asymmetry in the slip distribution (**Figure 10**) and further reduction in the uncertainties might be obtained by their use but for the problem that it would require

prior knowledge of the sense of asymmetry along the fault to rupture. That is knowledge that is not generally available at this time.

A more formal approach than outlined here will incorporate both the uncertainties attendant to the fitting of curves to the slip versus length data (e.g. **Figures 7 and 13**) and the estimates of the Coefficients of Variation (e.g. **Figures 9 and 10**). That said, the compilation and analysis of observations shows the feasibility of the approach, which is the main intent here.

Estimating the Length of Future Earthquake Ruptures on Mapped Faults

The distribution and lengths of active faults are generally fundamental input to assessments of seismic hazard in regions of active tectonics [e.g., *Frankel et al.*, 2002; *SCEC*, 1994]. Because the lengths of earthquake ruptures are commonly less than the entire length of the mapped fault on which they occur, the seismic hazard analyst may encounter the problem in deciding how to place limits on the probable lengths of future earthquakes on the mapped active faults. It has been noted previously that faults are not generally continuous but are commonly composed of segments that appear as steps in map view and that these discontinuities may play a controlling role in limiting the extent of earthquake ruptures. The data collected here and summarized in **Figure 14** show that about two-thirds of the endpoints of strike-slip earthquake ruptures are associated with fault steps or the termini of active fault traces (**Figure 15a**), and that there is a limiting dimension of fault step (3-4 km) above which earthquake ruptures have not propagated and below which rupture propagations cease only about 40 percent of the time (**Figure 15b**). The variability of behavior for steps of dimension less than 3-4 km in part reflects variability in the three-dimensional character of the discontinuities mapped at the surface. The effect on rupture propagation may vary between steps of equal map dimension if, for example, the subsurface structures differ or do not extend to equal depths through the seismogenic layer [e.g., *Graymer et al.*, 2006; *Simpson et al.*, 2006]. The approach and observations might be useful for placing probabilistic bounds on the expected endpoints of future earthquake ruptures on mapped active faults, given that detailed mapping of faults is available in the region of interest.

The observations are fewer for dip-slip earthquakes (**Figures 16, 17** and **18**). That withstanding, the normal earthquake rupture endpoints appear to be associated with

discontinuities in mapped fault trace at about the same ~70% frequency as observed for the strike-slip earthquakes (**Figure 17**). The data are too few to draw an analogous generalization from the small number of reverse fault earthquakes. A comparison of the dip-slip (**Figure 16**) to strike-slip earthquakes (**Figure 14**) shows the dip-slip events to have ruptured through steps in map trace of 5-7 km, greater than observed for strike-slip earthquakes. The larger value may simply reflect the dipping nature of the faults.

Mechanics of the Rupture Process

Slip versus Length: Physical Implications

Theoretical models of fault displacements in an elastic medium predict that the stress drop $\Delta\sigma$ resulting from slip S on a fault is of the form $\Delta\sigma \cong C*S/W$, where W is the shortest dimension across the fault area and C is a shape factor generally near unity [e.g., *Kanamori and Anderson*, 1975]. Analyses of instrumental recordings of earthquakes have been the basis to interpret that stress drops for earthquakes are relatively constant and limited to between 10 and 100 bars over the entire spectrum of observed earthquake sizes [*Hanks*, 1977; *Kanamori and Anderson*, 1975]. It is generally assumed that the limiting depth of coseismic slip is reflected equal to the depth extent of aftershocks or background seismicity in the vicinity of the earthquakes. The earthquakes of **Table 1** share a similar seismogenic depth of about 12-15 km (**Figure 2**). It follows that earthquakes of constant stress drop and rupture width will share a similar ratio of S/W. The systematic increase in displacement S with rupture length observed in **Figure 7** is thus in apparent conflict with the constant stress drop hypothesis, a point first recognized by [*Scholz*, 1982a]. A number of observations and hypotheses have been brought forth to reconcile the issue.

Models of earthquake rupture conventionally impose the boundary condition that coseismic slip be mechanically limited to zero at the base of the seismogenic layer. The observed increase in slip with length may be explained by modifying the boundary condition such that coseismic slip is a rapid upward extension of displacement that has accumulated below the seismogenic layer prior to the earthquake [*Scholz*, 1982a]. Physical fault models arising from such an explanation predict that the time for displacement to occur at any point on a fault should be on the same order as the total duration of faulting [*Scholz*, 1982b]. The idea is not supported by dislocation time histories of fault ruptures which are short compared to the overall duration of an

earthquake [*Heaton*, 1990]. Today it appears to remain generally accepted that large earthquake ruptures are the result of simple elastic failure whereby displacements are limited to zero at the base of the seismogenic layer. Efforts to explain the enigmatic increase of S with L generally invoke the idea that large earthquakes commence with systematically larger stress drops or unusually large slip pulses relative to earthquakes of lesser size [*Bodin and Brune*, 1996; *Heaton*, 1990], and thus have a tendency to propagate over greater distances. Independent observations of the interaction of earthquake ruptures and the geometry of faults presented here and in *Wesnousky* [2006] are at odds with this latter idea. An alternate explanation is that the base of the seismogenic zone does not result from the onset of viscous relaxation but rather a transition to stable sliding in a medium that remains stressed at or close to failure and that coseismic slip during large earthquakes may extend below the seismogenic layer. The latter explanation is explored in more detail by *King and Wesnousky* [2006], satisfies standard elastic models, and preserves both the idea of constant stress drop in light of the observed increase of S with L.

The Growth of Earthquake Ruptures

The majority of coseismic slip during continental earthquakes is generally concentrated in the upper 15 km of the earth's crust. The length of strike-slip ruptures considered here ranges from about 15 km to >400 km. The direction of rupture propagation may be viewed as primarily horizontal for each event. Theoretical and numerical models and observation support the idea of a causal association between fault steps and the endpoints of earthquake ruptures [e.g., *Harris and Day*, 1993; 1999; *Oglesby*, 2005; *Segall and Pollard*, 1980; *Sibson*, 1985; *Wesnousky*, 1988]. The synopsis of observations in **Figure 14** shows that there is a transition in step-dimension at 3-4 km above which strike-slip faults appear not to propagate and that the transition is largely independent of rupture length. The observation leads me to think that the magnitude of stress changes and the volume effected by those stress changes at the leading edge of propagating earthquake ruptures are similar at the initial stages of rupture propagation and largely invariable during the rupture process (**Figure 19**). The transition of 3-4 km in step width above which ruptures have not propagated by analogy places a limit on the dimension of process zone or volume significantly affected by stress changes at the

rupture front. In this context, it appears that variations in earthquake rupture lengths are not necessarily controlled by the relative size of initial slip pulses or stress drops [e.g., *Brune*, 1968; *Heaton*, 1990] but rather by the geometrical complexity of fault traces [e.g., *Wesnousky*, 1988] and variations in accumulated stress levels along faults that arise due to the location of past earthquakes [e.g., *McCann et al*., 1979].

The observations of (**Figure 12**) which summarize the relationship between the location of earthquake epicenters and the asymmetry of slip distributions also have bearing on the topic of fault propagation. The observations show no systematic correlation between the initiation point of an earthquake and the location of maximum slip along fault trace. The result is independent of which asymmetric curve fit is used to approximate the shape of the slip distributions. Indeed, while one may examine the figure and point to a number of earthquakes where the epicenter is spatially correlated to the peak of the slip distribution, there are numerous events where the epicenter is spatially separated from the peak. The latter observation is most evident for those events of unilateral rupture where the ratio E/L is close to 0 or 1. I view the observation to indicate that patterns of slip are also not controlled by the relative size of initial slip pulses but likely instead by variations in accumulated stress reflecting variations in fault strength and accumulated stress along strike.

The Shape of Slip Distributions and Self-Similarity

The exercise of fitting curves to the slip distributions (**Figure 9)** shows the unsurprising result that better fits to the observations are obtained with the increase in freely adjustable variables used in the regressions. The average (i.e. *flat-line*), symmetric (i.e. *sine* and *ellipse*), and asymmetric (i.e. *asymmetric sine*, *asymmetric ellipse* and *triangle*) functions yield increasingly better fits to the observed slip distributions (**Figure 10**). Similarly, the asymmetric forms may be viewed as a better approximation to the general shape of surface slip distributions. The degree of asymmetry that one observes in fitting asymmetric functions to the slip distributions is dependent on the particular form of the function (**Figure 11**). The assumption of a *triangle* function tends to exaggerate the asymmetry as compared to the *asymmetric sine* or *ellipse*. The exaggeration results because of the control of the assumed functions on the slope of the curve-fit near the rupture endpoints. The scatter in values of asymmetry for the triangular and asymmetric

ellipse curves would argue against the suggestion that the slip curves are self-similar in nature whereas the lessening of scatter in the value for the asymmetric sine fits might allow it (**Figure 11**). The statistical differences in the triangle and asymmetric curve-fits to the observations are insufficient to allow a resolution of the matter.

The systematic changes in slope attendant to the plots of the peak amplitudes of the curves fit to the surface slip distributions versus rupture length shown in **Figure 13** provide another manner to characterize the shapes of the surface slip distributions. The plots show the same characteristics as observed in the earlier plots of average surface slip versus rupture length (**Figure 7**). Specifically, the fewer normal and reverse earthquake data may be fit by a straight line but the strike-slip earthquakes which cover a wider range of rupture lengths cannot. The observations for the strike-slip earthquakes and the entire data set overall are better fit by a curve that decreases with slope as a function of increasing rupture length. The slope reflects the ratio of amplitude to length of the assumed slip functions. In this regard, the average shapes of the prescribed surface slip distribution vary across the magnitude spectrum of the observed earthquakes and may not be viewed as self similar.

Conclusions

I have put forth a compilation of about 3 dozen historical earthquakes for which there exist both maps of earthquake rupture traces and data describing the coseismic surface slip observed along fault strike. The analysis of that data presented here may be of use in developing seismic hazard methodologies and placing bounds on physical fault models meant to describe the earthquake source. In these regards, observations provide statistical approach to predicting the endpoints and surface slip distribution of earthquakes on mapped faults. They also lend support to the ideas that there exists a process zone at the edges of laterally propagating earthquake ruptures of no more than about 3-5 km dimension within which stress changes may be sufficient to trigger slip on adjacent faults, and that the ultimate length of earthquake ruptures is controlled primarily by the geometrical complexity of fault traces and variations in accumulated stress levels along faults that arise due to the location of past earthquakes.

Acknowledgements

Support for some of the research was provided by USGS NHERP contract 04HQPA00 and NSF/SCEC Award 077946/EAR-0106924. Center for Neotectonics Contribution Number XX.

Table 1: Geological Observations

#	Date Location	*Type	Length(km)	Average Slip (m)	Max Slip (m)	Depth (km)	Rigidity 10^{11}dyn/cm^2	Geo- Mo^g 10^{26}dyn-cm	Geo-Po 10^{15} cm^3	M_W^g	Reference&	Notes+
1	1857-1-9 San Andreas, CA	ssr	360	4.7	9.1 (12)	15	3	76	25.4	7.9	1	a
2	1887-5-3 Sonora, MX	n/60	70	2.2	4.1	15	3	8.0	2.7	7.2	2,3,48	b
3	1891-10-28 Neo-Dani, JPN	ssl	80	3.1	7.9	15	3	11.3	3.8	7.3	4	c
4	1896-8-31 Rikuu, JPN	r/45	37	2.5 [3.5]	6.2 [8.8]	15	3.0	8.2	2.7	7.2	5	d
5	1915-10-2 Pleasant Val, NV	n/45	61	1.8[2.6]	5.8[8.2]	15	3.1	10.3	3.4	7.3	6	e
6	1930-11-2 Kita-Izu, JPN	ssl	35	1.1	3.5	12	3.3	1.6	0.48	6.7	7	f
7	1939-12-25 Erzincan, TUR	ssr	300	4.2	7.4	13	3.2	52.5	16.4	7.7	8	g
8	1940-5-19 Imperial, CA	ssr	60	1.6	3.3	13	2.5	3.0	1.2	6.9	9	h
9	1942-12-20 Erbaa-Niksar, TUR	ssr	28	1.66	1.9	13	3.2	1.8	0.6	6.8	8	i
10	1943-11-26 Tosya, TUR	ssr	275	2.5	4.4	13	3.2	28.7	9.0	7.6	8	j
11	1943-9-10 Tottori, JPN	ssl	10.5	0.6	1.5	15	3.3	0.3	.09	6.3	10	k
12	1944-2-01 Gerede-Bolu, TUR	ssr	155	2.1	3.5	13	3.2	13.3	4.2	7.35	8	l
13	1945-1-31 Mikawa, JPN	r/30	4.0	1.3	2.1	8	3.0	0.24	.08	6.2	11	m
14	1959-8-17 Hebgen Lake, MT	n/50	25	2.5	5.4	15	3.0	3.7	1.25	7.0	12	s
15	1954-12-16 Fairview Peak, NV	nssr/60	62	1.1	5.2	15	3.0	3.5	1.2	7.0	13	n
16	1954-12-16 Dixie Valley, NV	n/60	47	0.8[0.9]	3.1[3.5]	12	3.0	1.76	0.6	6.8	13	t
17	1967-7-22 Mudurnu, TUR	ssr	60	0.9	2.0	12	2.4	1.6	0.65	6.7	8	u
18	1968-4-8 Borrego Mtn, CA	ssr	31	.13	0.4	12	3.3	.16	0.05	6.1	14	v
19	1971-02-09 San Fernando, CA	r/45	15	0.95	2.5	15	3.4	1.0	0.30	6.7	59	ap
20	1979-6-02 Cadoux, AUS	r/35	10	0.6	1.2	6	3.2	0.20	.06	6.1	49	x
21	1979-10-15 Imperial, CA	ssr	36	0.28-.41	0.6-.78	13	2.5	.33-.48	0.13-0.19	6.3-6.4	15,16	w
22	1980-10-10 El Asnam, Algeria	r/50	27.3	1.2	6.5	12	3.0	1.55	0.5	6.7	60	aq
23	1981-7-29 Sirch Iran	ss/69	64	.13	.50	15	3.3	0..43	.13	6.4	50	aj

24	1983-10-28 Borah Peak, ID	n/45	34	.94[1.3]	2.8[4.0]	14	3.2	2.9	0.89	6.9	17	y
25	1986-3-3 Marryat, AUS	r/35	13	.24(s)[.42] 0.26u[0.46]	0.70(s) [1.2] 0.8u[1.4]	3	3.2	.09(s) .10(u)	.03(s) 03(u)	5.9(s) 5.9(u)	46	z
26	1987-11-23 Super. Hills, CA.	ssr	25	0.3 - 0.6	.5 - 1.1	12	2.5	.22 - .47	.09-.19	6.2-6.4	18	aa
27	1987-03-2 Edgecumbe, NZ	n/60	15.5	.0.6[0.7]	2.6[3.0]	10	2.6	0.33	.13	6.3	19	ao
28	1988-01-22 Tennant Crk, AUS	r/45	30	0.7 [1.0]	1.8[2.5]	8	3.3	1.1	.34	6.6	43	ab
29	1990-07-16 Luzon, PHL	ssl	112	3.5	6.2	20	3.5	27.4	7.84	7.6	20,21	am
30	1992-06-28 Landers, CA	ssr	77	2.3	6.7	15	3.0	8.1	2.7	7.2	22	ac
31	1998-03-14 Fandoqa, IRN	ssn/54	25	1.1	3.1	10	3.3	1.2	.36	6.6	50	ag
32	1999-09-21 Chi-Chi, Taiwan	r/70	72	3.5 [4.0]	12.7 [16.4]	20	3.0	18.4	6.1	7.4	23	ad
33	1999-10-16 Hector Mine, CA.	ssr	44	1.56	5.2	12	3.0	2.5	0.82	6.9	57	an
34	1999-08-17 Izmit, TUR	ssr	107 (145)	1.1	5.1	13	3.2	4.9	1.5	7.1	47	ae
35	1999-11-12 Duzce, TUR	ssr	40	2.1	5.0	13	3.2	3.5	1.1	7.0	24	af
36	2001-11-14 Kunlun, China	ssl	421	3.3	8.7	15	3.0	62.5	20.8	7.8	53	am
36a	2001-11-14 (spot) Kunlun, China	ssl	428	2.4	8.3	15	3.0	46.8	15.6.	7.8	61	al
37	2002-11-03 Denali, AK (Haessler)	ssr	302	3.6	8.9	15	3.2	51.6	16.1	7.7	52	ak

* Type of earthquake mechanism and dip. Right and left-lateral strike slip are ssr and ssl, respectively. Reverse and normal are r and n, respectively. Right-lateral normal oblique motion is nssr.

& See Table 3 for key to references.

\+ See Table 1a for notes bearing on basis for assigning column values and location of epicenter when plotted.

Table 1a: Notes for Table 1

a. Value in parenthesis is that reported in text of original reference. Other is maximum of digitized slip curve as provided in original reference. Value of width taken from average depth of microseismicity along fault observed in *Hill et al*. [1990]. Rigidity of $3x10^{11}$ dyn/cm^2 assumed. Digitized slip curve value used in plots and regressions. Epicenter assumed to be at northern end of trace based on *Sieh* [1978a].

b. Digitized slip curve taken from (3) and is scarp height and for this reason may overestimate actual displacement. Max Suter (pers. comm.) suggests the rupture is significantly longer but chose not to share his observations at this time. Moment calculated assuming 60° dip. Rigidity and fault depth assumed same as used for 1954 Fairview Peak earthquake.

c. Moment calculated from vector sum of left-lateral and vertical slip measurements. Fault depth assumed same as average base (15Km) of seismogenic layer [e.g. *Wesnousky et al*., 1982]. Rigidity assumed same as used for 1943 Tottori earthquake. Epicenter taken from *Research Group for Active Faults* [1991].

d. Total length measured along average strike from ends of Obanai and Senya fault segments. Vertical component of slip provided in original surface slip distribution. Values in brackets are corrected for dip and used when calculating moment and making plots and regressions. Individual segment values are original values from slip distribution and not corrected for dip. Values of maximum and average slip for entire trace are obtained after summing slip of main and conjugate traces. Dip of Senya fault is 45-70° from field observation [*Matsuda et al*., 1980]. *Thatcher et al*. [1980] use rigidity of $3x10^{11}$ dyn/cm^2 in geodetic analysis of event. Fault depth assumed same as average base (15Km) of seismogenic layer [e.g. *Takagi et al*., 1977; *Wesnousky et al*., 1982]. Epicenter taken from *Research Group for Active Faults* [1991].

e. Fault dip 'well-defined' at 44°±8° [*Doser*, 1988]. Vertical component of slip provided in original surface slip distribution. Values in brackets are corrected for dip and used when calculating moment. Individual segment values are original values from slip distribution and not corrected for dip. Values of fault width assumed same as used for 1954 Fairview Peak earthquake. Value of rigidity is back calculated from parameters of moment, fault width, and displacement given to the event by [*Doser*, 1988].

f. Slip Distribution curve is modified by author to more closely approximate distribution of measurements. Original curve of *Matsuda* [1972] appears to consistently be greater than maximum values of measurement. Only horizontal values of slip used here because they are dominant and vertical components alternate along fault strike and likely reflect in large part the horizontal displacement. Epicenter for event is that reported by *Nakata et al*. [1998]. Fault depth (12 km) is depth of aftershock distribution for nearby 1974 Izu-Oki earthquake and also same as elastic model that gives best fit to displacements measured with triangulation data in 1930 [*Abe*, 1978]. Rigidity value assumed similar to that used in geodetic moment determination of *Abe* [1978]. Epicenter taken from *Research Group for Active Faults* [1991].

g. Fault depth 12.5 and shear modulus (3.2) are those used by *Stein et al*. [1997] in modeling of stress transfer along Anatolian fault. Source cites *McKenzie* [1972] for focal mechanism and presumably epicenter, and incorporates measurements of *Pamir and Ketin* [1941] and *Kocyigit* [1989; 1990] into his slip distribution curve. Epicenter taken from *Barka* [1996] whom cites *Dewey* [1976].

h. Rigidity and fault depth values are assumed same as used for 1979 Imperial Valley earthquake. Best-fitting geodetic analysis places confines slip to upper 13 km of crust [*Doser and Kanamori*, 1987; *Reilinger*, 1984]. Subdivision of segments 'north' and 'south' reflects measures to north and south of All American Canal, respectively, where there is abrupt change in displacement values in apparent absence of any structural discontinuity along fault trace. Epicenter taken from maps of *Trifunac* [1972] and also *Anderson and Bodin* [1987].

i. Fault depth 12.5 and shear modulus (3.2) are those used by *Stein et al*. [1997] in modeling of stress transfer along Anatolian fault. Slip distribution also incorporates measurements of [*Pamir and Aykol*, 1943]. Epicenter is taken from [*Stein et al*. [1997]. Uncertainty in epicenter location is comparable to rupture length [*Dewey*, 1976].

j. Fault depth 12.5 and shear modulus (3.2) are those used by *Stein et al*. [1997] in modeling of stress transfer along Anatolian fault. Slip distribution also incorporates measurements of [*Ando*, 1974b;

Blumenthal, 1945a; 1945b; *Ketin*, 1969; *Ozturk*, 1980]. Epicenter is taken from [*Stein et al*. [1997] and he cites relocated ISC earthquakes by *Engdahl et al* [1998].

k. Mean and max slip values are taken from vector sum of displacement components along trace. Slip distribution plot shows interpolated values used by author (thick dashed lines) and those originally interpreted (thin dashed lines) by source. Rigidity assumed on basis of from *Kanamori*'s [1973] seismological analysis (see Table 2). Fault depth assumed same as average base (15Km) of seismogenic layer [e.g., *Wesnousky et al*., 1982].

l. Fault depth 12.5 and shear modulus (3.2) are those used by *Stein et al*. [1997] in modeling of stress transfer along Anatolian fault. Slip distribution includes new measures of slip and compilations of older observations [*Allen*, 1969; *Ambraseys*, 1970; *Ketin*, 1948; 1969; *Tasman*, 1944]. Epicenter is taken from [*Stein et al*. [1997] and he cites relocated ISC earthquakes by *Engdahl et al*. [1998].

m. Fault dip (30°) and depth (8km) are from seismological analysis of *Kikuchi et al*. [2003]. Value of rigidity assumed to same as used in that same analysis (see Table 2). Assumption is made that lateral values of slip are apparent. Calculations include only measures of vertical slip.

n. Moment value is sum of all segments (ΣMo). Average displacement calculated as $\Sigma Mo/(3x10^{11}dyne/cm^2)(15km/sin(60))(62km)$. Fault depth (15km) and dip (60°) based on long-period body-wave analysis of *Doser* [1986]. Geodetic fault models of *Hodgkinson et al*. [1996] suggest most slip occurred at depths shallower than 8 km. Value of rigidity taken to be same as used by *Hodgkinson et al*. [1996]. Epicenter taken from *Doser* [1986]

s. Slip distribution constructed by author from original measurements of displacement on Plate 2 of *Witkind* [1964]. Range of epicenter estimates shown by oval in slip distribution plot encompasses estimates of *Doser* [1985] and *Ryall* [1962]. Average value of rigidity is that used by *Barrientos et al*. [1987] in their geodetic analysis of event. Depth extent of faulting (15 km) in concert with focal depth determination and geodetic modeling of source [*Barrientos et al*., 1987; *Doser*, 1985]. Average dip (50°) assumed based on long-period body wave analysis of *Doser* [1985]. Epicenter reflects range of values from *Doser and Smith* [1985] and *Ryall [1962]*.

t. Original slip distribution gives measures of vertical separation. Values in square brackets are corrected for fault dip (sum of vertical separations / sin(60°). Geologic Moment calculated assuming 60° dipping fault and reflect vector sum of displacements on all traces. Fault depth assumed to be 12 km based on hypocentral depth calculation of *Doser* [1986]. The lesser value as compared to the Fairview Peak earthquake is consistent with geodetic modeling of *Hodgkinson et al*. [1996] that suggests slip was confined to shallower depths than Fairview Peak. Value of rigidity taken to be same as used by *Hodgkinson et al*. [1996]. Epicenter assumed to be at south end of rupture and triggered by 1954 Fairview Peak but in reality simply assumede.

u. Length and moment calculation for main fault trace between about Kanlicay and Guney. The single reported measure near Sapanca is not included. Epicenter adapted from [*Stein et al*., 1997]. Value of rigidity is derived from average velocity-density crustal model used by *Pinar et al* [1996] to compute Green's functions. Analysis of teleseismic body waves place most moment release at 10 km. Depth extend assumed 12 km on that basis. Epicenter is taken from [*Stein et al*. [1997] and he cites relocated ISC earthquakes by *Engdahl et al*. [1998].

v. Central and south strands recorded afterslip. Values in this table also reflect measurements in April and June after earthquake. Depth extent of aftershocks limited to 12 km [*Hamilton*, 1972]. Value of rigidity assumed similar to that used at source depth in analyses determining seismic moment (see Table 2). Epicenter taken from *Allen and Nordquist* [1972].

w. Aftershocks and geodetic models indicate slip limited to upper 13 km of crust [*Doser and Kanamori*, 1986; *Reilinger*, 1984]. Rigidity of $2.53x10^{11}dyne/cm^2$ based on velocity density model of *Hartzell and Heaton* [1983]. See notes for Table 2. Range of surface displacement values is for measurements taken 4 days and 160 days after event. Values for 160 days used in plots.

x. Net surface displacements taken from Table 3 of source. Dip and depth taken from teleseismic body-wave inversion of *Fredrich et al*. [1988]. Depth is twice centroid depth. Rigidity is derived from velocity-density structure at source used by *Fredrich et al*. [1988].

y. Original slip distribution gives measures of throw (vertical). Values given reflect vertical throw, except for those in square brackets which are corrected for dip. Fault dip and depth are from [*Doser and Smith*, 1985] and [*Richins et al*., 1987]. Value of rigidity is average of values that have been used in calculating seismic moment from waveforms (see Table 2). Note segments in digitized slip curve are separated by decay in displacement to 0 and discontinuities and bends in fault strike.

Segments 1 and 2 show distinct patches of relatively increased slip with long 'tails' of lesser slip. Values in parenthesis are those for the 'slip patch' and 'tails'. 1983 Borah Peak epicenter from [*Richins et al*., 1987].

z. Original slip distribution gives measures of throw (vertical). Values in square brackets are corrected for fault dip. Dip and depth of fault plane taken to equal 35° and 3 km, respectively, based on centroid moment determination of *Fredrich et al*. [1988]. Rigidity assumed on basis of velocity-density structure at source given by *Fredrich et al.* [1988]. Length of slip distribution curve measured along curved trace. Separate values are for smoothed (s) and unsmoothed slip distribution curves. Unsmoothed is used in plots. Epicenter from *Fredrich et al*. [1988] and/or *Machette et al. [1993].*

aa. Results provided for slip after 1 day and final displacement predicted to power-law fit to observed decay of after-slip with time. Aftershocks limited to upper 12 km of crust [*Magistrale et al*., 1989]. Rigidity computed from velocity-density structure used by *Frankel and Wennerberg* [1989]. Plots use final displacement value. Epicenter taken from *Sharp et al*. [1989].

ab. Dip and depth of faulting from aftershock and waveform analysis of *Choy and Bowman* [1990]. Rigidity (3.3) is value used in that same analysis (George Choy, United States Geological Survey, pers. comm.)Vertical component of slip provided in original surface slip distribution. Values in brackets are corrected for dip and used when calculating moment. Individual segment values are original values from slip distribution and not corrected for dip. Epicenter taken from *Choy and Bowman* [1990].

ac. Source provides a cumulative slip distribution which is sum of contributions of individual strands composing rupture. Assessment of characteristics of individual traces required differencing the contributions of individual traces. Aftershock distribution extends to 15km depth [*Sieh et al*., 1993]. Rigidity assumed same as generally used in seismological analyses of event. Epicenter taken from *Sieh et al.* [1993].

ad. Displacement values are the vector sum of the original slip distributions which provide vertical and lateral components of slip separately. Values in brackets take into account fault dip. Geologic moment calculated assuming fault dips at 70°. Aftershocks mostly confined to upper 20 km of crust [*Lin*, 2001]. Rigidity reflects average of velocity-density structures used in seismological analyses of event (see Table 2). Epicenter taken from *Lin et al*. [2002].

ae. Fault depth 12.5 and shear modulus (3.2) are those used by *Stein et al*. [1997] in modeling of stress transfer along Anatolian fault. Length of slip and, hence, geologic estimate of Mo is minimum because trace is submerged beneath Marmara sea at west end. Total length is probably about 145 km. Similarly, characteristics of Golcuk and Herzek sections of the fault are incomplete and not considered separately. Depth of aftershocks generally limited to upper 15 km of crust [*Ergin et al*., 1999]. Epicenter taken from *Akyuz et al*. [2002] but note fault extends offshore which is not reflected in surface distribution plot.

af. Displacement values are vector sum of vertical and horizontal slip. Values of rigidity and fault depth kept same as used for events on eastern Anatolian fault. Thus, fault depth 12.5 and rigidity (3.2) are those used by *Stein et al*. [1997] in modeling of stress transfer along Anatolian fault, although aftershocks of the earthquake were generally limited to above 17 km [*Milkereit et al*., 1999; *Umutlu et al*., 2004]. Epicenter taken from *Akyuz et al.* [2002].

ag. Fault dip from teleseismic analysis [*Berberian et al*., 2001] and fault depth is twice the centroid moment depth and equal to depth of found with INSAR modeling of source by same authors. Original slip distribution gives values of vertical and lateral components of slip separately. Value of slip is for total fault slip including effect of dip (sqrt((vertical/sin(54))^2+(strike slip)^2).

ah. Fault width of 10 km assumed based on range of aftershock depths reported by [*Eberhart-Phillips et al*., 2003]. Rigidity (3.2) assumed between that used by *Ozacar and Beck* [2004] and *Frankel* [2004](see Table 2)

ai. Original slip distribution provides measures of vertical separation and horizontal slip separately. Slip values are vector sums of two components and that in brackets is corrected for fault dip (e.g. slip/sin(dip)). Values of dip (69) on basis of teleseismic analysis by *Berberian et al*. [2001]. Fault depth of 15 km assumed. Centroid moment solution depths reported by *Berberian et al*. [2001] are 15 to 18 km but he notes 'depths are not well resolved'. Same authors note surface slip appears small for length of fault and suggest most slip concentrated at depth.

aj. Mechanism and slip calculated same as for 1998 Fandoqa earthquake. Each occurred on same fault. Exception to this is that dip and fault depth assumed to be 15km based on body-wave analysis of *Berberian* [2001](see Table 2).

ak. Values reflect vector sum of vertical and horizontal slip. Fault width of 10 km assumed based on range of aftershock depths reported by [*Eberhart-Phillips et al.*, 2003]. al. *Ozacar and Beck* [2004] note regional seismicity limited to about 15 km depth. Rigidity (3.2) assumed between that used by *Ozacar and Beck* [2004] and *Frankel* [2004](see Table 2). Epicenter taken from *Haeussler et al* [2005].

al. Digitized slip distribution is that of *Xu et al*. [2002] modified in central portion where reexamined by *Klinger et al*. [2005]. Fault trace is taken from *Klinger et al.* [2005]. Depth of rupture assumed to be same as depth of background seismicity (15) as stated by *Ozacar and Beck* [2004]. Rigidity (3) is that used by *Ozacar and Beck* [2004] (Arda Ozacar, Dept. of Geological Sciences, University of Arizona, pers. comm.). Epicenter taken from *Klinger et al*. [2006].

am. Width based on depth extent of aftershocks [*Shibutani*, 1991; *Yoshida and Abe*, 1992] and value of rigidity of 3.5 follows assumption of [*Velasco et al.*, 1996]. Epicenter taken from map of *Nakata* [1990]. Epicenter taken from *Klinger et al.* [2006].

an. Depth of aftershocks extends to and is limited to above 15 km [*Hauksson et al*., 2002]. Rigidity value is approximate average value from zero to 15 km [*Jones and Helmberger*, 1998; see figure 10 in *Simons et al*., 2002]. Two values of average and max offset are given. First includes only offsets on main trace. Second also includes contribution from secondary traces. Differences do not change estimates of geologic moment or potency at level of significance listed in table. Epicenter as reported in *Treiman et al*. [2002]

ao. Slip distribution describes vertical component of displacement. Range of dip values reported for fault range from 55°-71°. Values of offset in brackets are corrected for dip (offset/sin(60°)). Moment is calculated with corrected values of slip. Depth of aftershocks is limited to upper 10 km [*Robinson*, 1989] Rigidity of 2.6×10^{11}dyne/cm^2 is computed from average velocity-density structure [*Ozacar and Beck*, 2004]in upper 15 km of crust [see Table 1 of *Anderson and Webb*, 1989]

ap. Slip distribution is for total slip. Dip of 45° assumed on basis of waveform and focal mechanism analysis Rigidity of 3.4×10^{11}dyne/cm^2 is average of values explicitly stated in Table 2. Depth extent of faulting assumed from depth of aftershocks and bodywave form analyses cited.

aq. Slip profile is for vertical component. Aftershock analyses indicate depth of seismicity reaches 12 km. Focal mechanism and waveform modeling indicate average dip of 50°, leading to ~15 km fault plane width. Only displacement from fault offset at surface considered, not folding component. Epicenter taken from *Yielding et al* [1981].

ar. Slip profile from computer analysis of SPOT imagery [*Klinger et al.*, 2006]. Fault trace is taken from *Klinger et al*. [2005]. Depth of rupture assumed to be same as depth of background seismicity (15) as stated by *Ozacar and Beck* [2004]. Rigidity (3) is that used by *Ozacar and Beck*, 2004][2004] (Arda Ozacar, Dept. of Geological Sciences, University of Arizona, pers. comm.)

Table 2: Seismological Observations

#	Date Location	Type	Mo^{BODY} 10^{26} dyn-cm	$Mo^{LONG-PEROD}$ 10^{26} dyn-cm	$Mo^{GEODETIC}$ 10^{26} dyn-cm	Range 10^{26} dyn-cm	Po^{BODY} 10^{15} cm^3	$Po^{LONG-PEROD}$ 10^{15} cm^3	$Po^{GEODETIC}$ 10^{15} cm^3	Range 10^{15} cm^3	References	Notes
5	1915-Oct-2 Pleasant Val, NV	n/60	2.7±0.6 (3.3)			2.7±0.6	.82			.82	27	be
6	1930-Nov-2 Kita-Izu, JPN	ssl			2.7(3.3)	-			.82	.82	56	bak
8	1940-May-19 Imperial, CA	ssr	2.3 (3.3) 3.0 (3*) 4.4 (3.3)	4.8 (3.3)	8.4 (3.3*)	5.3 ±3.1	.696 1.0 1.3	1.45	2.5 5	1.62 ±.92	42	bh
11	1943-Sep-10 Tottori, JPN	ssl	3.6 (3.35)			3.6	1.08			1.08	40	bk
13	1945-Jan-31 Mikawa, JPN	r	1(3) 1(2.5)		0.87(3)	0.94 ±.065	.33 .40		.29	.35±.05	41	bm
14	1959-Aug-17 Hebgen Lake, MT	n/500	10(3.3)	15(3)	13(3.23)	12.5±2.5	3.0	5.0	4.0	4.0 ±1.0	31	bs
15	1954-Dec-16 Fairview Peak, NV	nssr/60	5.5(3)		4.6(3.0)	5.05 ±0.45	1.83		1.53	1.68 ±.15	35	br
16	1954-Dec-16 Dixie Valley, NV	n/60	1.0(3.3)		2.2(3.0)	1.6±0.6	0.30		0.73	0.52 ±0.22	36	bt
17	1967-Jul-22 Mudurnu, TUR	ssr	8.8(3.3) 11 (2.4) 15(3*)	7.5(3*)		11.25 ±3.75	2.67 4.58 5.0	2.5		3.75 ±1.25	39	bu
18	1968-Apr-8 Borrego Mtn, CA	ssr	.9(3) 1.1(3.4) 0.7(3.3) 1.2(3.8)	1.1(3*)		0.95 ±0.25	.3 .32 .21 .315	.37		.29 ±.08	28	bv
19	1971-2-09 San Fernando, CA	r/45	1.3(3*) 0.9(3.5) 1.7(3.3)	1.9(3*)		1.4 ±0.5	0.43 0.23 0.52	0.63		0.38± 0.15	59	bam
20	1979-Jun-02 Cadoux, AUS	r/35	.15(3.2)	0.175(4.4)		.163 ±.013,	.046	.040		.043 ±.0035	45	bx
21	1979-Oct-15 Imperial, CA	ssr	0.5(2.5) 0.5(2.5)	0.7(3*) .72(2.7)		0.61 ±0.11	.20, .20	.233 .267		.233 ±.033	30	bw
22	1980-10-10 El Asnam	r/50	2.5(3)			2.5				0.83	60	ban
23	1981-Jul-29 Sirch, IRAN	ss/54	3.7(3.3*)	9.0(4.4)		6.35 ±2.65	1.12	2.05		1.58 ±.046	50	bah

24	1983-Oct-28 Borah Peak, ID	n/60	2.1(3.3) 2.3(2.5)	3.5(3*), 3.1(2.7)	2.6(3.2) 2.9(3.2)	2.8 ±0.7	.64 .92	1.2 1.1	.81 .91	.90 ±.27	29	by
25	1986-Mar-3 Marryat, AUS	r/35	.06(3.2)			.06	.019			.019	45	bz
26	1987-Nov-23 Superstition Hills, CA.	ssr	0.5(3.3) 0.8(1.8) 0.2(2.3)	1.0(3*) 0.7(4.4)	0.9(2.8)	0.6±..4	.15 .44 .09	.33 .16	.32	.266 ±.18	33	baa
27	1987-Mar-2 Edgecumbe, NZ	n/60	0.4(3.5) 0.7(3.6)	0.9(3.6) 0.6(4.4)		0.65 ±0.25	.11 .19	.25 .14		.182 ±.067	34	bai
28	1988-Jan-22 Tennant Creek, AUS	r/45	1.6(3.3)	1.5(4.4)		1.55 ±.05	.48	.35		.41 ±.07	44	bab
29	1990-Jul-16 Luzon, PHL	ssl	36(4.0)	39(7.3) 41(4.4)		38.5 ±2.5	9.0, 5.3	9.3		7.3± 2.0	32	baj
30	1992-Jun-28 Landers, CA	ssr	7(3*) 7.5(3)	8(3*) 10.6(4.4)	9(3.0) 10(3*)	8.8 ±1.8	2.3 2.5	2.7 2.4	3.0 3.3	2.8± 0.5	25	bac
31	1998-Mar-14 Fandoqa, IRN	ssn	0.9 (3.3)	0.95 (4.4)	1.2(3.4)	1.05 ±0.15	.28	.22	.35	.284 ±.07	50	bag
32	1999-Sep-20 Chi-Chi, Taiwan	r/70	29(2.1) 41(3.0)	34(4.4)	27(3)	34±7	13.8 13.7	7.7	9.0	10.8± 3.0	26	bad
33	1999-Oct-16 Hector Mine,CA	ssr	6.2(3*)	6.0(4.4)	6.8(3*) 5.9(3*) 7.0(3.)	6.45±0 .55	2.1	1.4	2.3 2.0 2.3	1.8± 0.45	58	bal
34	1999-Aug-17 Izmet, TUR	ssr	22(3.3 15(3.5)	28.8(4.4)	24(3.3) 18(3.3) 26(3.4)	21.9 ±6.9	6.7 4.3	6.6	7.3 5.4 7.7	5.97 ±1.7	38	bae
35	1999-Nov-12 Duzce, TUR	ssr	5.0(3*)	6.7H(4.4)	5.4(3.0)	5.4 ±1.3	1.67	1.52	1.8 0	1.66 ±.14	37	baf
36	2002-Nov-14 Kunlun, China	ssl	46(3) 50(3.0)	59(4.4)	71(3 *)	58.5 ±12.5	15.3, 16.7	13.4	23. 6	18.5 ±5.1	55	bai
37	2002-Nov-03 Denali, AK	ssr	68(3.3) 38(3*) 49(3*) 56(3)	75(2.6)		56.5 ±18.5	20.1 12.7 16.3 18.7	28.8		20.7 ±8.1	54	baj

Notes: See Table 2a
References: See Table 3.

Table 2a: Notes for Table 2

be. Rigidity not cited in original text of source. Value used was $3.3x10^{11}$ dyn/cm^2 (Diane Doser, University of Texas, El Paso, pers. comm).

bh. Rigidity for moment estimates (2.3 and 4.8) not cited in original texts of sources [*Doser*, 1990; *Doser and Kanamori*, 1987]. Value used was $3.3x10^{11}$ dyn/cm^2 (Diane Doser, University of Texas, El Paso, pers. comm.]. The value of rigidity used in *Thatcher and Hanks*' [1973] estimate of body-wave moment (3.0) is incorporated into expression for shear displacement spectra but not explicitly stated in text. Value of 3.0 for rigidity is assumed. *Trifunac and Brune*,'s [1970] do not state the value of rigidity used in estimate of body-wave moment (4.4). They used value of rigidity = $3.3x10^{11}$ dyn/cm^2 when using geologic data to compute moment. Assumed here that same value was used in their estimate of seismic moment. The geodetic moment (8.4) arises from *Doser and Kanamori*'s [1987] interpretation of *Reilinger's* [1984] geodetic model. The interpretation does not state value of rigidity used. Value of 3.3 is assumed here.

bk. Value of rigidity used in estimate of body-wave moment (3.6) not explicitly stated. Value of rigidity $3.35x10^{11}$ dyn/cm^2 is back calculated from *Kanamori*'s [1973] statement of source dimensions and moment estimate (μ=Mo/LWD).

bm. Value of rigidity not explicitly stated in text of *Kikuchi et al*. [2003]. It is inferred to equal $3.0x10^{11}$ dyn//cm^2 from their statement of source dimensions (20km x 15km), average coseismic slip (1.1m), and moment (1.0). *Ando* [1974a] uses rigidity $3.0x10^{11}$ dyn/cm^2 to calculate seismic moment (0.87) from geodetic model. *Kakehi and Iwata* [1992] report seismic moment (1.0), source dimensions (12km x 11km), and average slip (3m) from which it is calculated here that they used average rigidity of 2.5×10^{11} dyn/cm^2.

br. Rigidity for moment estimate (5.5) not cited in original text of source [*Doser*, 1985]. Value used was $3.3x10^{11}$ dyn/cm^2 (Diane Doser, University of Texas, El Paso, pers. comm.]. *Hodgkinson et al.* [1996] use a value of rigidity $3.0x10^{11}$ dyn/cm^2 too calculate geodetic moment from model fault parameters.

bs. Rigidity for moment estimates (10 and 13) not cited in original texts of sources [*Doser*, 1985; *Doser and Kanamori*, 1987]. Values used were $3.3x10^{11}$ dyn/cm^2 (Diane Doser, University of Texas, El Paso, pers. comm.]. *Barrientos et al*. [1987] explicitly state rigidity of $3.0x10^{11}$ dyn/cm^2 used in calculation of geodetic moment.

bt. Value of rigidity used in calculation of body wave moment (1.0) by *Doser* [1986] not provided. Assumed here to be $3.0x10^{11}$ dyn/cm^2. *Hodgkinson et al.* [1996] use a value of rigidity $3.0x10^{11}$ dyn/cm^2 too calculate geodetic moment from model fault parameters.

bu. *Hanks and Wyss* [1972] do not state value of rigidity used in moment (8.8) calculation but assume $3.3x10^{11}$ dyn/cm^2 when computing moment from field data. Assumed here same value used in estimate of seismic moment. Value or rigidity (2.4) calculated from velocity-density structure used by *Pinar et al.,* [1996] to calculate body-wave moment (11). The body-wave moment (15) of *Stewart and Kanamori* [1982] is not accompanied by information bearing on value of rigidity used. Here assumed to equal $3x10^{11}$ dyn/cm^2.

bv. *Hanks and Wyss* [1972] do not state value of rigidity used in moment (0.9): $3x10^{11}$ dyn/cm^2 assumed for this analysis. *Burdick and Mellman* [1976] report use of rigidity $3.4x10^{11}$ dyn/cm^2 in estimate of body wave moment (1.1). *Butler* [1983] provides no estimate of velocity-density structure or rigidity used in estimate of surface wave moment (1.1): $3x10^{11}$ dyn/cm^2 assumed for this analysis. *Ebel and Helmberger's* [1982] body wave moment (0.7) accompanied by velocity-density structure at source from which rigidity calculated to equal $3.3x10^{11}$ dyn/cm^2. *Swanger et al.* [1978] do not cite value of rigidity used in body wave moment (1.2) but provide velocity-density at assumed 8 km source depth from which rigidity of $3.8x10^{11}$ dyn/cm^2 listed here is calculated. [*Vidale et al.*, 1985] GET Mo… give velocity-density structure at source depth from which rigidity $3.8x10^{11}$ dyn/cm^2 listed here is derived.

bw. *Hartzell and Helmberger* [1982] state rigidity is $2.5x10^{11}$ dyn/cm^2 when extracting displacement from moment estimate (0.5). *Hartzell and Heaton's* [1983] do not state rigidity explicitly in calculation of moment (0.5) but displacements of their model are distributed primarily between 5 and 11 km depth where shear velocity (3.07 km/s) and density (2.67 g/cc) model: rigidity derived from velocity model assumed $2.5x10^{11}$ dyn/cm^2. The surface wave moment (0.7) of *Kanamori and*

Reagan [1982] is computed assuming point source at 9.75 km and velocity-density model 5.08M reported in *Kanamori* [1970], implying rigidity 3.9 $x10^{11}$ dyn/cm^2 used for source excitation functions (but when estimating slip from moment – they assume rigidity of 3.0 $x10^{11}$ dyn/cm^2).

bx. *Fredrich et al*., [1988] provide velocity- density structure at source used to compute seismic moment (15): 3.2 $x10^{11}$ dyn/cm^2

by. Rigidity used to calculate body wave moment (2.1) not cited in original text of source. Value used was $3.3x10^{11}$ dyn/cm^2 (Diane Doser, University of Texas, El Paso, pers. comm). *Mendoza and Hartzell* [1988] provide velocity-density structure used to calculate synthetics and moment (2.3): average rigidity in source region of maximum slip is $2.5x10^{11}$ dyn/cm^2. *Ward and Barrientos* [1986] calculation of moment (2.6) accompanied by use of rigidity of 3.2 $x10^{11}$ dyn/cm^2 when calculating average fault slip yielding best fit of geodetic model deformation to that observed. Inferred that *Barrientos et al. [1987]* calculate moment (2.9) using rigidity of 3.2 $x10^{11}$ dyn/cm^2 : they calculate average fault slip from geodetic moment using this value. Assumed rigidity used in *Tanimoto and Kanamori* 's [1986] surface wave moment (3.5) was 3 $x10^{11}$ dyn/cm^2.

bz. *Fredrich et al*. [1988] provide velocity-density structure at source used to compute seismic moment (.06), from which rigidity is estimated here.

baa. *Wald et al*. [1990] do not state rigidity explicitly in calculation of seismic moment (0.5). They use average value of rigidity rigidity $3.3x10^{11}$ dyn/cm^2 when deriving estimate of stress drop from seismic moment. The centroid moment tensor solution of *Hwang et al*. [1990] (0.8) gives depth of event at 4-6 km. Velocity (Vs=2.6 km/s) – density (2.6 g/cc) structure which equates to rigidity $1.8x10^{11}$ dyn/cm^2. Velocity-density structure used by *Frankel and Wennerberg* [1989] to calculate moment (0.2) implies rigidity of $2.3x10^{11}$ dyn/cm^2. Value of rigidity $3x10^{11}$ dyn/cm^2 assumed for *Sipkin*'s [1989] estimate of moment (1.0): no explicit statement of rigidity or velocity-density structure. Rigidity of $2.8x10^{11}$ dyn/cm^2 used in estimate of moment (0.9) by *Larsen et al*. [1992]. The depth (15km) and velocity-density model of PREM used in centroid solution of *Dziewonki et al. [1989]* indicates rigidity $4.4x10^{11}$ dyn/cm^2 used in estimate of moment (0.7). Note depth is at boundary of upper and lower crust and method assumes velocity-density structure of lower when final location is at boundary (Goran Ekstrom, Harvard University, personal comm. 2005).

bai. *Anderson and Webb* [1989] best estimate of moment (0.4) is for source depth at 8±3 km. Average rigidity at this depth based on velocity-density structure they use is $3.5x10^{11}$ dyn/cm^2. Rigidity values of *Priestly's* [1987] seismic moment estimates from body (0.6) and surface waves (0.9) appear to use average velocity (Vs = 3.6 km/s) and density (2.8 g/cc) at source equivalent to rigidity of $3.6x10^{11}$ dyn/cm^2.

bab. Rigidity of $3.3x10^{11}$ dyn/cm^2 used in *Choy and Bowman's* [1990] estimate of seismic moment (George Choy, USGS, Menlo Park, personal comm., 2005). Value of moment is sum of 3 distinct subevents. Value of Harvard moment tensor catalog is also sum of 3 subevents over span of 12 hours.

baj. Rigidity used in calculation of synthetics and surface wave moment (39) of *Yoshida and Abe* [1992] is $7.3x10^{11}$ dyn/cm^2: derived from shear wave velocity (4.7 km/s) – density (3.3 g/cc) at source depth of 30 km (Yasuhiro Yoshida, Meteorological Research Institute, Japan, personal comm., 2005). Rigidity used in calculation of synthetics and body wave moment (36) of *Yoshida and Abe* [1992] is $4.0x10^{11}$ dyn/cm^2: derived from shear wave velocity (3.74 km/s) – density (2.87 g/cc) at at depth of source (Yasuhiro Yoshida, Meteorological Research Institute, Japan, personal comm., 2005). *Velasco et al*. [1996] use numerous velocity models to find best fitting centroid moment (42) depth between 15 and 45 km: Rigidity at these depths in PREM is $4.4x10^{11}$ dyne/cm^2.

bac. *Cohee and Beroza* [1994] do not provide or recall exact estimate of rigidity (velocity-density structure) used in estimating body wave moment (7) (Greg Beroza, Stanford University, personal comm.., 2005): Value of $3x10^{11}$ dyn/cm^2 assumed. *Dreger* [1994] do not provide velocity-density structure nor explicitly state value of rigidity used in estimate of moment (8): Value of $3x10^{11}$ dyn/cm^2 assumed. Geodetic moment (9) of *Freymueller* [1994] not accompanied by explicit notation of value of rigidity used in model. He generally uses $3.0x10^{11}$ dyn/cm^2 (Jeff Freymueller, University of Alaska, personal comm., 2005), which is used here. *Johnson et al* [1994] do not explicitly state value of rigidity in their use of geodetic data to estimate moment (10): Value of $3x10^{11}$ dyn/cm^2 assumed. *Wald and Heaton* [1994] do not provide information bearing on value of rigidity used in body-wave analysis of moment (7.5): Value of $3x10^{11}$ dyn/cm^2 assumed.

bad. *Zeng and Chen* [2001] use average rigidity of $2.1x10^{11}$ dyn/cm in their estimate of seismic moment (29) (Yuehua Zeng, USGS, Golden, Co, personal comm.). Average value of rigidity of $3x10^{11}$ dyn/cm^2 is estimated here from velocity structure used by *Wu et al* [2001] in their joint inversion of GPS and strong-ground motion observations to calculate moment (27): they do not explicitly state average value displacement or rigidity. Average value of rigidity of $3x10^{11}$ dyn/cm^2 is estimated here from velocity structure used by *Chi* et al. [2001] to determine moment (41): they do not explicitly state average value displacement or rigidity.

bae. *Delouis et al*. [2002] use rigidity $3.3x10^{11}$ dyn/ cm^2 in calculating synthetics for inversion for moment (24). Rigidity of $3.5x10^{11}$ indicated for *Sekiguchi and Iwata's* [2002] estimate of seismic moment (1.5) is derived from velocity-density structure at depth of 10 km. Rigidity for *Li et al*. [2002] moment (22) estimate is that for their velocity-density model structure at 5 to 15km depth. *Feigl et al* [2002] explicity state rigidity $3.3x10^{11}$ dyn/cm used in seismic moment (18) calculation. *Wright et al* [2001] use rigidity $3.4x10^{11}$ dyn/cm^2 in calculation of moment (26).

baf. *Burgmann et al* [2002] use rigidity $3.4x10^{11}$ dyn/cm^2 in estimating moment (5.4). Body-wave analysis of *Umutlu, et al*. [2004] does not state value of rigidity used in moment calculation (5.0) nor estimate of fault slip.

bag. *Berberian et al*. [2001] use Vs=3.7 km/s in body-wave analsysis and estimate of seismic moment (0.91). Assume density of 2.6g/cc yields value of $3.3x10^{11}$ dyne/cm^2 listed. Harvard moment (0.95) is constrained at 15km, a layer boundary in PREM model. Assume here rigidity of lower layer (Goran Ekstron, personal communication). Moment (1.2) derived by Berberian et al by SAR assumes 3.4exp11 dyn/cm^2 for rigidity and is average of two solutions for differing boundary conditions.

bah. *Berberian et al*. [2001] use Vs=3.7 km/s. Assume density of 2.6g/cc yields value of $3.3x10^{11}$ dyne/cm^2 assumed here. Harvard moment (0.95) moment centroid is 15km, a layer boundary in PREM model. Assume here rigidity ($4.4x10^{11}$ dyn/cm^2. of lower layer (Goran Ekstron, personal communication).

bai. Moment (71) estimated from INSAR by *Lasserre et al*. [2005] does not state value of rigidity used in analysis. Value of $3.3x10^{11}$ dyn/ cm^2 assumed. Rigidity of 3 used by *Ozacar and Beck* [2004] in calculation of seismic moments (46) (Arda Ozacar, Dept. of Geological Sciences, University of Arizona, pers. comm.). Rigidity of 4.4 $x10^{11}$ dyne/cm^2 based on PREM and centroid depth for Harvard moment-tensor estimate (59). Rigidity of $3.0x10^{11}$ dyn/ cm^2 used by *Antolik, et al*. [2004] when estimating length parameters from estimated value of seismic moment (50).

baj. Rigidity of $3.3x10^{11}$ dyne/cm^2 derived from velocity model at average source depth of 6 km for Mo (68) estimate of *Frankel* [2004]. *Choy and Boatwright* [2004] do not state value of rigidity used in calculation of seismic moments (38 and 49) . . Rigidity of 3 used by *Ozacar and Beck* [2004] in calculation of seismic moment (56) (Arda Ozacar, Dept. of Geological Sciences, University of Arizona, pers. comm.).Rigidity of 2.6 $x10^{11}$ dyne/cm^2 based on PREM and centroid depth for Harvard moment-tensor estimate (75).

bak. Rigidity of $3.3x10^{11}$ dyne/cm^2 is that assumed by *Abe* [1978] when estimating moment (2.7) from geodetic data.

bal. Moment estimate (6.2) of *Ji et al*. [2002b] does not state nor provide velocity-density structure from which averge rigidity may be calculated. The same is true for the moment estimates (6.8 and 5.9) of *Kaverina et al*. [2002] and [*Jonsson et al*., 2002]. Rigidity value (3.0) used by *Simons et a.l* [2002] when estimating moment (7.0) is average of rigidity structure in upper 15 km of crust [*Jones and Helmberger*, 1998; see figure 10 in *Simons et al*., 2002].

bam. Moment estimates of *Wyss* [1971] for surface (1.9) and body (1.3) wave moments not accompanied by statement of value of rigidity used. Velocity-density model used by *Langston* [1978] to calculte Mo (1.9) equivalent to rigidity of $3.5x10^{11}$ dyne/cm^2. Velocity-density model used by *Langston* [1978] to calculte Mo (1.7) equivalent to rigidity of $3.3x10^{11}$ dyne/cm^2. Dip or 45° taken from analysis of *Heaton* [1982]. Seismicity [*Allen et al*., 1971] extends to depth of about 15 km.

ban. Rigidity of $3.0x10^{11}$ dyne/cm assumed by *Yielding et al*. [1981] Moment estimate (2.5).

Table 3: References cited in Tables 1 and 2

1. [*Sieh*, 1978b] , 2. [Bull and Pearthree, 2002], 3. [Pezzopane and Dawson, 1996], 4. [Matsuda, 1974], 5. [Matsuda et al., 1980], 6. [Wallace, 1980], 7. [Matsuda, 1972], 8. [Barka, 1996], 9. [Trifunac and Brune, 1970], 10. [Kaneda and Okada, 2002], 11. [Tsuya, 1946], 12. [Witkind, 1964], 13. [Caskey et al., 1996], 14. [Clark, 1972], 15. [Johnson and Hutton, 1982]] , 16. [Sharp et al., 1982] , 17. [Crone et al., 1987], 18. [Sharp et al., 1989], 19. [Beanland et al., 1989] , 20. [Nakata, 1990], 21. [Yomogida and Nakata, 1994], 22. [Sieh et al., 1993], 23. [Lin et al., 2001], 24. [Akyuz et al., 2002] , 25. [Cohee and Beroza, 1994; Dreger, 1994; Freymueller, 1994; Johnson et al., 1994; Wald and Heaton, 1994], 26. [Chi et al., 2001; Wu et al., 2001; Zeng and Chen, 2001] , 27. [Doser, 1988], 28. [Burdick and Mellman, 1976; Butler, 1983; Ebel and Helmberger, 1982; Hanks and Wyss, 1972; Heaton and Helmberger, 1977; Swanger et al., 1978; Vidale et al., 1985], 29. [Doser and Smith, 1985; Hanks and Wyss, 1972; Mendoza and Hartzell, 1988; Tanimoto and Kanamori, 1986; Ward and Barrientos, 1986], 30. [Doser, 1990; Hartzell and Heaton, 1983; Hartzell and Helmberger, 1982; Kanamori and Reagan, 1982], 31. [Barrientos et al., 1987; Doser and Kanamori, 1987; Doser and Smith, 1985], 32. [Velasco et al., 1996; Yoshida and Abe, 1992], 33. [Dziewonki et al., 1989; Frankel and Wennerberg, 1989; Hwang et al., 1990; Larsen et al., 1992; Sipkin, 1989; Wald et al., 1990], 34. [Anderson and Webb, 1989; Priestly, 1987] , 35. [Doser, 1986; Hodgkinson et al., 1996], 36. [Doser, 1985; Hodgkinson et al., 1996], 37. [Burgmann et al., 2002; Umutlu et al., 2004], 38. [Delouis et al., 2002; Li et al., 2002; Sekiguchi and Iwata, 2002] , 39. [Hanks and Wyss, 1972; Pinar et al., 1996; Stewart and Kanamori, 1982; Taymaz et al., 1991] , 40. [Kanamori, 1973] , 41. [*Ando*, 1974a; *Kakehi and Iwata*, 1992; *Kikuchi et al.*, 2003] , 42. [Doser, 1990; Doser and Kanamori, 1987; Reilinger, 1984; Thatcher and Hanks, 1973; Trifunac, 1972] , 43. [Crone et al., 1992] , 44. [Choy and Bowman, 1990] , 45. [Fredrich et al., 1988] , 46. [Machette et al., 1993] , 47. [Barka et al., 2002] , 48. [Suter and Contreras, 2002] , 49.[*Lewis et al.*, 1981] , 50. [*Berberian et al.*, 2001] , 51. [*Eberhart-Phillips et al.*, 2003] , 52. [Haeussler et al., 2005] , 53. [Klinger et al., 2005; Lin et al., 2002; Xu et al., 2002] , 54. [Choy and Boatwright, 2004; Frankel, 2004; Ozacar and Beck, 2004] , 55. [Antolik et al., 2004; Lasserre et al., 2005; Ozacar and Beck, 2004] , 56. [Abe, 1978], 57. [Treiman et al., 2002], 58. [*Ji et al.*, 2002a; *Jonsson et al.*, 2002; *Kaverina et al.*, 2002], 59. [*Allen et al.*, 1971; *Allen et al.*, 1975; *Heaton*, 1982; *Langston*, 1978; *Wyss*, 1971], 60. [*Yielding et al.*, 1981], 61. [*Klinger et al.*, 2006]

References

Abe, K. (1978), Dislocations, source dimensions and stresses associated with earthquakes in the Izu Peninusula, Japan, *Journal of Physics of the Earth*, *26*, 253-274.

Aki, K., and P. G. Richards (1980), *Quantitative Seismology: Theory and Methods*, 932 pp., W. H. Freeman, San Francisco, California.

Akyuz, H. S., et al. (2002), Surface rupture and slip distribution of the 12 November 1999 Duzce Earthquake (M 7.1), North Anatolian Fault, Bolu, Turkey, *Bulletin of Seismological Society of America*, *92*, 61-66.

Allen, C. R. (1969), Active faulting in northern Turkey, *Contr. No. 1577*, *Div. Geol. Sci. Calif Inst. Tech.*, 32 pp.

Allen, C. R., et al. (1971), Main shock and larger aftershocks of the San Fernando earthake, February 9 through March 1, 1971, in *The San Fernando, California, earthquake of February 9, 1971*, edited, pp. 17-20, U. S. Government Printing Office, Washington.

Allen, C. R., et al. (1975), Seismological studies of the San Fernando earthqke and their tectonic implications , in *San Fernando, Califoria, earthquake of 9 February 1971*, edited, pp. 257-262, California Division of Mines and Geology, SacramentoCalifornia Division of Mines and Geology.

Allen, C. R., and J. M. Nordquist (1972), Foreshock, mainshock, and larger aftershocks of the Borrego mountain earthquake, in *The Borrego mountain earthquake of April 9, 1968: U. S. Geological Survey Professional Paper*, edited, United States Government Printing Office, Washngton.

Ambraseys, N. N. (1970), Some characteristic features of the North Anatolian fault zone, *Tectonophysics*, *9*, 143-165.

Anderson, H., and T. Webb (1989), The rupture process of the 1987 Edgecumbe earthquake, New Zealand, *New Zealand Journal of Geology and Geophysics*, *32*, 43-52.

Anderson, J. G., and P. Bodin (1987), Earthqake recurrence models and historical seismicity in the Mexicali-Imperial valley, *Bulletin of the Seismological Society of America*, *77*, 562-578.

Ando, M. (1974a), Faulting in the Mikawa earthquake of 1945, *Tectonophysics*, *22*, 173-186.

Ando, M. (1974b), Faulting in the Mikawa Earthquake of 1945 (in accompaniment with Japanese reprint provided by A. Okada with slip measurements but I have lost translation of Journal name), *Tectonophysics*, *22*, 173-186.

Antolik, M., et al. (2004), The 14 November 2001 Kokoxili (Kunlunshan), Tibet, earthquake: Rupture transfer through a large extensional step-over, *Bulletin of the Seismological Society of America*, *94*, 1173-1194.

Barka, A. (1996), Slip distribution along the North Anatolian Fault associated with the large earthquakes of the period 1939 to 1967, *Bulletin of Seismological Society of America*, *86*, 1238-1254.

Barka, A., et al. (2002), The surface rupture and slip distribution of the 17 August 1999 Izmit Earthquake (M 7.4), North Anatolian Fault, *Bulletin of Seismological Society of America*, *92*, 43-60.

Barrientos, S. E., et al. (1987), Comparison of the 1959 Hebgen Lake, Montana and the 1983 Borah Peak, Idaho, earthquakes from geodetic observations, *Bulletin of the Seismological Society of America*, *77*, 784-808.

Beanland, S., et al. (1989), Geological investigations of the 1987 Edgecumbe earthquake, New Zealand, *New Zealand Journal of Geology and Geophysics*, *32*, 73-91.

Ben-Menahem, A., and S. J. Singh (1981), *Seismic waves and sources*, 1108 pp., Springer-Verlag, New York.

Ben-zion (2001), On quantification of the earthquake source, *Seismological Research Letters*, *72*, 1551-1152.

Berberian, M., et al. (2001), The 1998 March 14 Fandoqa earthquake (Mw 6.6) in Kerman province, southeast Iran: re-rupture of the 1981 Sirch earthquake fault, triggering of slip on adjacent thrusts and the active tectonics of the Gowk fault zone, *Geophy. J. Int.*, *146*, 371-398.

Blumenthal, M. (1945a), Ladik deprem atti, *Bull. Mineral Res. Explor. Ints. Turkey*, *1/33*, 153-174.

Blumenthal, M. (1945b), Die Kelkit dislocation und ihre tectonische rolle, *Bull. Mineral Res. Explor. Ints. Turkey*, *2/34*, 372-386.

Bodin, P., and J. N. Brune (1996), On the scaling of slip with rupture length for shallow strike-slip earthquakes: Quasi-static models and dynamic rupture propagation, *Bulletin of the Seismological Society of America*, *86*, 1292-1299.

Brune, J. N. (1968), Seismic moment, seismicity, and rate of slip along major fault zones, *Journal of Geophysical Research*, *73*, 777-784.

Bull, W. B., and P. A. Pearthree (2002), Frequency and size of Quaternary surface ruptures of the Pitaycahic fault, northeastern Sonora, Mexico, *Bulletin of the Seismological Society of America*, *78*, 956-978.

Burdick, L., and G. R. Mellman (1976), Inversion of the body waves from the Borrego Mountain earthquake to source mechanism, *Bulletin of the Seismological Society of America*, *66*, 1485-1499.

Burgmann, R., et al. (2002), Deformation during the 12 November 1999 Duzce, Turkey, earthquake, from GPS and Insar data, *Bulletin of the Seismological Society of America*, *92*, 161-171.

Butler, R. (1983), Surface wave analysis of the 9 April 1968 Borrego mountain earthquake, *Bulletin of the Seismological Society of America*, *73*, 879-883.

Caskey, S. J., et al. (1996), Surface faulting of the 1954 Fairview Peak (Ms=7.2) and Dixie Valley (Ms=6.8) earthquakes, central Nevada., *Bulletin of the Seismological Society of America*, *86*, 286-291.

Chi, W. C., et al. (2001), Finite-source modeling of the 1999 Taiwan (Chi-Chi) earthquake derived from a dense strong-motion network, *Bulletin of the Seismological Society of America*, *91*, 1144-1157.

Choy, G. L., and J. Boatwright (2004), Radiated energy and the rupture process of the Denali fault earthquake sequence of 2002 from broadband teleseismic body waves, *Bulletin of the Seismological Society of America*, *94*, S269-S277.

Choy, G. L., and J. R. Bowman (1990), Rupture process of a multiple main shock sequence; analysis of teleseismic, local, and field observations of the Tennant Creek, Australia, earthquakes of Jan 22, 1988, *Journal of Geophysical Research*, *95*, 6867-6882.

Clark, M. M. (Ed.) (1972), *Surface rupture along the Coyote Creek fault, the Borrego Mountain Earthquake of April 9, 1968*, 55-86 pp., United States Geological Survey.

Cohee, B. P., and G. c. Beroza (1994), Slip distribution of the 1992 landers earthquake and its implications for earthquake source mechanics, *Bulletin of the Seismological Society of America*, *84*, 692-712.

Crone, A., et al. (1987), Surface faulting accompanying the Borah Peak earthquake and segmentation of the Lost River Fault, central Idaho, *Bulletin of Seismological Society of America*, *77*, 739-770.

Crone, A. J., et al. (1992), Geologic Investigations of the 1988 Tennant Creek, Australia, Earthquakes - Implications for paleoseismicity in stable continental regions, *United States Geological Survey Bulletin*, *2032-A*, A1-A51.

Delouis, B., et al. (2002), Joint inversion of InSAR, GPS, Teleseismic, and Strong-motion data for the spatial and temporal distribution of earthquake slip: application to the 1999 Izmit mainshock, *Bulletin of the Seismological Society of America*, *92*, 278-299.

Dewey, J. W. (1976), Seismicity of northern Anatolia, *Bulletin of the Seismological Society of America*, *66*, 843-868.

Doser, D. I. (1985), Source parameters and faulting processes of the 1959 Hebgen lake, Montana, earthquake sequence, *Journal of Geophysical Research*, *90*, 4537-4555.

Doser, D. I. (1986), Earthquake processes in the Rainbow Mountain-Fairview Peak-Dixie Valley, Nevada, region 1954-1959, *Journal of Geophysical Research*, *91*, 12572-12586.

Doser, D. I. (1988), Source parameters of earthquakes in the Nevada seismic zone, 1915-1943, *Journal of Geophysical Research*, *93*, 15001-15015.

Doser, D. I. (1990), Source characteristics of earthquakes along the southern San Jacinto and Imperial fault zones (1937 to 1954), *Bulletin of the Seismological Society of America*, *80*, 1099-1117.

Doser, D. I., and H. Kanamori (1986), Depth of seismicity in the Imperial Valley region (1977-1983) and its relationship to heat flow, crustal structure, and the October 15, 1979, earthquake, *Journal of Geophysical Research*, *91*, 675-688.

Doser, D. I., and H. Kanamori (1987), Long period surface waves of four western United States earthquakes recorded by the Pasadena strainmeter, *Bulletin of the Seismological Society of America*, *77*, 236-243.

Doser, D. I., and R. B. Smith (1985), Source parameters of the 28 October 1983 Borah Peak, Idaho, earthquake from body wave analysis, *Bulletin of the Seismological Society of America*, *75*, 1041-1051.

Dreger, D. (1994), Investigation of the rupture process of the 28 June 1992 landers earthquake utilizing TERRAscope, *Bulletin of the Seismological Society of America*, *84*, 713-724.

Dziewonki, A. M., et al. (1989), Centroid-moment tensor solutions for October-December 1987, *Physics of Earth and Planetary Interiors*, *54*, 10-21.

Ebel, J. E., and D. V. Helmberger (1982), P-wave complexity and fault asperities: the Borrego Mountain, California, earhquake of 1968, *Bulletin of the Seismological Society of America*, *72*, 413-437.

Eberhart-Phillips, D., et al. (2003), The 2002 Denali fault earthquake, Alaska: A large magnitude,slip-partitioned event., *Science*, *300*, 1113-1118.

Engdahl, E. R., et al. (1998), Global teleseismic earthquake location with improved travel times and procedures for depth determination, *Bulletin of the Seismological Society of America*, *88*, 722-743.

Ergin, M., et al. (1999), Aftershock analysis of the August 17, 1999 Izmit, Turkey, Earthquake, in *The 1999 Ismit and Duzce Earthquakes: preliminary results*, edited by A. Barka, et al., pp. 171-178, Istanbul Technical University.

Feigl, K., et al. (2002), Estimating slip distribution for the Izmit mainshock from coseismic GPS, ERS1, RADARSAT, and SPOT measurements, *Bulletin of the Seismological Society of America*, *92*, 138-160.

Frankel, A. (2004), Rupture process of the M 7.9 Denali fault, Alaska, earthquake: Subevents, directivity, and scaling of high-frequency ground motions, *Bulletin of the Seismological Society of America*, *94*, S234-S255.

Frankel, A., and L. Wennerberg (1989), Ruture process of the Ms 6.6 Superstition Hills earthquake determined from strong-motion recordings: application of tomographic source inversion, *Bulletin of the Seismological Society of America*, *79*, 515-541.

Frankel, A. D., et al. (2002), Documentation for the 2002 update of the national seismic hazard maps, *USGS Open-File Report*, *OF 02-0420*, 33 pp.

Fredrich, J., et al. (1988), Source parameters of seven large Australian earthquakes determined by body waveform inversion, *Geophysical Journal of the Royal Astronomical Society*, *95*, 1-13.

Freymueller, J. (1994), The co-seismic slip distribution of the Landers earthquake, *Bulletin of the Seismological Society of America*, *84*, 646-659.

Fuis, G. S., and L. A. Wald (2003), Rupture in south-central Alaska - The Denali fault earthquake of 2002, *U. S. G. S. Fact Sheet*, *014-03*, 4 p.

Graymer, R. W., et al. (2006), Relatively simple throughgoing fault planes at large earthquake depth may be concealed by surface complexity in stepover regions, *submitted for special volume of Geological Society of London preprint and personal communication*.

Haeussler, P. J., et al. (2005), Surface rupture and slip distribution of the Denali and Totschunda faults in the 3 November 2002 M7.9 earthquake, Alaska, *Bulletin of the Seismological Society of America*, *94*, S23-252.

Hamilton, R. M. (1972), Aftershocks of the Borrego Mountain earthquake from April 12 to June 12, 1968, in *The Borrego Mountain earthquake of April 9, 1968: U. S. Geological Survey Professional Paper*, edited, pp. 31-54, U. S. Government Printing Office, Wahsington.

Hanks, T. C. (1977), Earthquake stress drops, ambient tectonic stresses and stresses that drive plate motion, *Pageoph*, *115*, 441-458.

Hanks, T. C., and M. Wyss (1972), The use of body-wave spectra in determination of seismic-source parameters, *Bulletin of the Seismological Society of America*, *62*, 561-589.

Harris, R. A., and S. M. Day (1993), Dynamics of fault interaction - parallel strike-slip faults, *Journal of Geophysical Research*, *18*, 4461-4472.

Harris, R. A., and S. M. Day (1999), Dynamic 3D simulations of earthquakes on en echelon faults, *Geophysical Research Letters*, *98*, 2089-2092.

Hartzell, S. H., and T. Heaton (1983), Inversion of strong groundmotion and teleseismic waveform data for the fault rupture history of the 1979 Imperial Valley, California,

earthquake sequence, *Bulletin of the Seismological Society of America*, *73*, 1553-1584.

Hartzell, S. H., and D. V. Helmberger (1982), Strong-motion modeling of the Imperial Valley earthquake of 1979, *Bulletin of the Seismological Society of America*, *72*, 571-596.

Hauksson, E., et al. (2002), The 1999 Mw 7.1 Hector Mine, California, earthquake sequence: complex conjugate strike-slip faulting, *Bulletin of the Seismological Society of America*, *92*, 1154-1171.

Heaton, T., and D. V. Helmberger (1977), A study of the strong ground motion of the borrego Mountain, California earthquake, *Bulletin of the Seismological Society of America*, *67*, 315-330.

Heaton, T. H. (1982), The 1971 San Fernando earthquake: a double event?, *Bulletin of Seismological Society of America*, *72*, 2037-2062.

Heaton, T. H. (1990), Evidence for and implication of self-healing pulses of slip in earthquake rupture, *Physics of the Earth and Planetary Interiors*, *64*, 1-20.

Hill, D. P., et al. (1990), Seismicity, 180-1986, in *The San Andreas Fault System, California*, edited by R. E. Wallace, pp. 115-152, United States Government Printing Office, Washington, D. C.

Hodgkinson, K. M., et al. (1996), Geometry of the 1954 Fairview Peak-Dixie Valley earthquake sequence from a joint inversion of leveling and triangulation data, *Journal of Geophysical Research*, *101*, 25437-25457.

Hwang, L. J., et al. (1990), Teleseismic source parameters and rupture characteristics of the 24 November 1987, Superstition Hills earthquake, *Bulletin of the Seismological Society of America*, *80*, 43-56.

Ji, C., et al. (2002a), Source description of the 1999 Hector Mine, California, earthquake, Part I: Wavelet domain inversion theory and resolution analysis, *Bulletin of the Seismological Society of America*, *92*, 192-1207.

Ji, C., et al. (2002b), Source description of the 1999 Hector Mine, California, earthquake, Part II: Complexity of slip history, *Bulletin of Seismological Society of America*, *92*, 1208-1226.

Johnson, C. E., and L. K. Hutton (1982), Aftershocks and Preearthquake Seismicity in The Imperial Valley California, Earthquake of October 15, 1979, *United States Geological Survey Professional Paper*, *1254*, 59-76.

Johnson, H. O., et al. (1994), Extremal bounds on earthquake movement from geodetic data - application to the Landers earthquake, *Bulletin of the Seismological Society of America*, *84*, 660-667.

Jones, L. M., and D. V. Helmberger (1998), Earthquake source parametes and fault kinematics of eastern California shear zone, *Bulletin of the Seismological Society of America*, *88*, 1337-1352.

Jonsson, S., et al. (2002), Fault slip distribution of the 1999 Mw 7.1 Hector Mine, California earthquake, etimated from satellite radar and gps measurements, *Bulletin of the Seismological Society of America*, *92*, 1377-1389.

Kakehi, Y., and T. Iwata (1992), Rupture process of the 1945 Mikawa earthquake as determined from strong ground motion records, *Journal of Physics of the Earth*, *40*, 635-655.

Kanamori, H. (1970), Velocity and Q of mantle waves, *Physics of the Earth and Planetary Interiors*, *2*, 259-275.

Kanamori, H. (1973), Mode of strain release associated with major earthquakes in Japan, *Annual Review of Earth and Planetary Sciences*, *1*, 213-239.

Kanamori, H., and D. Anderson (1975), Theoretical basis of some empirical relations in seismology, *Bulletin of Seismological Society of America*, *65*, 1073-1096.

Kanamori, H., and J. Reagan (1982), Long-period surface waves, *U.S. Geological Survey Professional Paper*, *1254*, 55-58.

Kaneda, H., and A. Okada (2002), Surface rupture associated with the 1943 Tottori earthquake: compilation of previous reports and its tectonic geomorphological implications, *Active Fault Research*, *21*, 73-91 (in Japanese with English Abstract).

Kaverina, A., et al. (2002), The combined inversion of seismic and geodetic data for the source process of the 16 ctober 1999 Mw 7.1 Hector Mine, earthquake, *Bulletin of the Seismological Society of America*, *92*, 1266-1280.

Ketin, I. (1948), Uber die tektonisch-mechanischen Folgerungen aus des grossen anatolischen Erdbeben des letzten Dezenniums, *Geol. Rundsch.*, *36*, 77-83.

Ketin, I. (1969), Uber die nordanatolische Horizontalverschiebung, *Bull. Mineral Res. Explor. Ints. Turkey*, *72*, 1-28.

Kikuchi, M., et al. (2003), Source rupture processes of the 1944 Tonankai earthquake and the 1945 Mikawa earthquake derived from low-gain seismograms, *Earth Planets and Space*, *55*, 159-172.

King, G. C. P., and S. G. Wesnousky (2006), xxxxxxx.

King, G. C. P., and S. G. Wesnousky (2007), Scaling of earthquake fault parameters, *Bulletin of Seismological Society of America*, *submitted March for consideration of publication.*

Klinger, Y., et al. (2006), Evidence for an earthquake barrier model from Mw~7.8 Kokozili (Tibet) earthquake slip distribution, *Earth and Planetary Science Letters*, *242*, 354-364.

Klinger, Y., et al. (2005), High-resolution satellite imagery mapping of the surface rupture and slip distribution of the Mw ~7.8, 114 November 2001 Kokoxili earthquake, Kunlun fault, northern Tibet, China, *Bulletin of the Seismological Society of America*, *95*, 1970-1987.

Kocyigit, A. (1989), Susehri Basin; an active fault wedge bnasin, *Tectonophysics*, *167*, 13-29.

Kocyigit, A. (1990), Tectonic setting of the Golova basin; total offset of the North Anatolian fault zone, E Pontide, Turkey, *Annales Tectonicae*, *IV*, 155-170.

Kramer, S. L. (1996), *Geotechnical earthquake engineering*, 653 pp., Prentice Hall, Upper Saddle River, N. J.

Langston, C. A. (1978), The February 9, 1971 San Fernando earthquake: A study of source finiteness in teleseismic body waves, *Bulletin of Seismological Society of America*, *68*, 1-29.

Langston, C. A. (1987), Depth of faulting during the 1968 Meckering, Australia, earthquake sequence determined from wave form analysis of local seismograms, *Journal of Geophysical Research*, *92*, 11561-11574.

Larsen, S., et al. (1992), Global positioning system measurements of deformations associated with the 1987 Superstition Hills earthquake, *Journal of Geophysical Research*, *97*, 4885-4902.

Lasserre, C., et al. (2005), Coseismic deformation of the 2001 M-w=7.8 Kokoxili earthquake in Tibet, measured by synthetic aperture radar interferometry, *Journal of Geophysical Research-Solid Earth*, *110*.

Lewis, J. D., et al. (1981), The Cadeaux earthquake, 2 June 1979, *Geological Survey of Western Australia*, *Report 11*, 134 pp.

Li, X., et al. (2002), Complex source process of the 17 August 1999 Izmit, Turkey, earthquake, *Bulletin of the Seismological Society of America*, *92*, 267-277.

Lin, A., et al. (2002), Co-seismic strike-slip and rupture length produced by the 2001 Ms 8.1 central Kunlun earthquake, *Science*, *296*, 2015-2017.

Lin, A., et al. (2001), Co-seismic displacements, folding and shortening structures along the Chelungpu surface rupture zone occurred during the 1999 Chi-Chi (Taiwan) earthquake, *Tectonophysics*, *330*, 225-244.

Lin, C.-H. (2001), The 1999 Taiwan earthquake: A proposed stress-focusing, heel-shaped model, *Bulletin of the Seismological Society of America*, *91*, 1053-1061.

Machette, M. N., et al. (1993), Geologic investigations of the 1986 Marryat Creek, Australia, earthquake - implications for paleoseismicity in stable continental regions, *United States Geological Survey Bulletin*, *2032 B*, p. 29p.

Magistrale, H., et al. (1989), The Superstition Hills, California, earthquakes of 24 November 1987, *Bulletin of the Seismological Society of America*, *79*, 239-252.

Matsuda, T. (1972), Surface faults associated with Kita-Izu Earthquake of 1930 in Izu Peninsula, Japan, in *Izu Peninsula*, edited by M. Hoshino and H. Aoki, pp. 73-102., Tokai University Press, Tokyo.

Matsuda, T. (1974), Surface faults associated with Nobi (Mino-Owari) Earthquake of 1891, Japan, *Bulletin of Earthquake Research Institute, University of Tokyo*, *13*, 127-162.

Matsuda, T., et al. (1980), The surface faults associated with the Rikuu Earthquake of 1896, *Bulletin of Earthquake Research Institute, University of Tokyo*, *55*, 795-855.

McCann, W. R., et al. (1979), Seismic gaps and plate tectonics: seismic potential for major boundaries, *Pageoph*, *117*, 1082-1147.

McKenzie, D. (1972), Active tectonics of theMediterranean region, *Geophy. Journal Royal Astronomical Society*, *30*, 109-185.

Mendoza, C., and S. H. Hartzell (1988), Inversion for slip distribution using teleseismic P waveforms: North Palm Springs, Borah Peak, and Michoacan earthquakes., *Bulletin of the Seismological Society of America*, *78*, 1092-1111.

Milkereit, C., et al. (1999), Preliminary aftershock analysis of the Mw=7.4 and Mw=7.1 Duzce earthquake in western Turkey, in *1999 Izmit and Duzce earthquakes: preliminary results*, edited by A. Barka, et al., pp. 179-187, Istanbul Technical University.

Nakata, T. (1990), Surface faulting associated with the Philippine earthquake of 1990 (in Japanese), *Journal of Geography*, *99*, 95-112.

Nakata, T., et al. (1998), Fault branching and directivity of rupture propagation (in Japanese), *Journal of Geography*, *107*, 512-528.

Oglesby, D. D. (2005), The dynamics of strike-slip step-overs with linking dip-slip faults, *Bulletin of the Seismological Society of America*, *95*, 1604-1622.

Ozacar, A. A., and S. L. Beck (2004), The 2002 Denali fault and 2001 Kunlun fault earthquakes: Complex rupture processes of two large strike-slip events, *Bulletin of the Seismological Society of America*, *94*, S278-S292.

Ozturk, A. (1980), Lakik-Destek yoresinin tektonigi, *Bull. Geol. Soc. Turkey*, *23*, 31-38.

Pamir, H. N., and H. Aykol (1943), Corm ve Erbaa depremieri Tek. tonigi, *Bull. Eaerth Sci. Cumhuriyet Univ*, *2*, 35-52.

Pamir, H. N., and I. Ketin (1941), Das Anatolische Erdeben Ende 1939, *Geol. Rundsch.*, *32*, 278-287.

Petersen, M. D., and S. G. Wesnousky (1994), Fault Slip Rates and Earthquake Histories for Active Faults in Southern California, *Bulletin of the Seismological Society of America*, *84*, 1608-1649.

Pezzopane, S. K., and T. E. Dawson (1996), Fault displacement hazard: A summary of issues and information, in *Seismotectonic Framework and Characterization of Faulting at Yucca Mountain*, edited by J. W. Whitney, pp. 9-1 - 9-160.

Pinar, A., et al. (1996), A rupture model for the 1967 Mudurnu Valley, Turkey earthquake and its implication for seismotectonics in the western part of the North anatolian fault zone, *Geophysical Research Letters*, *23*, 29-32.

Press, W. H., et al. (1992), *Numerical recipes in Fortran: An art of scientific computing*, 2nd ed., 963 pp., Cambridge University Press.

Priestly, K. F. (1987), Source parameters of the 1987 Edgecumbe earthquake, New Zealand, *New Zealand Journal of Geology and Geophysics*, *32*, 53-59.

Reilinger, R. (1984), Coseismic and postseismic vertical movements associated with the 1940 M 7.1 Imperial Valley, California, earthquake, *Journal of Geophysical Research*, *89*.

Research, G. f. A. F. (1991), *Active faults in Japan: sheet maps and inventories*, 437 pp., University of Tokyo Press, Tokyo.

Richins, W. D., et al. (1987), The 1983 Borah Peak, Idaho, earthquake and its aftershocks, *Bulletin of the Seismological Society of America*, *77*, 694-723.

Robinson, R. (1989), Aftershocks of the 1`987 Edgecumbe earthquake, New Zealand: seismological and structural studies using portab le seismographs in the epicentral region, *New Zealand Journal of Geology and Geophysics*, *32*, 61-72.

Romanowicz, B. (1994), Comment on "A reappraisal of large earthquake scaling", *Bulletin of the Seismological Society of America*, *84*.

Rowland, J. V., and R. H. Sibson (2004), Structural controls on hydrothermal flow in a segmented rift system, Taupo Volcanic Zone, New Zealand, *Geofluids*, *4*, 259-283.

Ryall, A. (1962), The Hebgen Lake Montana, earthquake of August 17, 1959, *Bulletin of Earthquake Research Institute, University of Tokyo*, *52*, 235-271.

SCEC, W. G. (1994), Seismic Hazards in Southern California: Probable Earthquakes, 1994-2024, *Bulletin of the Seismological Society of America*, *85*, 379-439.

Scholz, C. (1982a), Scaling laws for large earthquakes: consequences for physical models, *Bulletin of Seismological Society of America*, *72*, 1-14.

Scholz, C. (1982b), Scaling relations for strong ground motion in large earthquakes, *Bulletin of Seismological Society of America*, *72*, 1903-1909.

Scholz, C. H. (1994), Reply to comment on"A reapprasial of large earthquake scaling", *Bulletin of the Seismological Society of America*, *84*, 1677-1678.

Segall, P., and D. D. Pollard (1980), Mechanics of discontinuous faults, *Journal of Geophysical Research*, *85*, 4337-4350.

Sekiguchi, H., and T. Iwata (2002), Rupture process of the 199 Kocaeli, Turkey, earthquake estimated from strong motion waveforms, *Bulletin of the Seismological Society of America*, *92*, 300-311.

Sharp, R., et al. (1989), Surface faulting along the Superstition Hills fault zone and nearby faults associated with the earthquakes of 24 November 1987, *Bulletin of Seismological Society of America*, *79*, 252-281.

Sharp, R., et al. (1982), Surface faulting in the Central Imperial Valley in 'The Imperial Valley California, Earthquake of October 15, 1979, *United States Geological Survey Professional Paper*, *1254*.

Shibutani, T. (1991), Search for the buried subfault(s) of the 16 July 1990 Luzon earthquake, the Phililppines, using aftershock observations, *J. Natural Disas. Sci*, *13*, 29-38.

Sibson, R. H. (1985), Stopping of earthquake ruptures at dilational fault jogs, *Nature*, *316*, 248-251.

Sieh, K., et al. (1993), Near-field investigations of the Landers earthquake sequence, April to July 1992, *Science*, *260*, 171-176.

Sieh, K. E. (1978a), Central California foreshocks of the great 857 earthquake, *Bulletin of the Seismological Society of America*, *68*, 1731-1749.

Sieh, K. E. (1978b), Slip along the San Andreas Fault associated with the great 1857 earthquake, *Bulletin of the Seismological Society of America*, *68*, 1421-1448.

Simons, M., et al. (2002), Coseismic deformation from the 1999 Mw 7l.1 Hector Mine, California, earthquake as inferred from InSAR and GPS observations, *Bulletin of the Seismological Society of America*, *92*, 1390-1402.

Simpson, R. W., et al. (2006), San Andreas fault geometry in the Parkfield, California region., *Bulletin of Seismological Society of America*, *in press*.

Sipkin, S. A. (1989), Moment-tensor solutions for the 24 November 1987 Superstition Hills, California earthquake, *Bulletin of the Seismological Society of America*, *79*, 493-499.

Stein, R. S., et al. (1997), Progressive failure on the North Anatolian fault since 1939 by earthquake stress triggering, *Geophysical Journal International*, *128*, 594-604.

Stewart, G. S., and H. Kanamori (1982), Complexity of rupture in large strike-slip earthquakes in Turkey, *Physics of Earth and Planetary Interiors*, *28*, 70-84.

Suter, M., and J. Contreras (2002), Active tectonics of northeastern Sonora, Mexico (southern Basin and Range Province) and the 3 May 1887 Mw 7.4 Earthquake, *Bulleting of the Seismological Society of America*, *92*, 581-589.

Swanger, H. J., et al. (1978), Simulation of strong-motion displacements using surface-wave modal superposition, *Bulletin of the Seismological Society of America*, *68*, 907-922.

Takagi, A., et al. (1977), Seismic activity in the northeastern Japan arc, *Journal of Physics of Earth*, *25*, S95-S104.

Tanimoto, T., and H. Kanamori (1986), Linear programming approach to moment tensor inversion of earthquake sources and some tests on the three-dimensional structure of the upper mantle, *Geophy. J. R. Astron. Soc.*, *84*, 413-430.

Tasman, C. E. (1944), Gerede-Bou depremi, *Bull. Mineral Res. Explor. Ints. Turkey*, *1/31*, p. 134.

Taymaz, T., et al. (1991), Active tectonics of the north and central Aegean sea, *Geophy. J. Int.*, *108*, 589-603.

Thatcher, W., and T. C. Hanks (1973), Source parameters of southern California earthquakes, *Journal of Geophysical Research*, *78*, 8547-8576.

Thatcher, W., et al. (1980), Lithospheric loading by the 1896 Riku-u earthquake, northern Japan - implications for plate flexure and asthenospheric rheology, *Journal of Geophysical Research*, *85*, 6429-6435.

Treiman, J., et al. (2002), Primary surface rupture associated with the Mw 7.1 16 October 1999 Hector Mine earthquake, San Bernardino County, California, *Bulletin of the Seismological Society of America*, *92*, 1171-1191.

Trifunac, M. D. (1972), Tectonic stress and the source mechanism of the Imperial Valley, California, earthquake of 1940, *Bulletin of the Seismological Society of America*, *62*, 1283-1302.

Trifunac, M. D., and J. Brune (1970), Complexity of energy release during the Imperial Valley, California, earthquake of 1940, *Bulletin of Seismological Society of America*, *60*, 137-160.

Tsuya, K. (1946), The Fukozu fault. A remarkable earthquake fault formed during the Mikawa earthquake of January 13, 1945., *Bull. Earthquake Research Institute, Tokyo University*, *24*, 59-76 (in Japanese with English abstract).

Umutlu, N., et al. (2004), The rupture process during the 1999 Duzce, Turkey, earthquake from joint inversion of teleseismic and strong-motion data, *Tectonophysics*, *391*, 315-324.

Velasco, A. A., et al. (1996), Rupture process of the 1990 Luzon, Phillippines (Mw=7.7) earthquake, *Journal of Geophysical Research*, *101*, 22419-22434.

Vidale, J., et al. (1985), Finite difference seismograms for SH waves, *Bulletin of the Seismological Society of America*, *75*, 1765-1782.

Wald, D. J., and T. Heaton (1994), Spatial and temporal distribution of slip for the 1992 Landers, California, earthquake, *Bulletin of the Seismological Society of America*, *84*, 668-691.

Wald, D. J., et al. (1990), Rupture process of the 1987 Superstition Hills earthquake from the inversion of strong-motion data, *Bulletin of the Seismological Society of America*, *80*, 1079-1098.

Wallace, R. E. (1980), Map of fault scarps formed during earthquake of October 2, 1915, Pleasant Valley, Nevada, and other young fault scarps, in *U.S. Geological Survey Open File Report*, edited, U. S. Geological Survey, Reston, VA.

Ward, S. N., and S. E. Barrientos (1986), An inversion for slip distribution and fault shape from geodetic observations of the 1983 Borah Peak, Idaho, earthquake, *Journal of Geophysical Research*, *91*, 4909-4919.

Wesnousky, S. (1988), Seismological and structural evolution of strike-slip faults, *Nature*, *335*, 340-342.

Wesnousky, S. G. (1986), Earthquakes, Quaternary faults, and seismic hazard in California, *Journal of Geophysical Research*, *91*, 12,587-512,631.

Wesnousky, S. G. (2006), Predicting the endpoints of earthquake ruptures, *Nature*, *444*, 358-360.

Wesnousky, S. G., et al. (1982), Deformation of an island arc: Ratges of moment-release and crustal shortening in intraplate Japan determined from seismicity and Quaternary fault data, *Journal of Geophysical Research*, *87*, 6829-2852.

Wesnousky, S. G., et al. (1984), Integration of geological and seismological data for the analysis of seismic hazard: A case study of Japan, *Bulletin of the Seismological Society of America*, *74*, 687-708.

Witkind, I. J. (1964), Reactivated faults north of Hebgen Lake, *U.S. Geological Survey Professional Paper*, *435-G*, 37-50.

Wright, T. J., et al. (2001), Triggered slip: observatons of the 17 August 1999 Ismit (Turkey) earthquake using radar interferometry, *Geophysical Research Letters*, *28*, 1079-1082.

Wu, C. J., et al. (2001), Source process of the Chi-Chi earthquake: a joint inversion of strong motion data and global positioning system data with multifault model, *Bulletin of the Seismological Society of America*, *91*, 1128-1143.

Wyss, M. (1971), Preliminary source parameter determination of the San Fernando earthquake, in *The San Fernando, California, earthquake of February 9, 1971*, edited, pp. 38-40, U. S. Government Printing Office, Washington.

Xu, X., et al. (2002), Surface rupture of the Kunlunshan earthquake (Ms 8.1), northern Tibetan plateau, China, *Seismological Research Letters*, *73*, 884-892.

Yielding, G., et al. (1981), Relations between surface deformation, fault geometry, seismicity, and rupture characteristics during the El Asnam (Algeria) earthquake of 10 October 1980, *Earth and Planetary Science Letters*, *56*, 287-304.

Yomogida, K., and T. Nakata (1994), Large slip velocity of the surface ruptures associated with the 1990 Luzon earthquake, *Geophysical Research Letters*, *21*, 1799-1802.

Yoshida, Y., and K. Abe (1992), Source Mechanism of the Luzon, Philippines earthquake of July 16, 1990, *Geophysical Research Letters*, *19*, 545-548.

Zeng, Y., and C. H. Chen (2001), Fault rupture process of the 20 September 1999 Chi-Chii, Taiwan earthquake, *Bulletin of the Seismological Society of America*, *91*, 1088-1098.

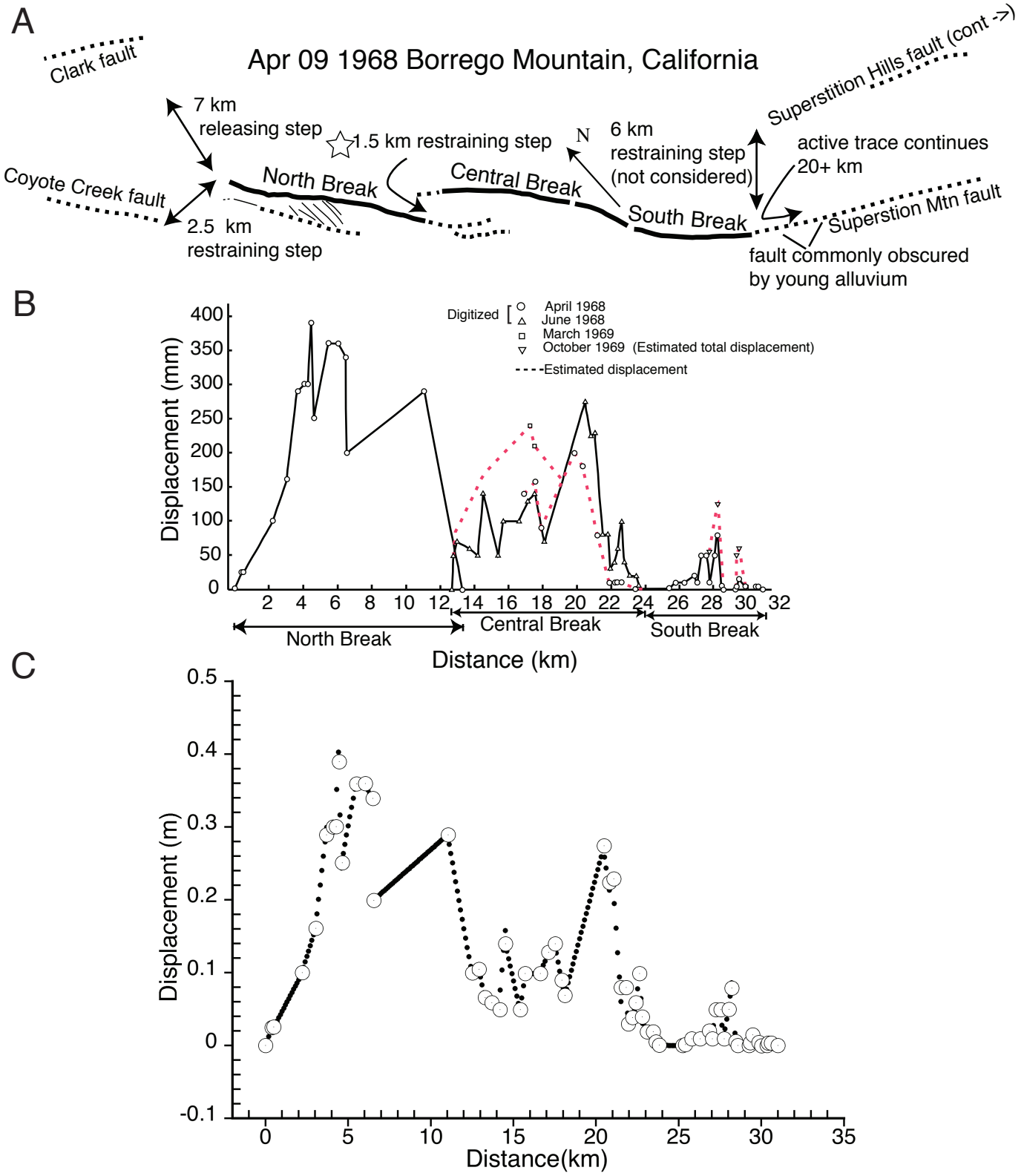

Figure 1. Illustration of data synthesis and analysis. (A) Map of 1968 Borrego Mountain earthquake rupture trace shown as bold lines. Adjacent and continuing traces of active faults that did not rupture during the earthquake are shown as thinner dotted lines. Also annotated are the dimensions of fault steps measured approximately perpendicular to fault strike and the distance to the nearest neighboring fault from the 1968 rupture endpoints. (B) Geologic measurements of surface slip along the rupture trace. (C) Plot of digitization of slip curve showing both field measurements (large circles) and interpolated values (small solid circles). Similarly annotated maps and plots for all earthquakes used in study (Table 1) are compiled in Appendix 1. Reference to map and slip curve sources are given in Table 1.

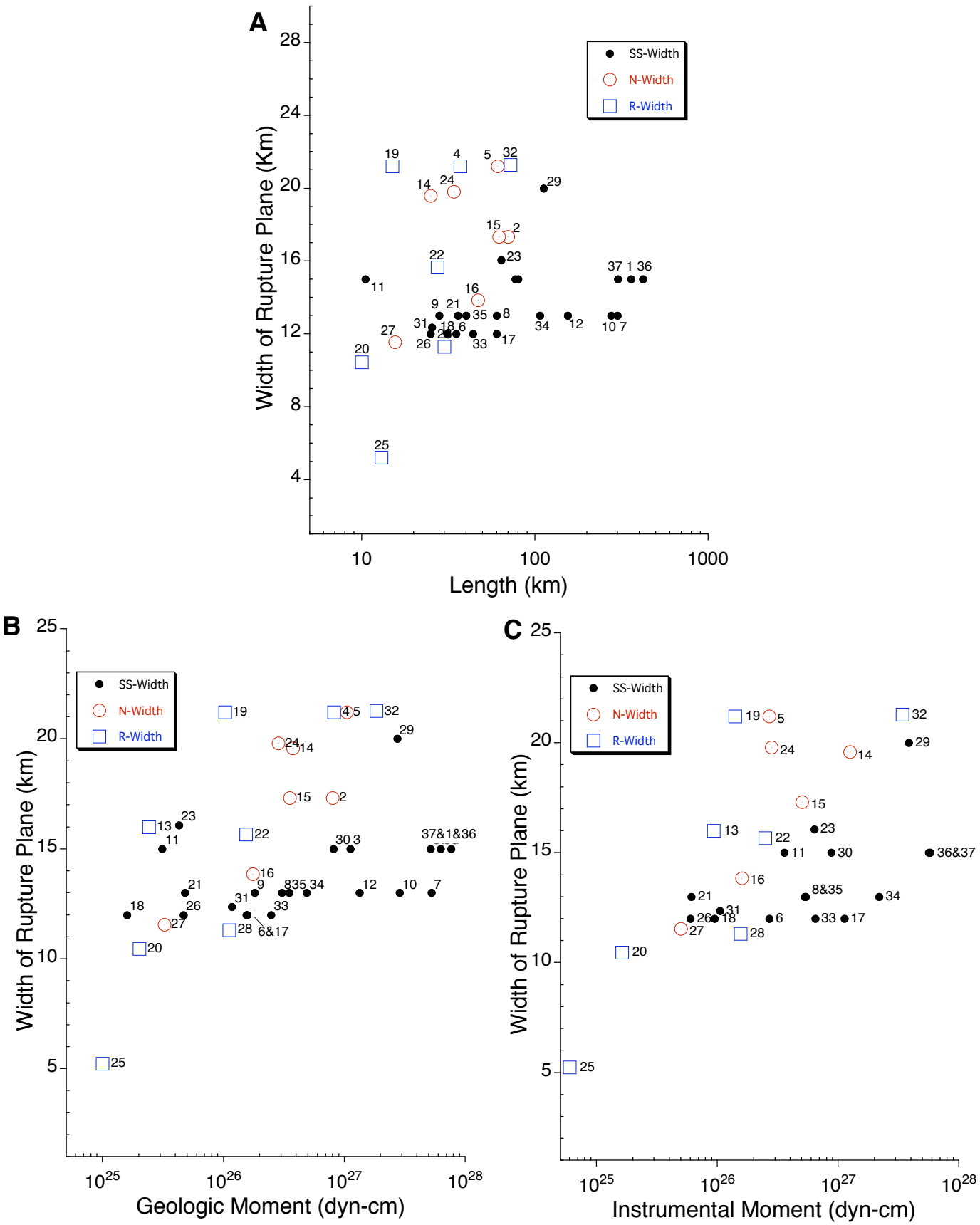

Figure 2. Rupture width as a function of (A) rupture length and (B) geologic moment and (C) seismic moment for events in Table 1. Note 1945 Mikawa (13) and 199 Izmit (34) rupture lengths are minimum because they do not include offshore extent of rupture.

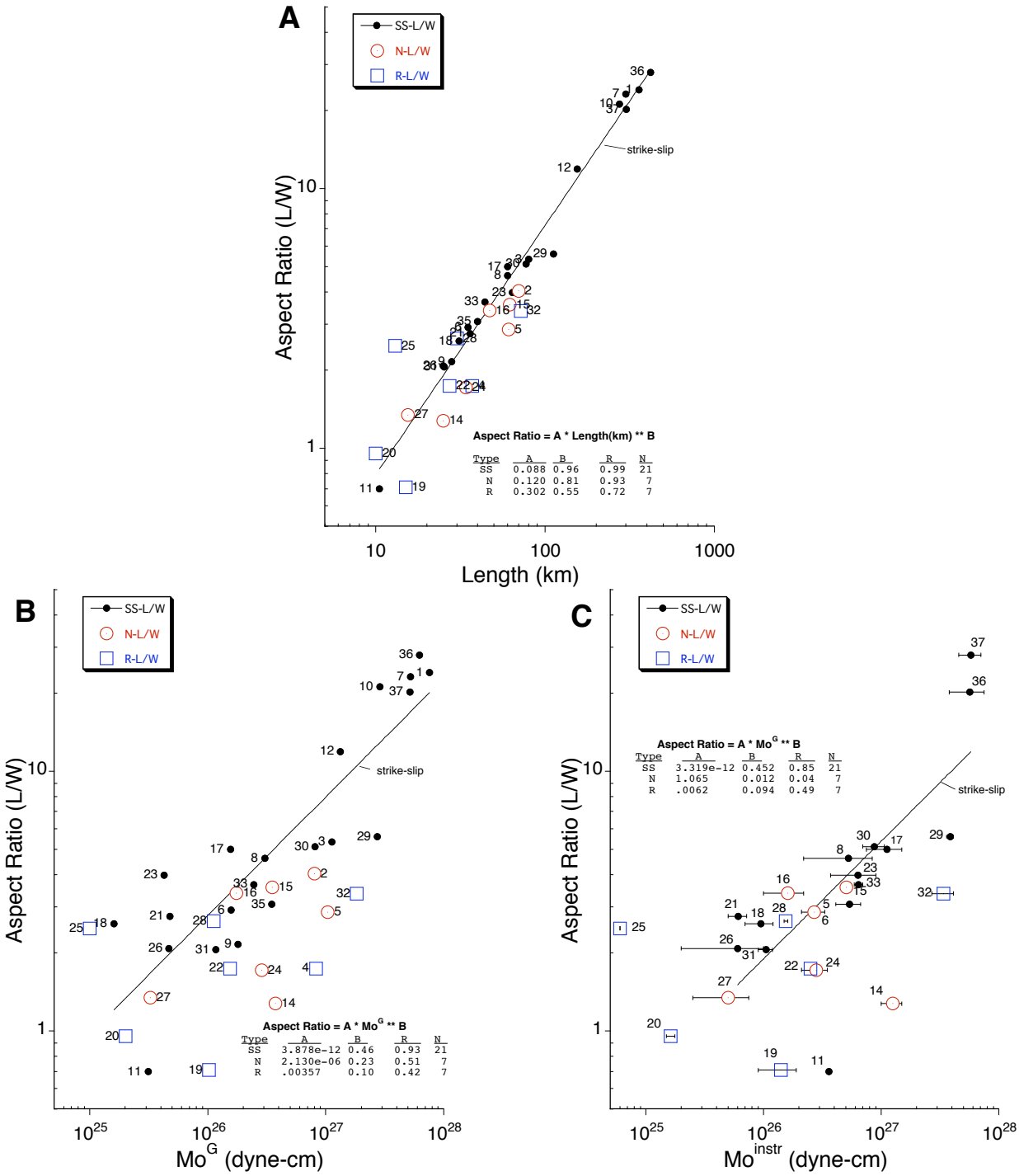

Figure 3. Aspect Ratio (L/W) as function of (a) surface rupture length (L) and moment Mo derived from (b) geological and (c) instrumental measurements, respectively. Numbers correspond to events listed in Table 1. Horizontal bars in (c) represent range of seismic moments reported by independent investigators and listed in Table 2. Parameters describing regression of power-law curve for each strike-slip, normal, and reverse faults are listed separately. Regression curve is shown only for strike-slip. The 1945 Mikawa and 1999 Izmet extend offshore and are not plotted nor included in regressions.

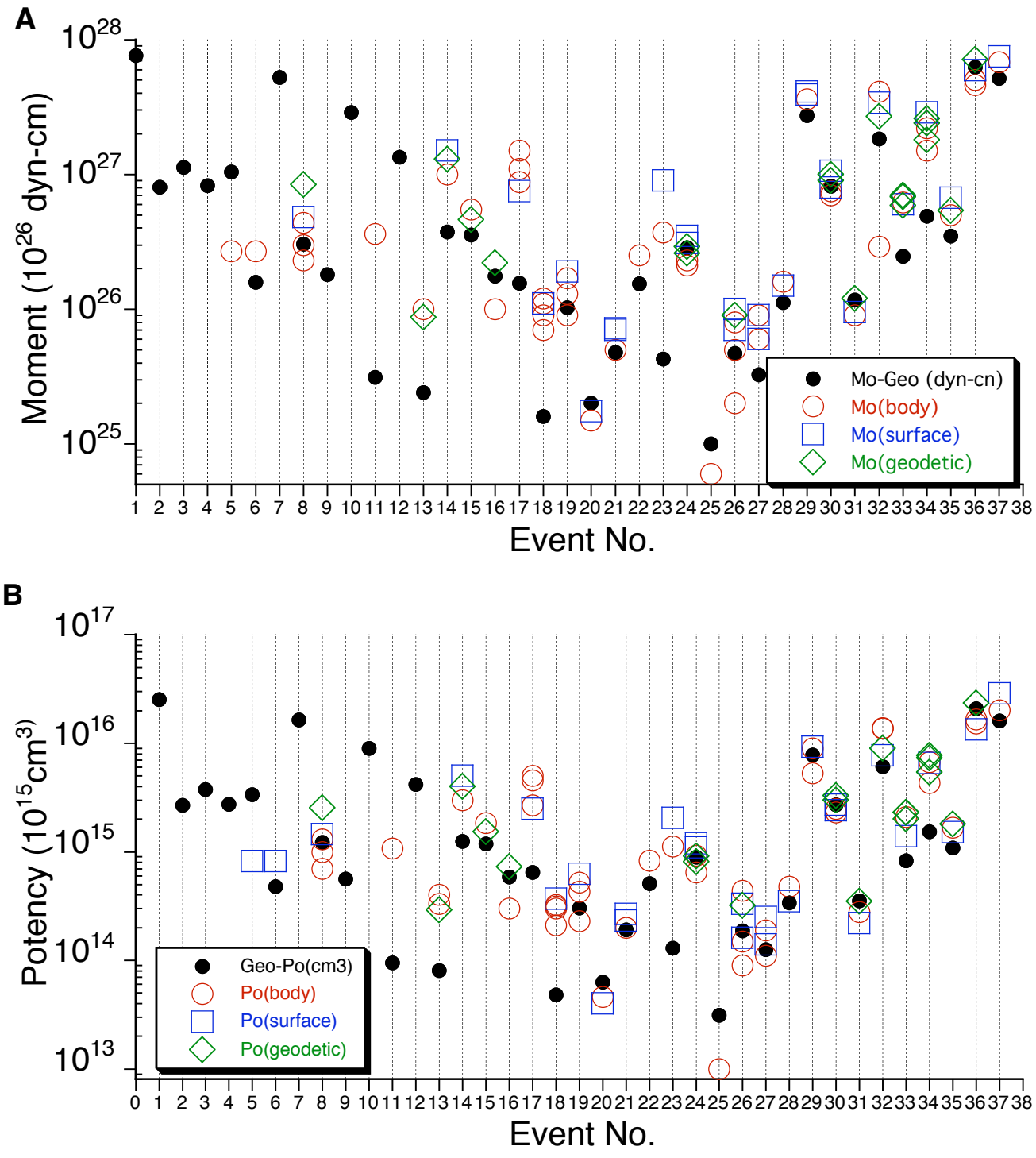

Figure 4. Geologically and instrumentally derived (A) seismic moments and (B) potencys plotted versus event number for events listed in Tables 1 and 2. Geologic values for events 13 (1945 Mikawa) and 34 (1999 Izmit) do not include portion of faults that extended offshore and are for that reason minimum values.

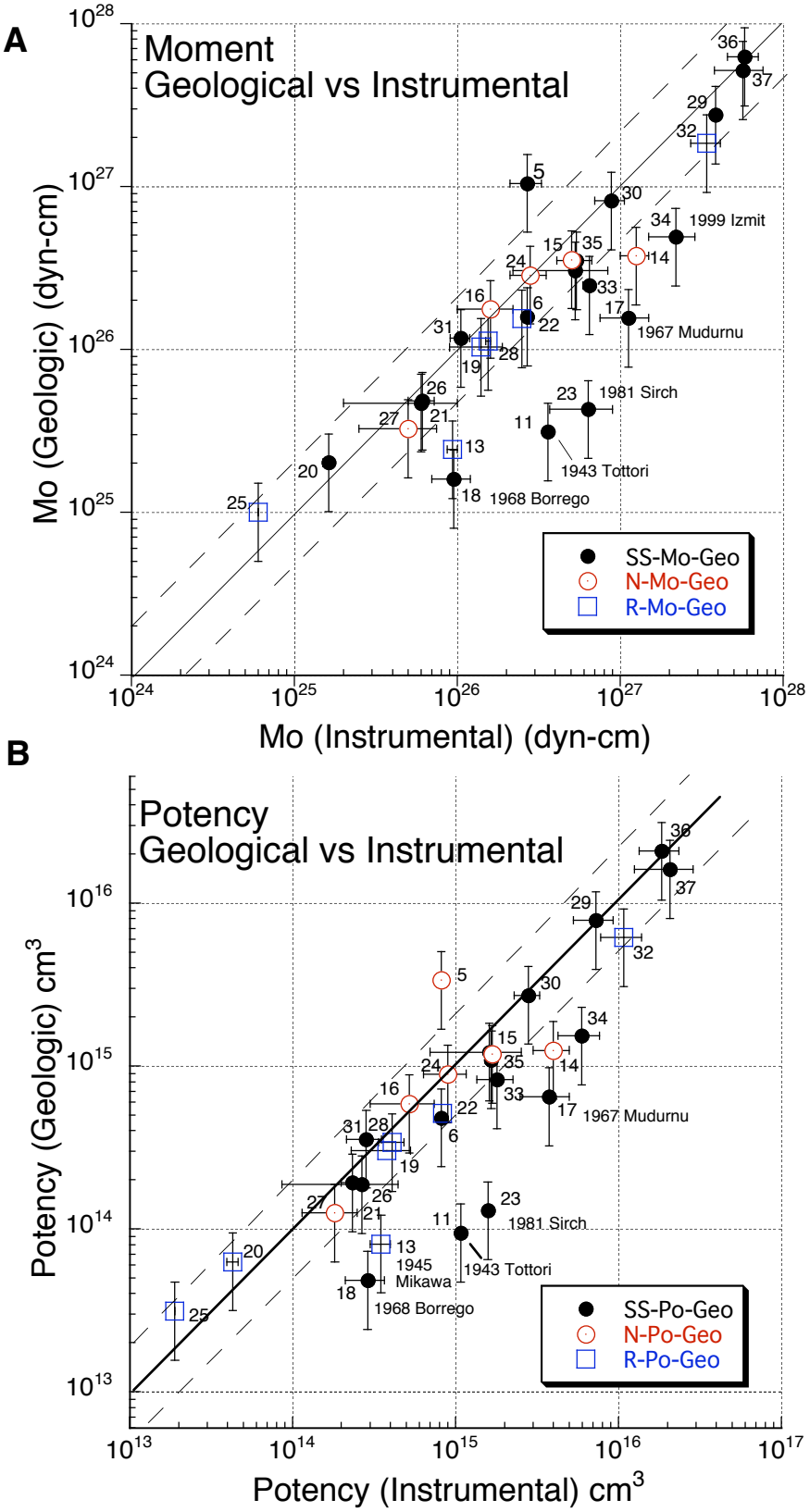

Figure 5. Geologically versus instrumentally derived estimates of (A) moment and (B) potency. Vertical bars represent a factor of 3 in geologic moment. Horizontal bars reflect the spread of multiple measures of seismic moment reported by independent investigators. Perfect correlation would follow solid line of slope 1. Dashed lines fall a factor of 2 about solid line of slope 1. The number next to each symbol corresponds to the listing of events in Table 1.

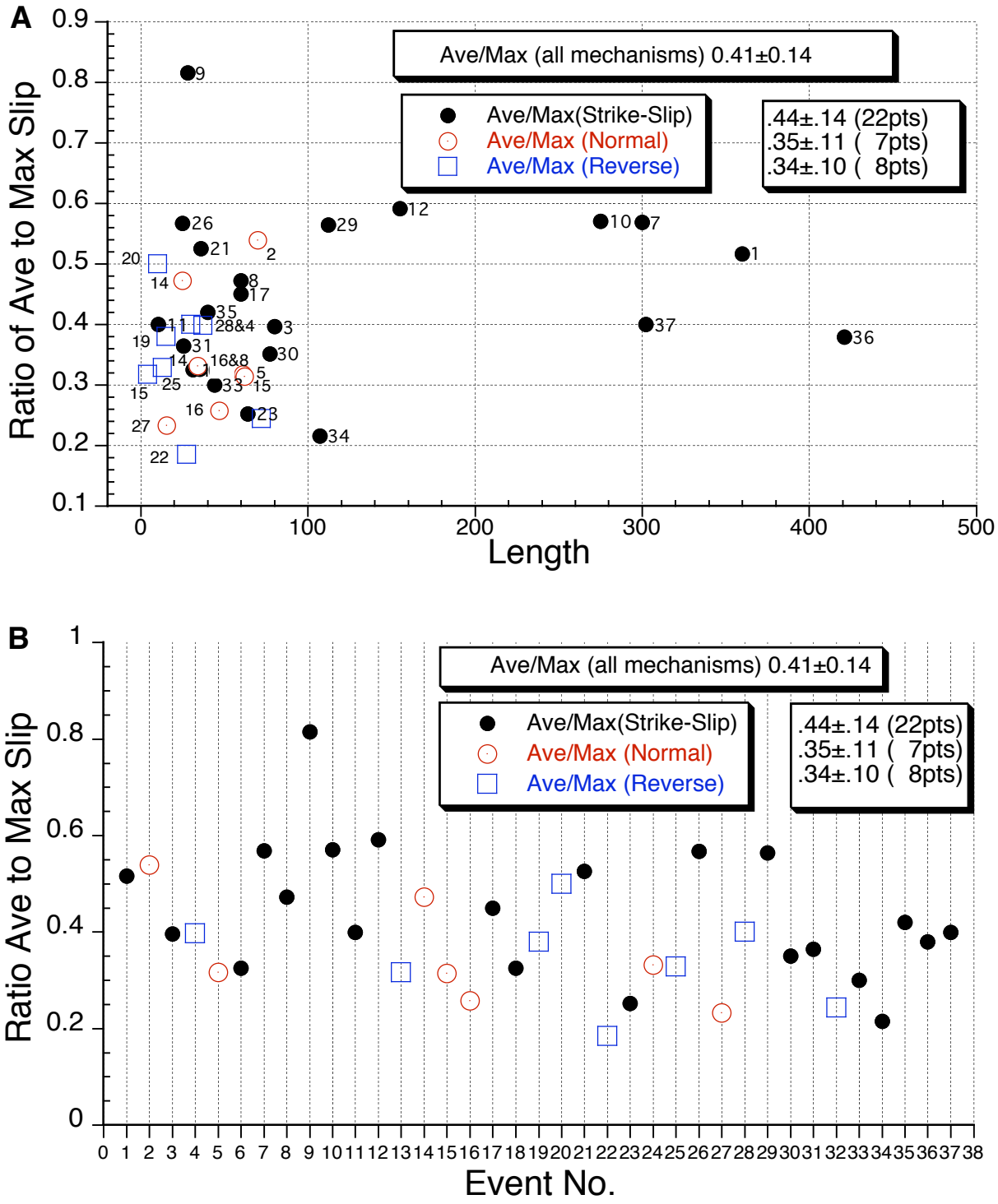

Figure 6. Ratio of average to maximum surface slip as function of (A) rupture length and (B) event number. Data point symbols differ according to fault mechanism. Average value of ratio, standard deviation, and number of points (pts) are given in key. Event numbers correspond to earthquakes listed in Table 1.

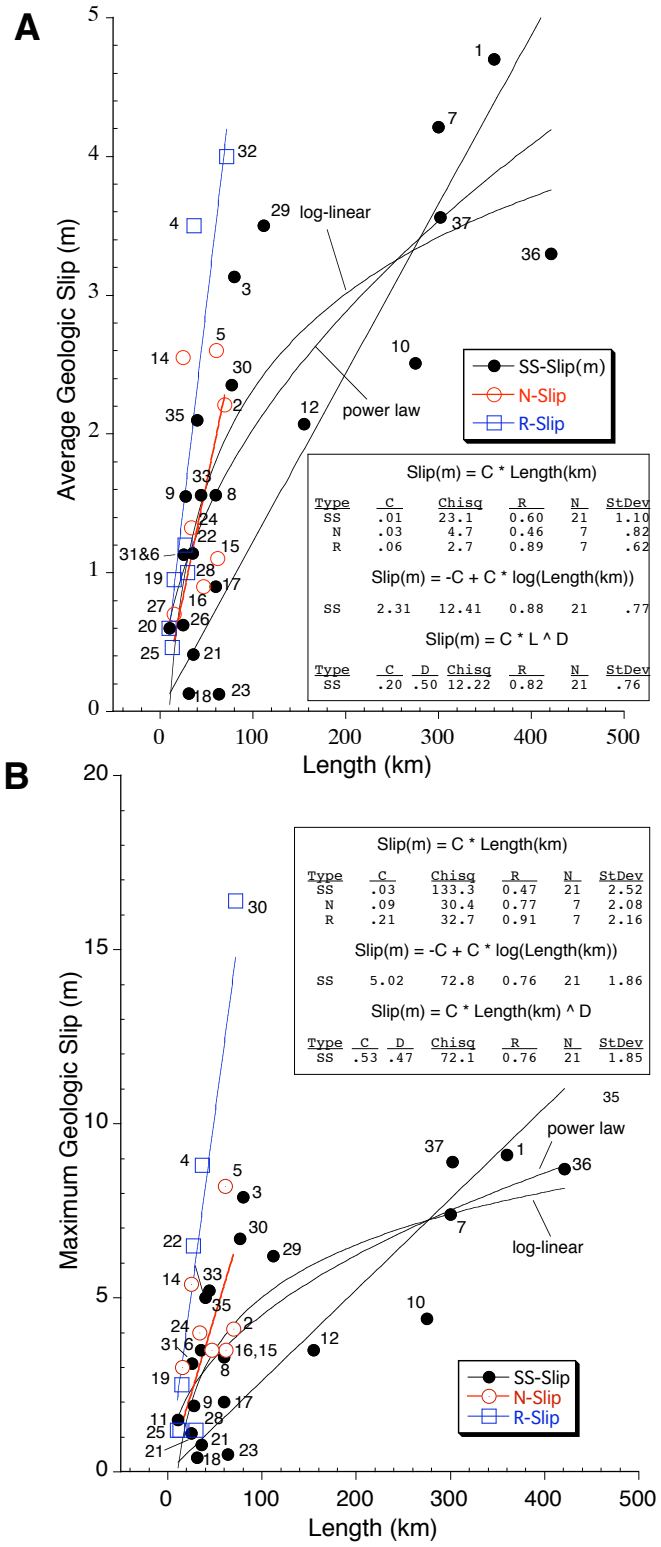

Figure 7. (A) Average and (B) maximum values of coseismic surface slip versus rupture length for earthquakes listed in Table 1. The 1945 Mikawa earthquake and 1999 Izmet earthquake ruptures extended offshore and are not included. Values derived from digitized slip distribution curves.

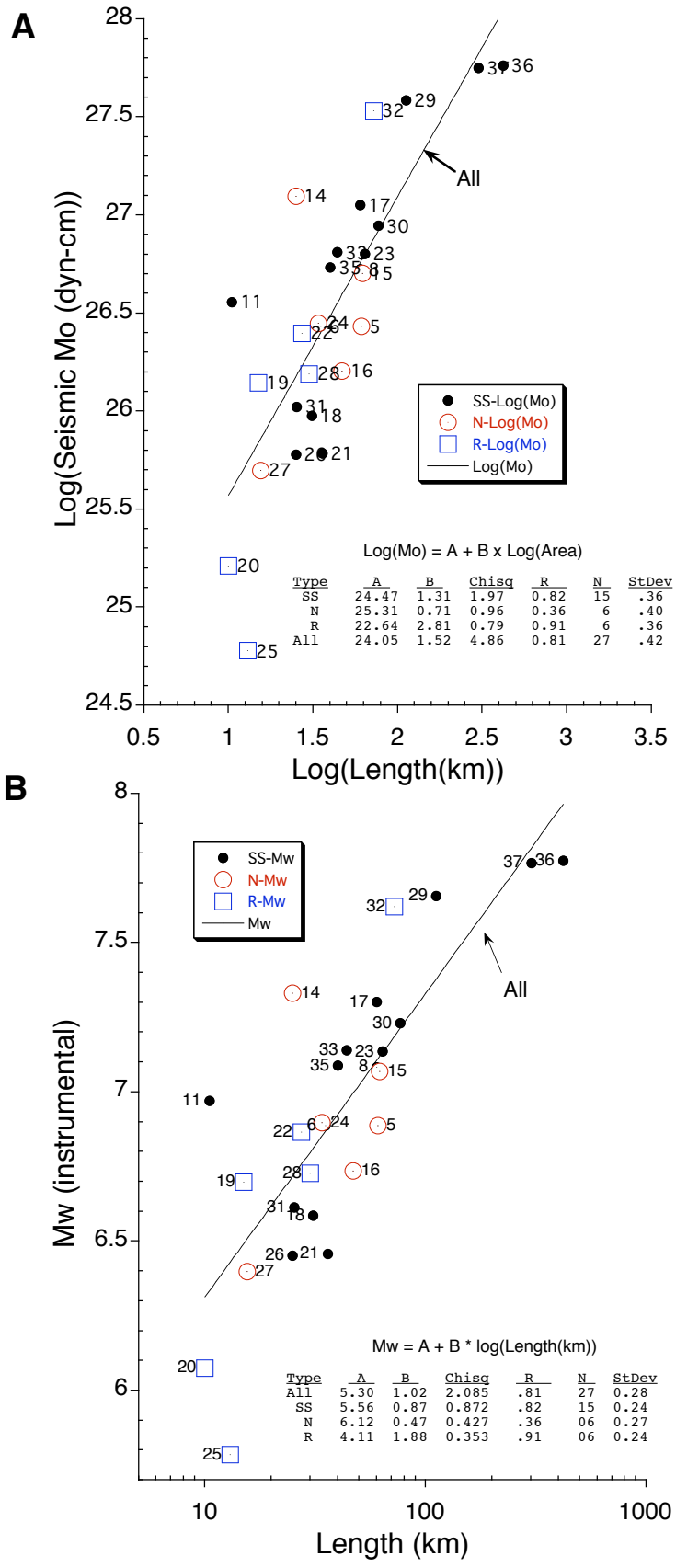

Figure 8. Instrumental measures of (A) Mw and (B) Log(Mo) versus rupture length L and Log(L), respectively for earthquakes listed in Table 1.

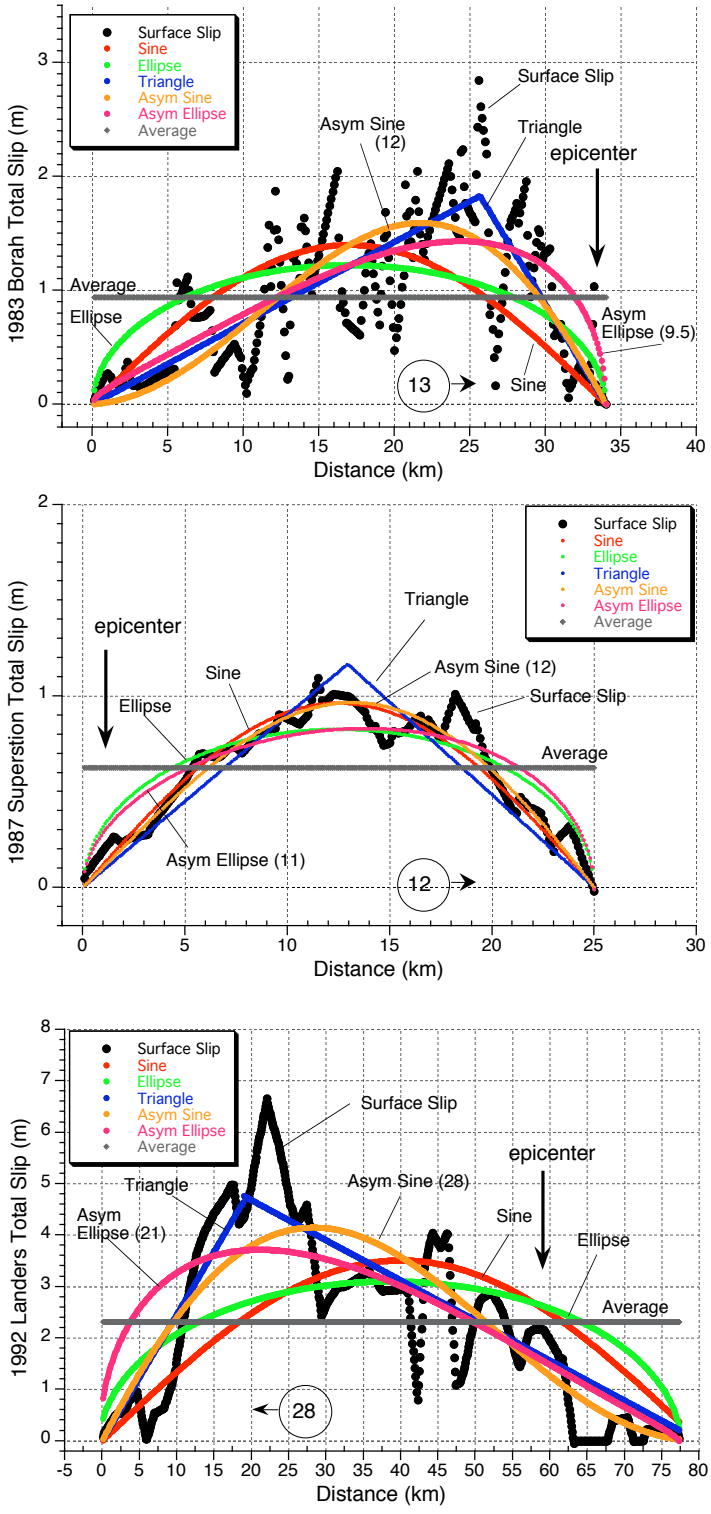

Figure 9. Examples of best-fitting regression curves to the coseismic surface slip distributions for 3 of the earthquakes listed in Table 1. The digitized surface slip and respectiive types of regression curves are labeled in each plot. Position of epicenter with respect to fault strike indicated by downward pointing arrow. Integration of the digitized values of surface slip allows definition of a point where half the cumulative slip falls on either side. That value is defined for each slip distribution (value in circle) by the distance in km to nearest fault endpoint. The distances (km) of the peak values to the nearest end of the fault rupture are given in parenthesis for the asymetric sine and asymetric ellipse curve fits. Remainder of events in Table 1 are analyzed in the same manner and compiled in Appendix 3.

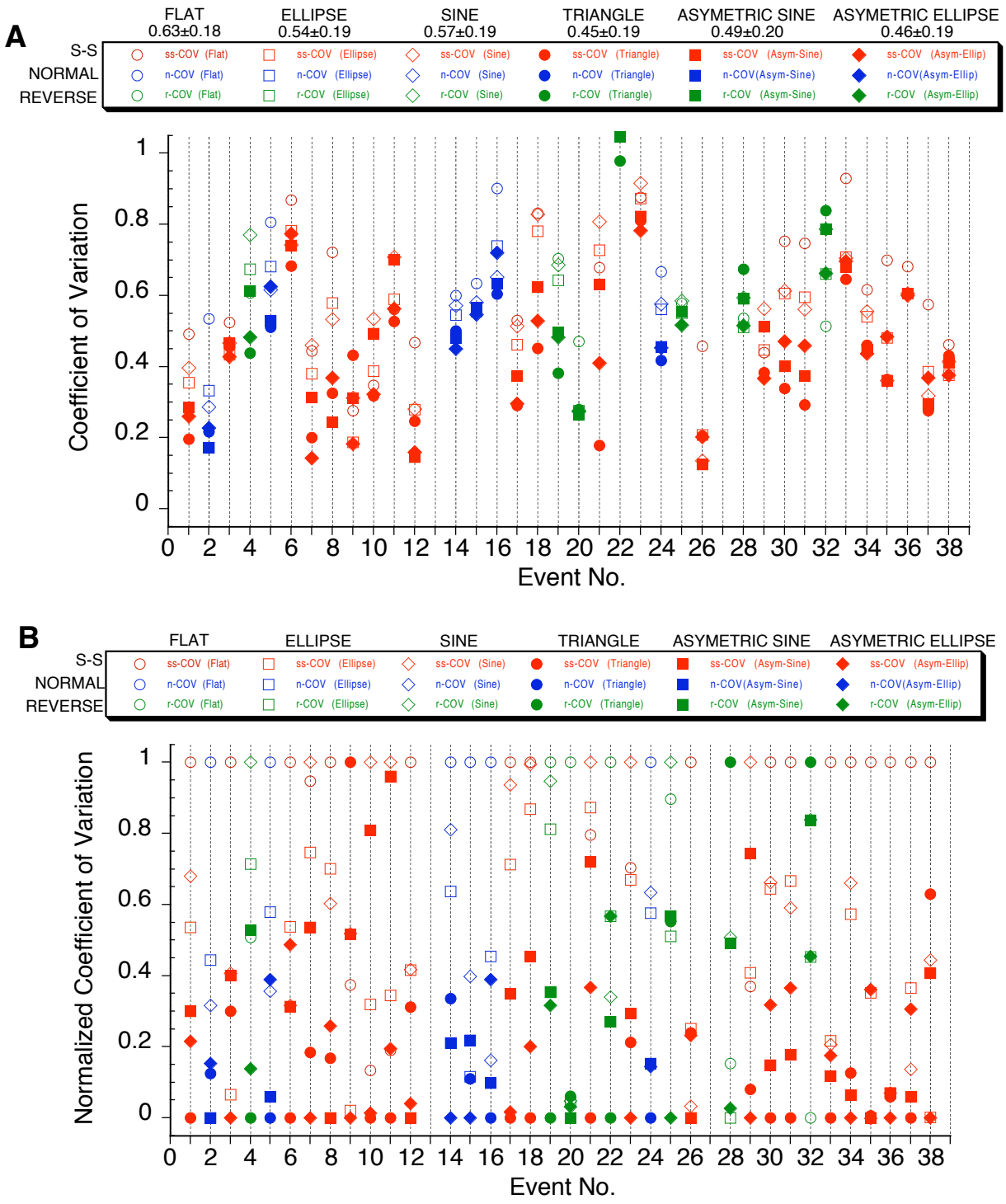

Figure 10. (A) Coefficient of Variation for various curve-fits to surface slip distributions plotted as function of the number of the respective earthquake listed in Table 1. Average values and standard deviation are listed for each type of curve fit in the plot header. (B) Coefficients of Variation are normalized between minimum and maximum values for each event to aid in visualization that asymetric curves (triangle, asymetric sine and ellipse: solid symbols) consistently provide better estimation of observed slip distributions than do a flat line or sine and ellipse curves.

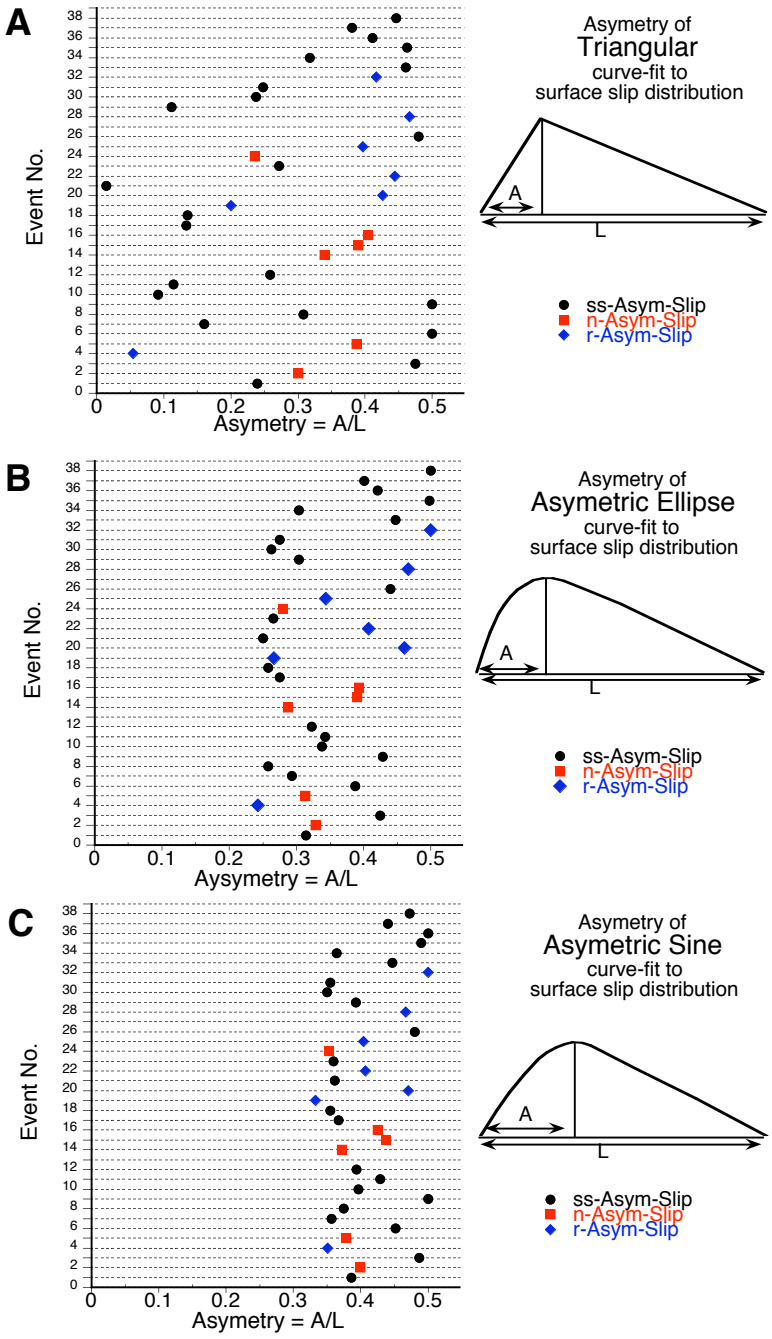

Figure 11. Asymetry of earthquake surface slip distributions for earthquakes listed in Table 1 as reflected in curve-fits to observed surface slip distributions using (A) triangular, (B) asymetric ellipse, and (C) asymetric sine functions. The asymetry function is defined as the ratio A/L where A is the shortest distance from a rupture endpoint to the peak slip and L is the respective rupture length. The function as defined is limited to between 0 and 0.5, whereby a value 0 indicates peak slip at endpoint of rupture and 0.5 value indicates peak slip at rupture midpoint. Different symbols are used for strike-slip (ss), reverse (r) and normal (n) earthquakes.

Figure 12. Relationship of epicenter location to asymetry of surface slip distributions as reflected in curve-fits to surface slip distributions using (A) triangular, (B) asymetric ellipse, (C) asymetric sine functions and (D) point along strike where contribution of slip to moment value is divided equally. The asymetry of the surface slip (solid symbols) is defined as the ratio A/L where A is the shortest distance from a rupture endpoint to the peak slip and L is the respective rupture length. The relative location of the epicenter is defined by ratio E/L where E is the distance of the epicenter from the same rupture endpoint used to define A. In this manner the ratio A/L is limited to between 0 and 0.5 and the ratio E/L is limited between 0 and 1. Strike-slip (SS), normal (n), and reverse (r) mechanisms are denoted by different symbols.

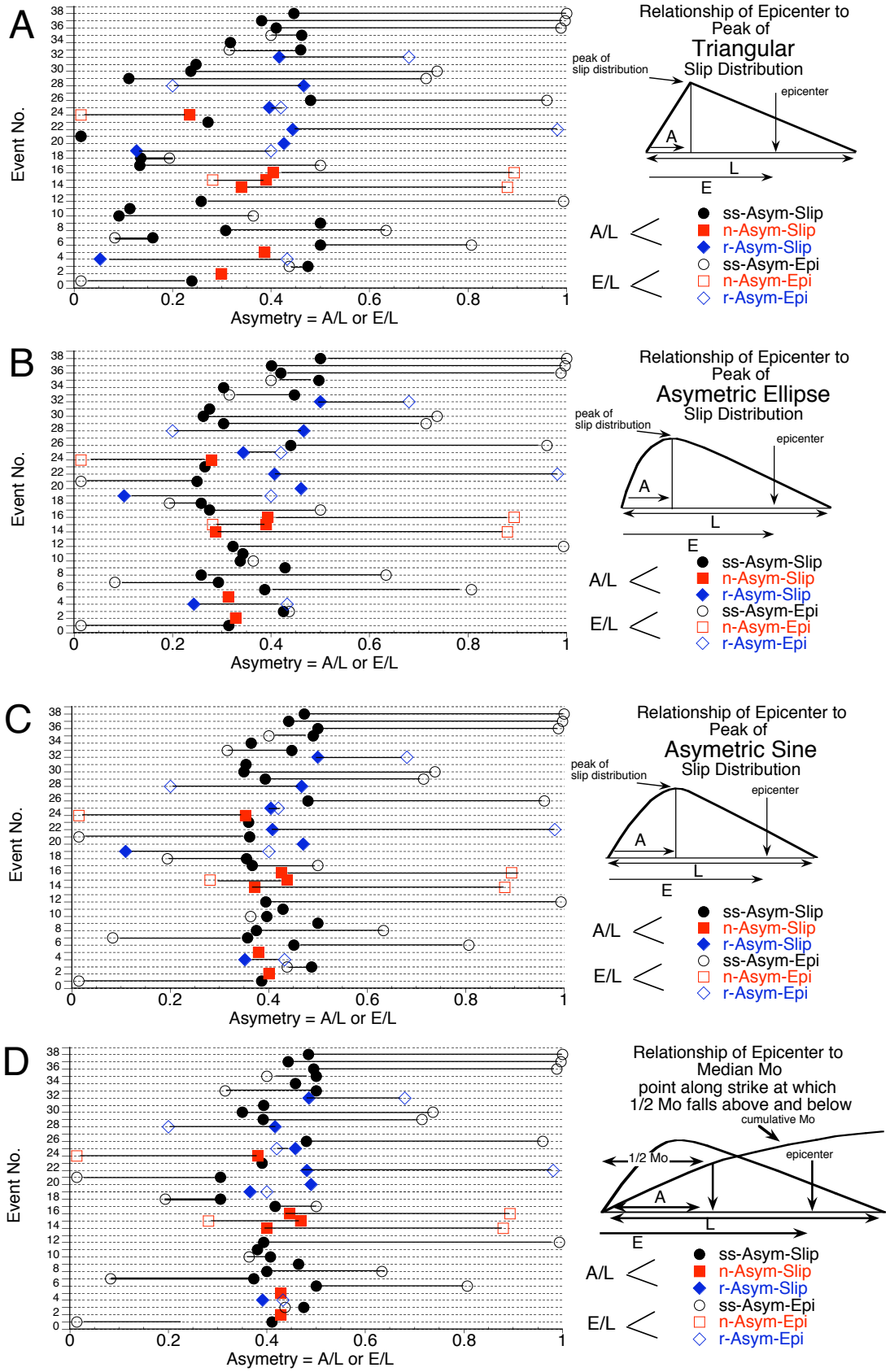
A
Event No.
Asymetry = A/L or E/L
Relationship of Epicenter to Peak of
Triangular
Slip Distribution
peak of slip distribution
epicenter
A
L
E
A/L
E/L
ss-Asym-Slip
n-Asym-Slip
r-Asym-Slip
ss-Asym-Epi
n-Asym-Epi
r-Asym-Epi
B
Relationship of Epicenter to Peak of
Asymetric Ellipse
Slip Distribution
C
Relationship of Epicenter to Peak of
Asymetric Sine
Slip Distribution
D
Relationship of Epicenter to Median Mo
point along strike at which 1/2 Mo falls above and below
cumulative Mo
1/2 Mo

Figure 12.

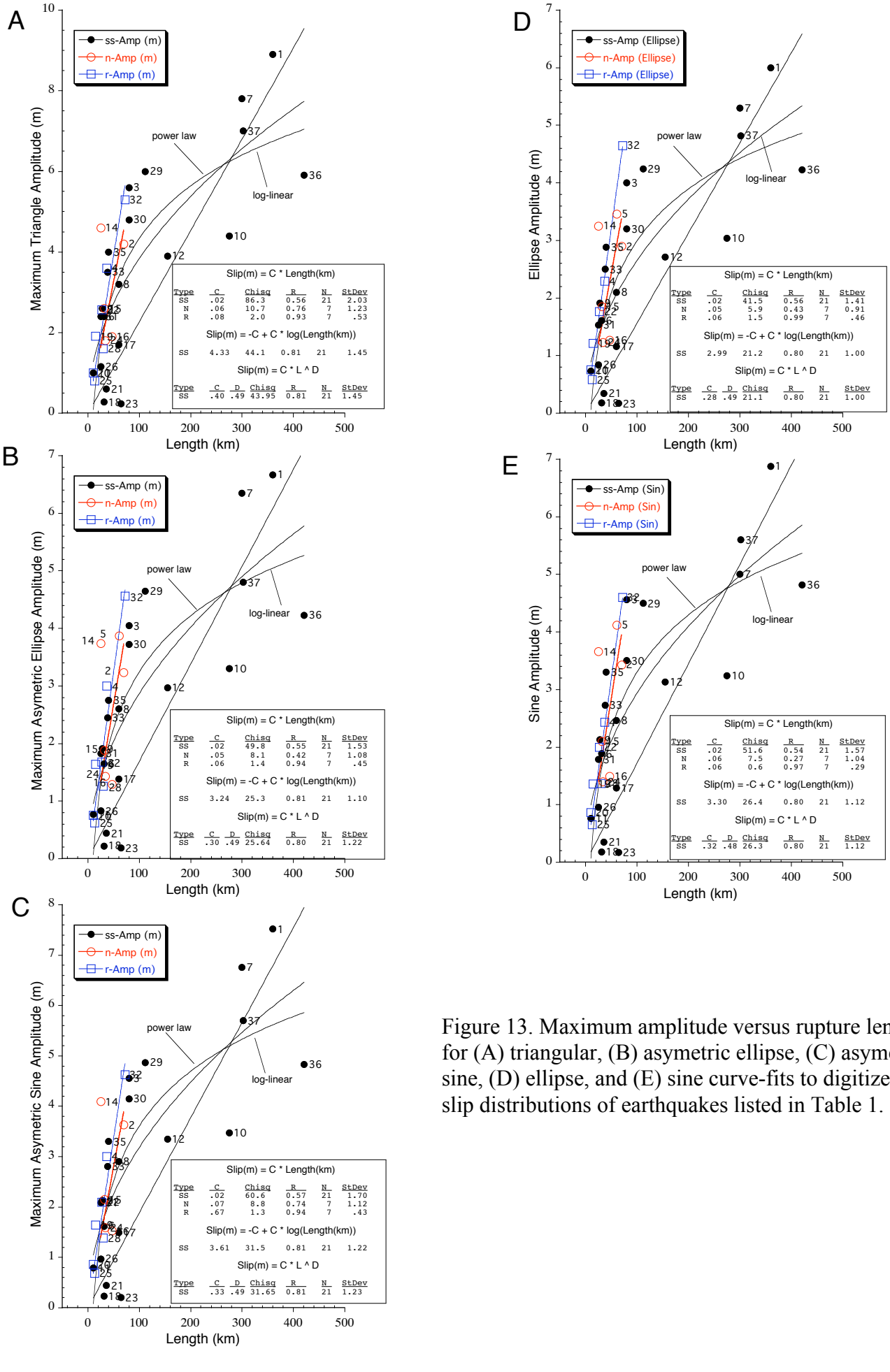

Figure 13. Maximum amplitude versus rupture length for (A) triangular, (B) asymetric ellipse, (C) asymetric sine, (D) ellipse, and (E) sine curve-fits to digitized slip distributions of earthquakes listed in Table 1.

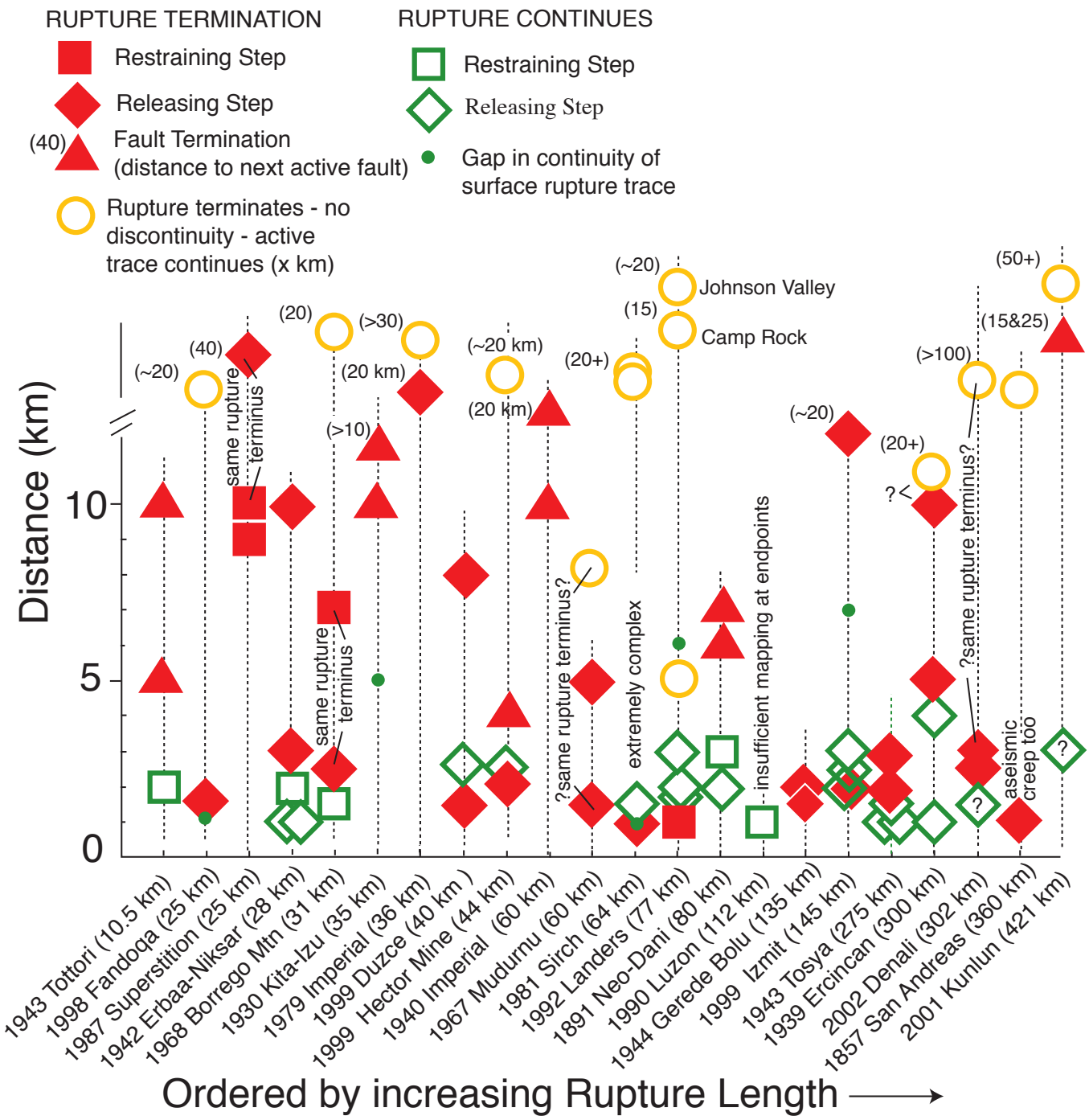

Figure 14. Synopsis of observations bearing on relationship of geometrical discontinuities along fault strike to the endpoints of historical earthquake ruptures. Earthquake date, name and rupture length listed on horizontal axis. The earthquakes are ordered by increasing rupture length (but not scaled to distance along axis). Above the label of each earthquake is a vertical line and symbols along line represent dimension of discontinuities within and at endpoints of each rupture.

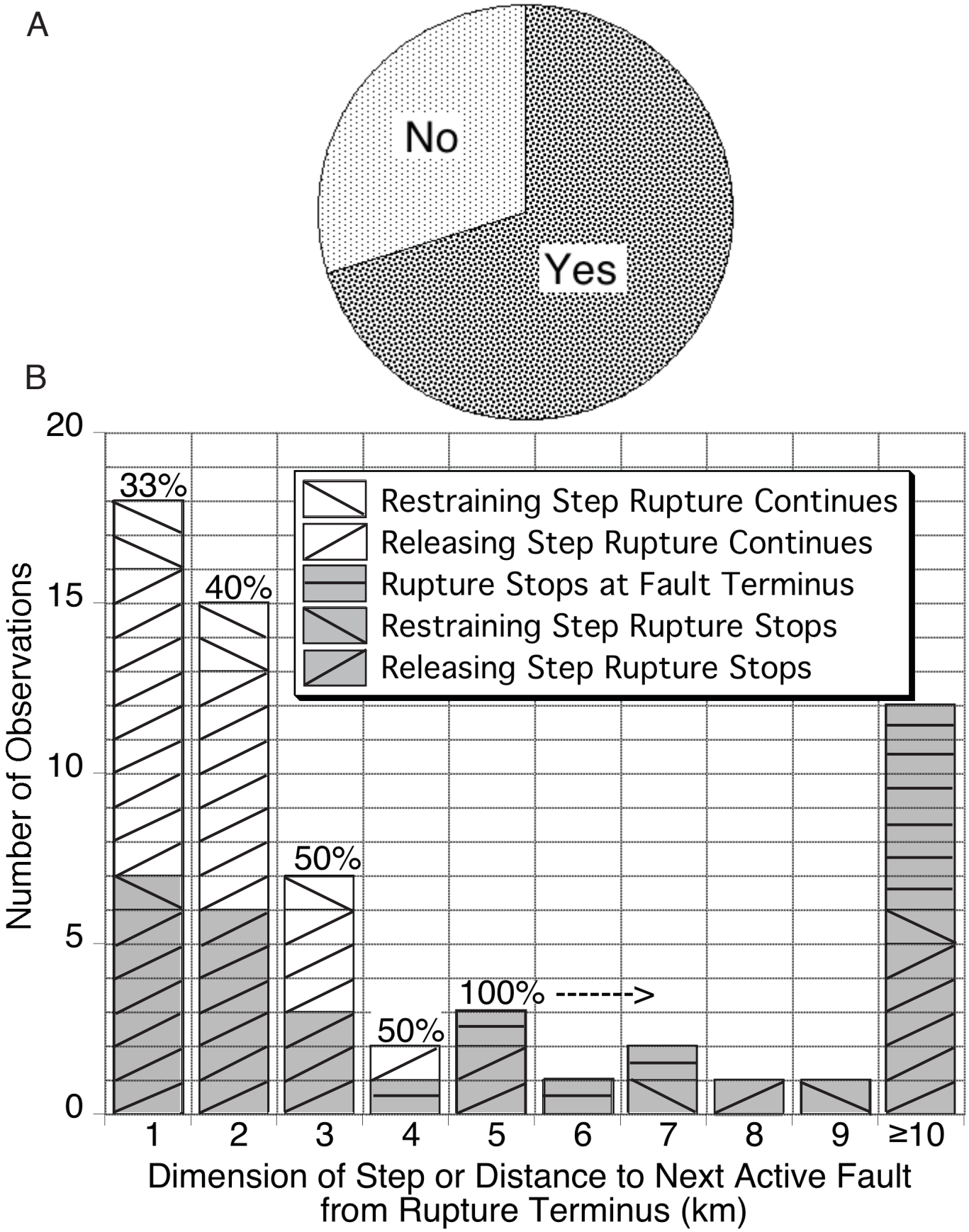

Figure 15. Relation of fault trace complexity to rupture length for strike-slip faults. (A) Pie chart of total number of rupture endpoints divided between whether (yes) or not (no) endpoints are associated with a geometrical discontinuity (step or termination of rupture trace). About 75% of time rupture endpoints are associated with such discontinuities. The remainder appear to simply die out along an active fault trace. Sample Size is 46. (B) Histogram of the total number of geometrical discontinuities located along historical ruptures binned as a function of size (≥1, ≥2, etc) and shaded according to whether the particular step occurred at the endpoint of rupture or was broken through by the rupture. A transition occurs at 3-4 km above which no events have ruptured through and below which earthquakes have ruptured through in ~40% of the cases.

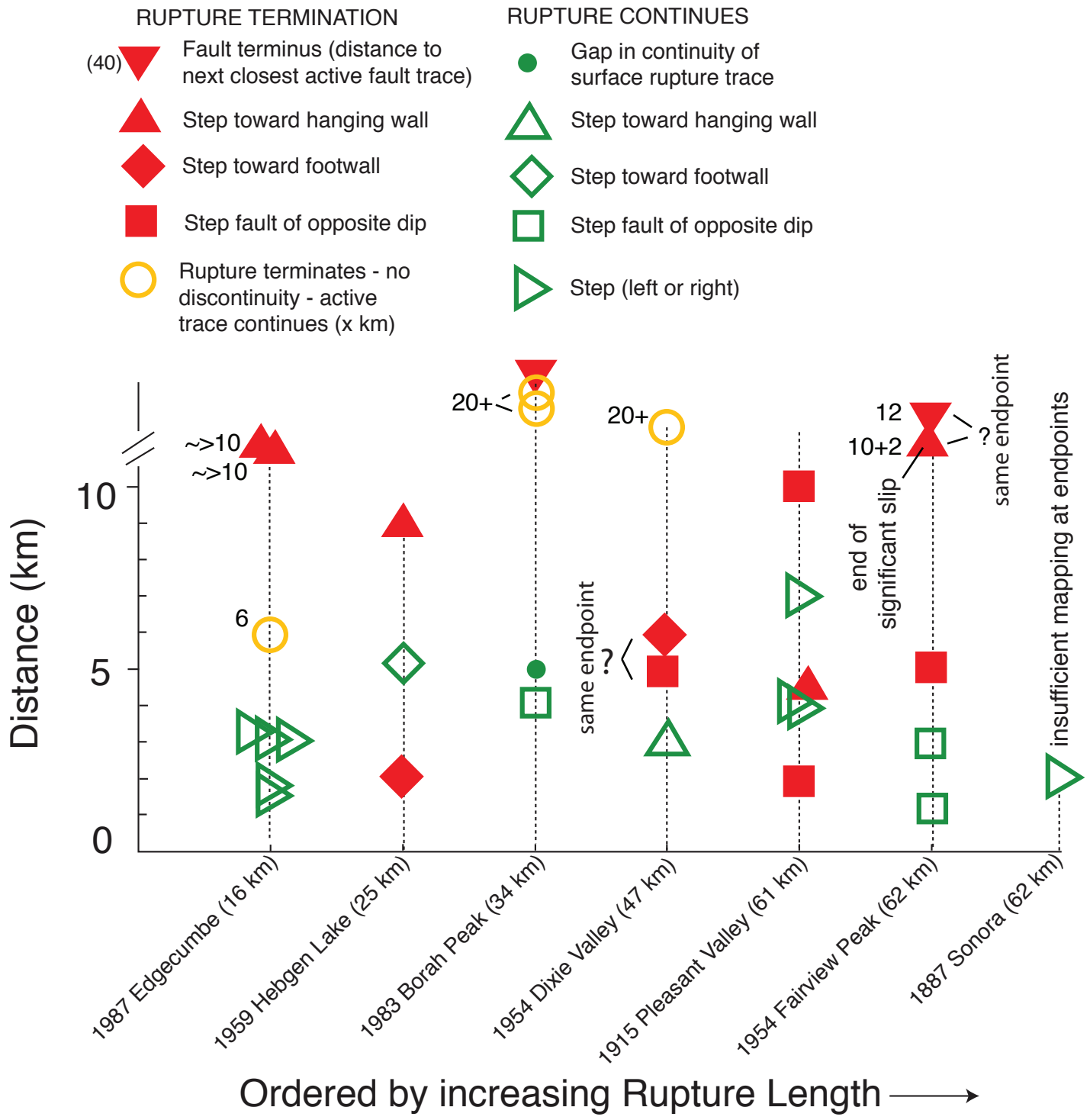

Figure 16. Synopsis of observations bearing on relationship of geometrical discontinuities along fault strike to the endpoints of normal mechanism historical earthquake ruptures. See Figure 14 for further explanation.

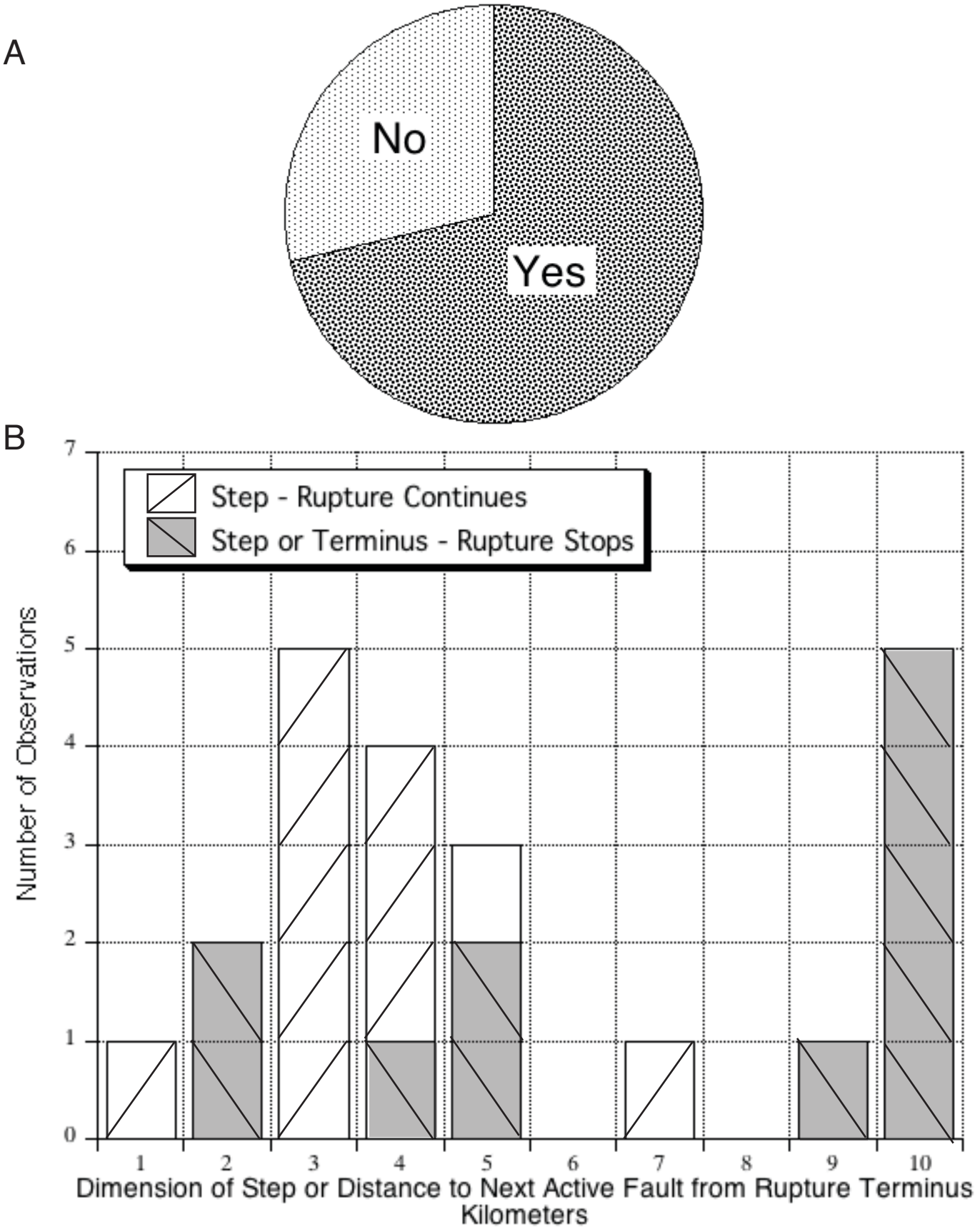

Figure 17. Relation of fault trace complexity to rupture length for normal faults. See Figure 15 for explanation. (A) About 75% of time rupture endpoints are associated with such discontinuities. The remainder appear to simply die out along an active fault trace. Sample size is 14. (B) Normal fault ruptures cross steps in fault strike as large as 5 to 7 km., larger than observed for strike-slip earthquakes.

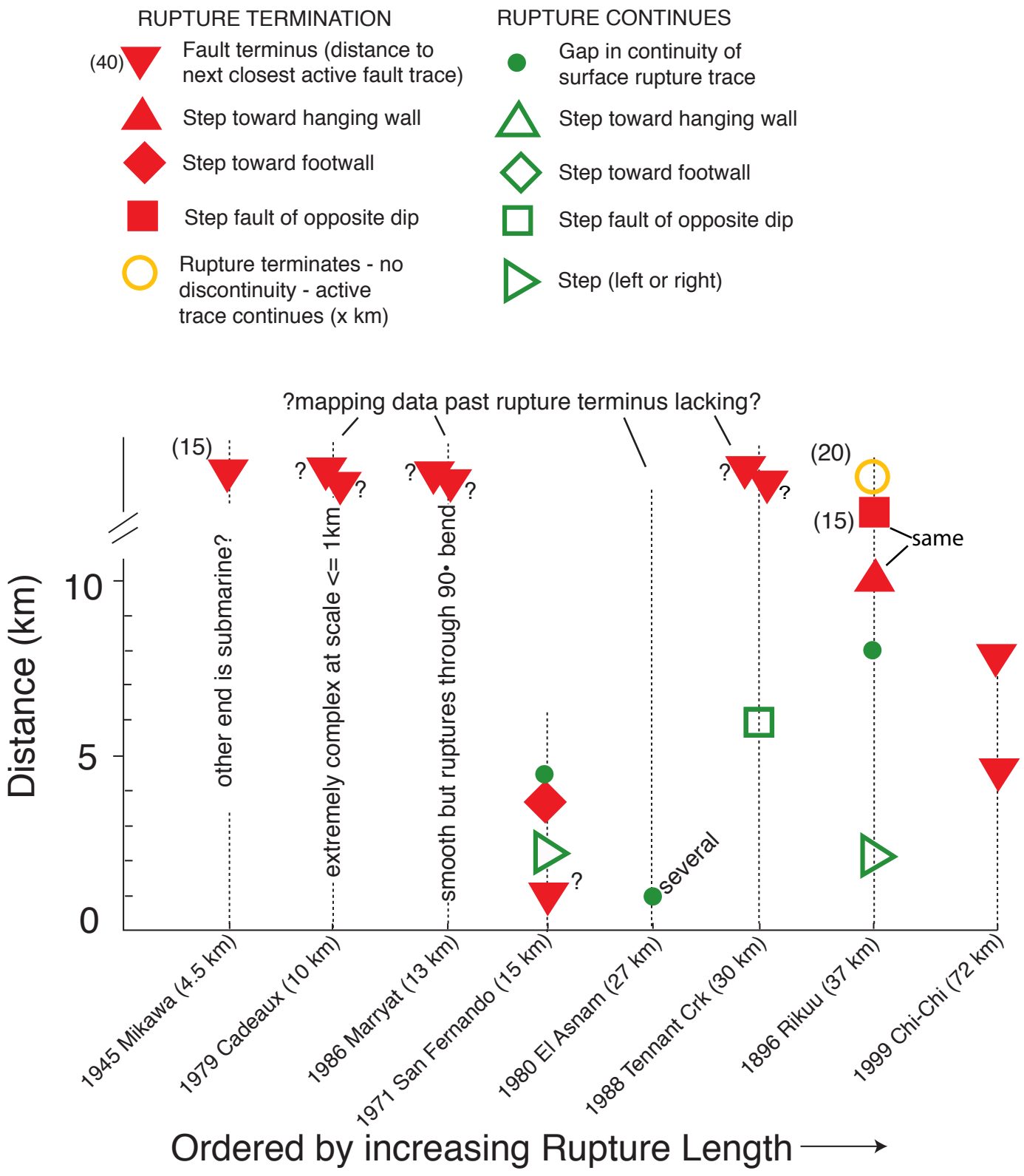

Figure 18. Synopsis of observations bearing on relationship of geometrical discontinuities along fault strike to the endpoints of thrust mechanism historical earthquake ruptures. Earthquake date, name and rupture length listed on horizontal axis. The earthquakes are ordered by increasing rupture length (but not scaled to distance along axis). Above the label of each earthquake is a vertical line and symbols along line represent dimension and type of discontinuities within and at endpoints of each rupture.

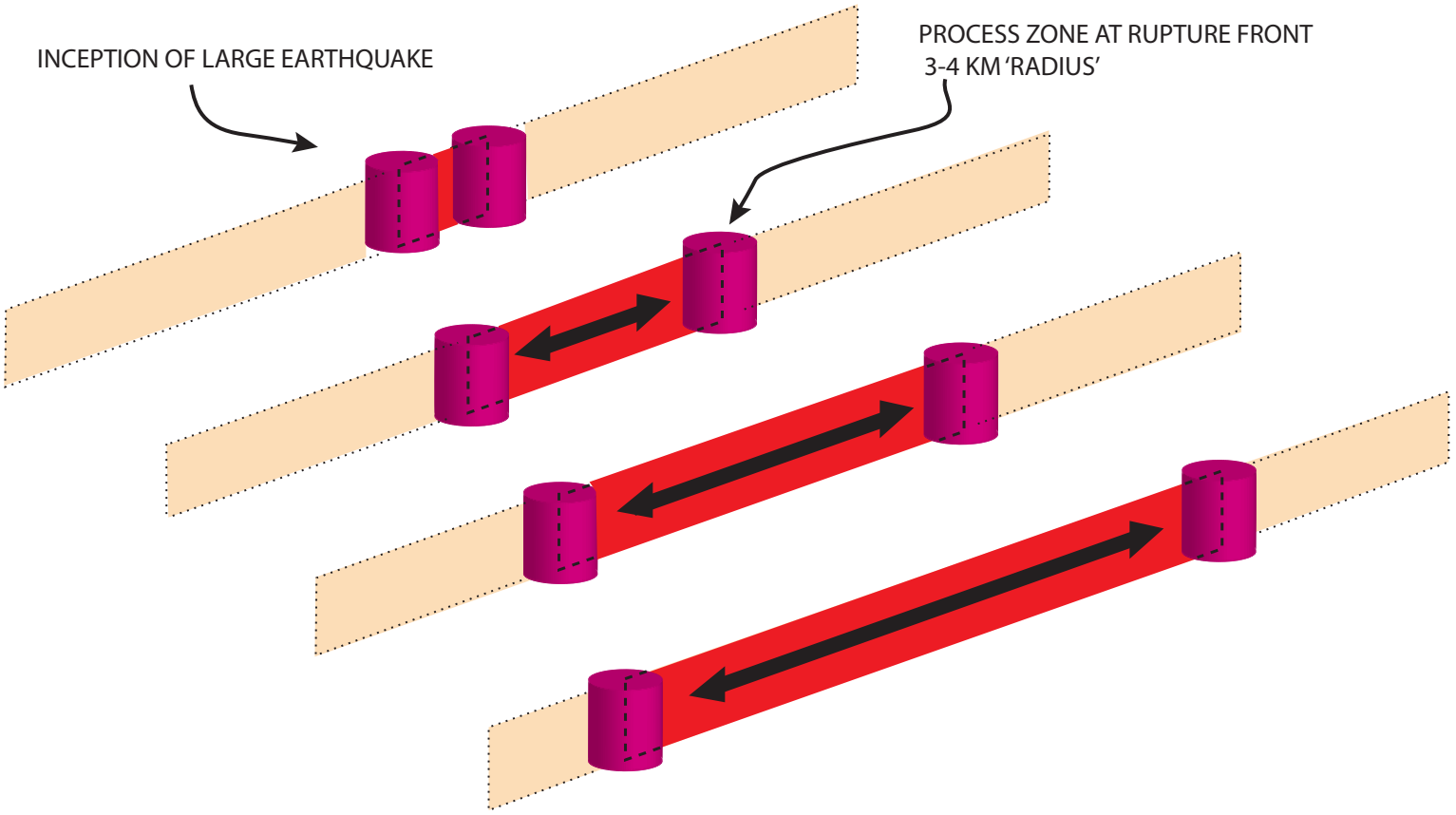

Figure 19. Empirical observations of the interplay of fault trace complexity and rupture propagation for large strike-slip earthquakes suggests a process whereby the magnitude of stress changes and volume affected by those stress changes at the front of a propagating rupture are largely the same and largely invariable during the rupture process, regardless of the distance a rupture has or will propagage.

Compilation of Maps and Earthquake Slip Distributions for Earthquakes Listed in Table 1
See Figures 1a and 1b of Manuscript for Explanation

Appendix 1

of

Displacement and Geometrical Characteristics of Earthquake Surface Ruptures: Issues and Implications for Seismic Hazard Analysis and Process of Earthquake Rupture.

Steven G. Wesnousky
Center for Neotectonic Studies
Mail Stop 169
University of Nevada, Reno
Reno, Nevada 89557
stevew@seismo.unr.edu

Jan 9 1857 Ft. Tejon, California

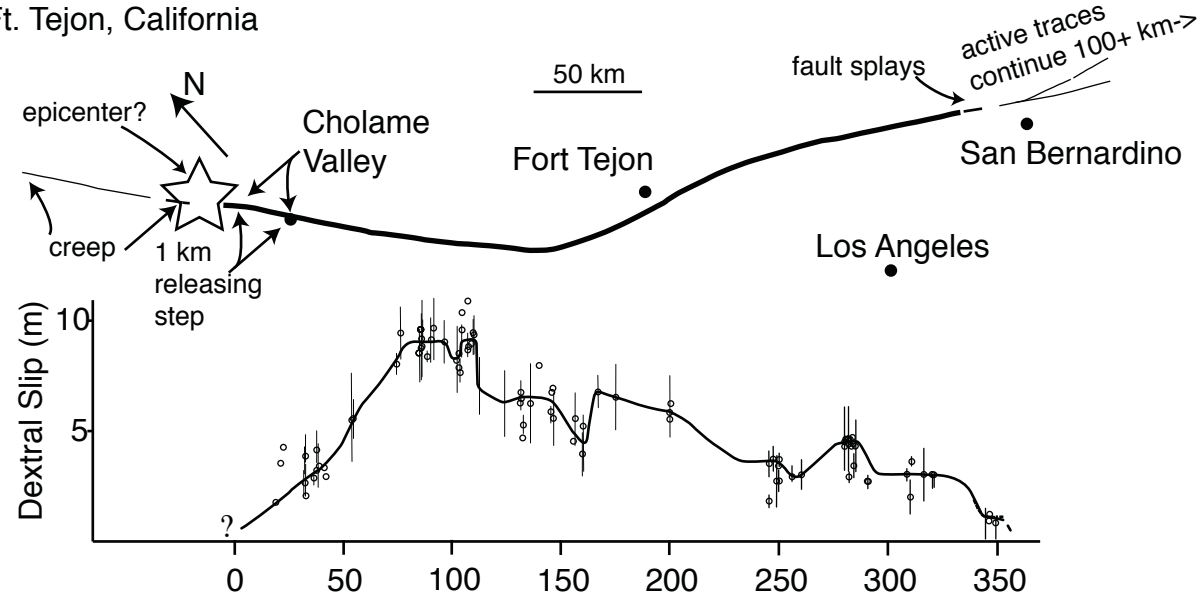

May 3 1887 Sonora, Mexico

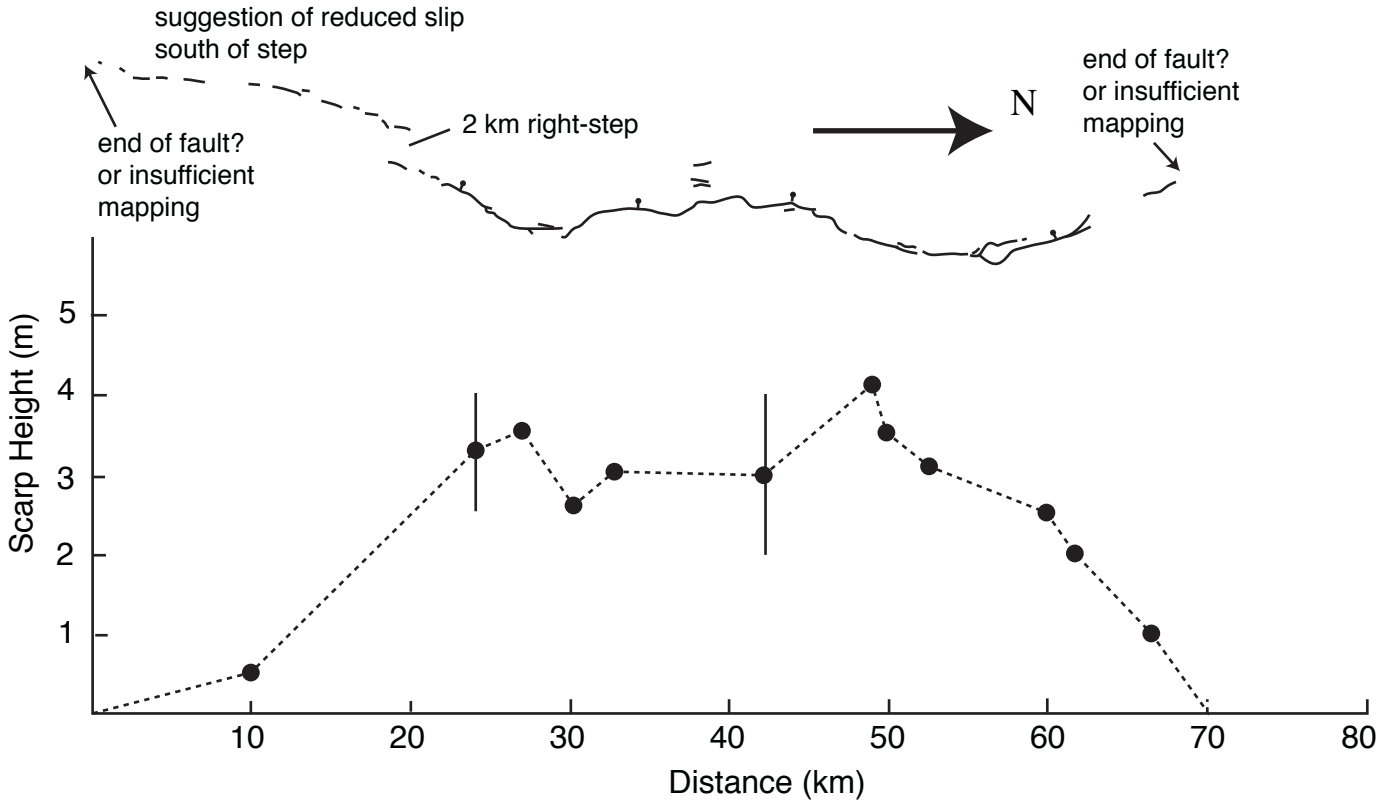

1891 Oct 28 Neo-Dani, Japan

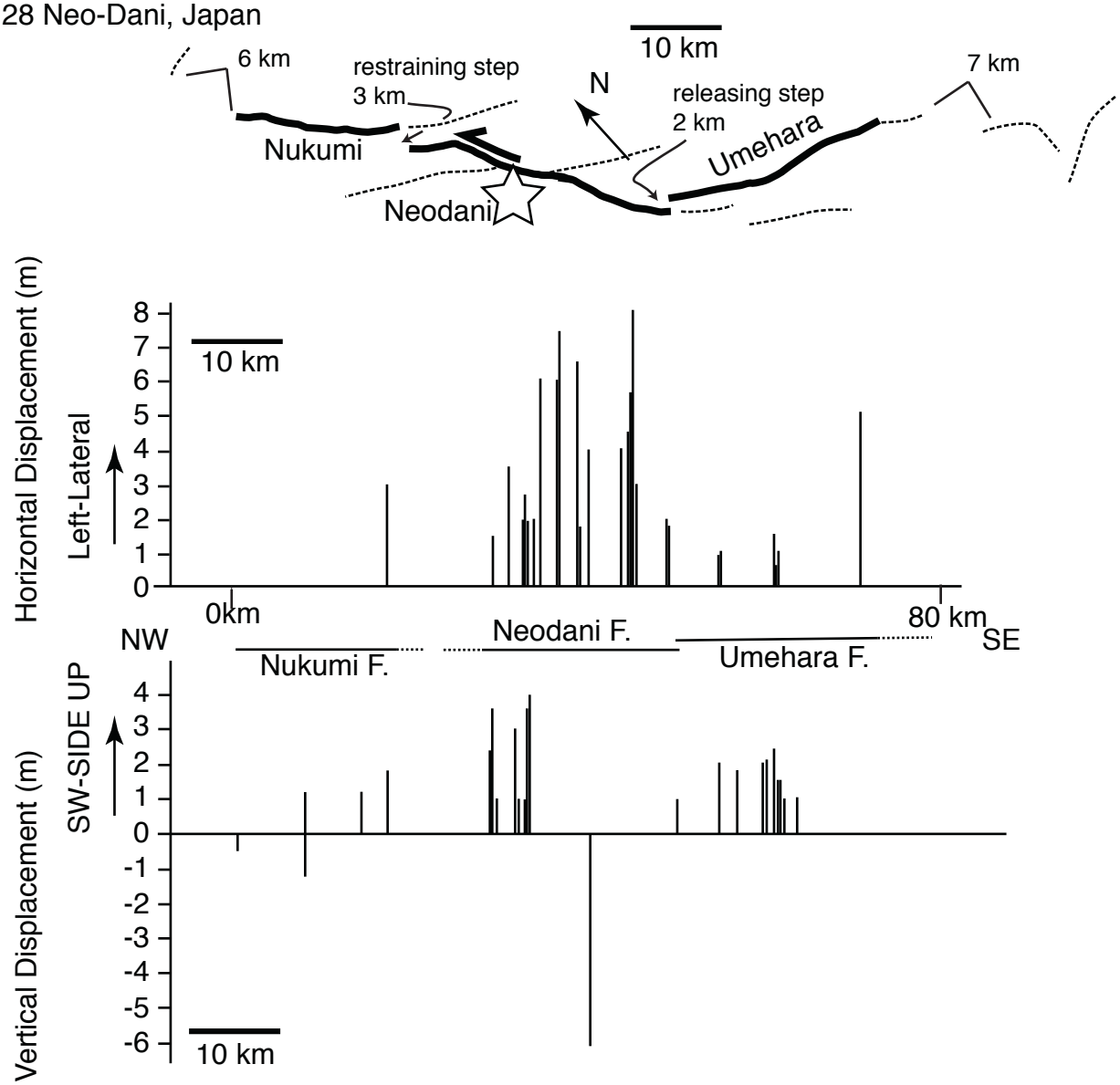

Aug 31 1896 Rikuu, Japan

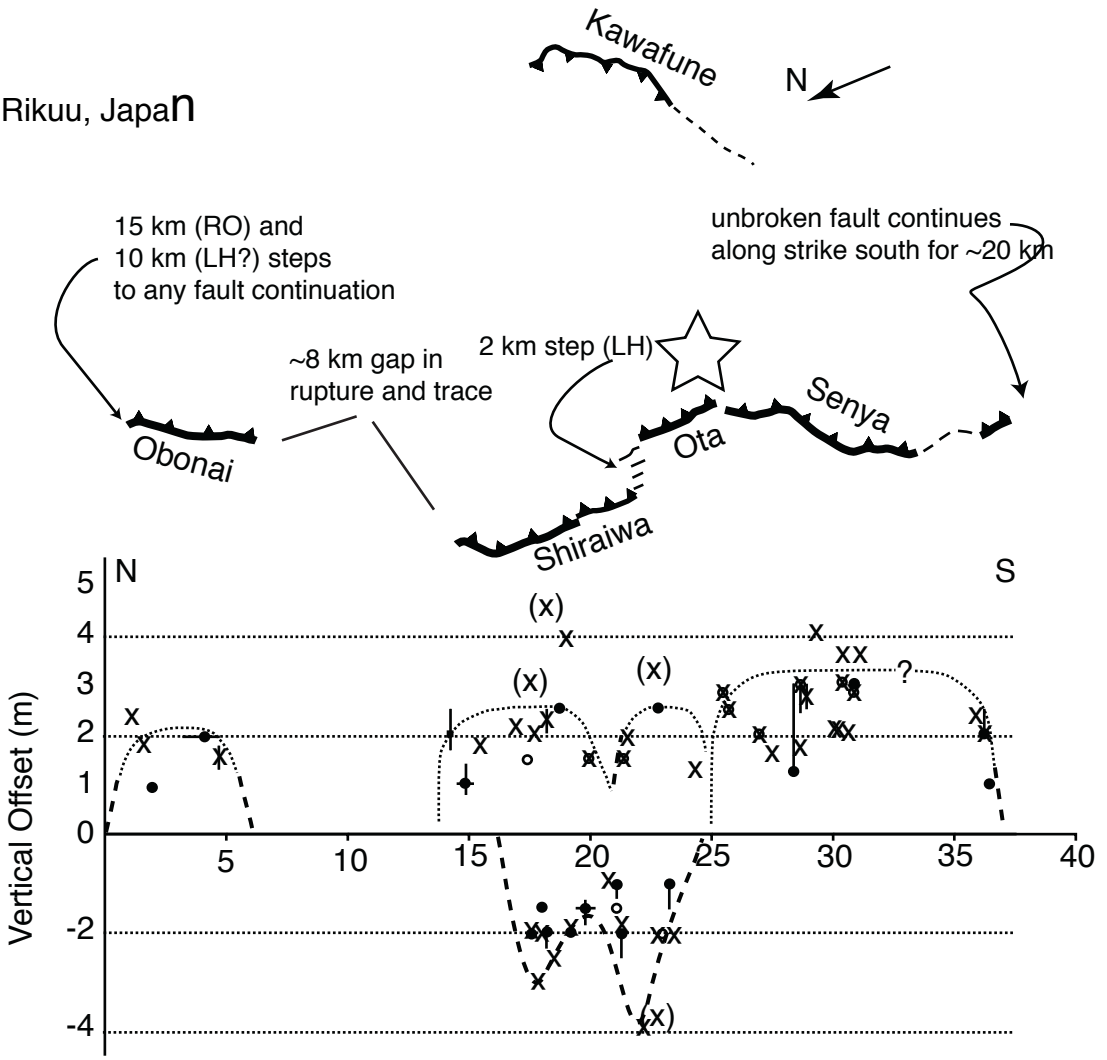

Oct 2 1915 Pleasant Valley, Nevada

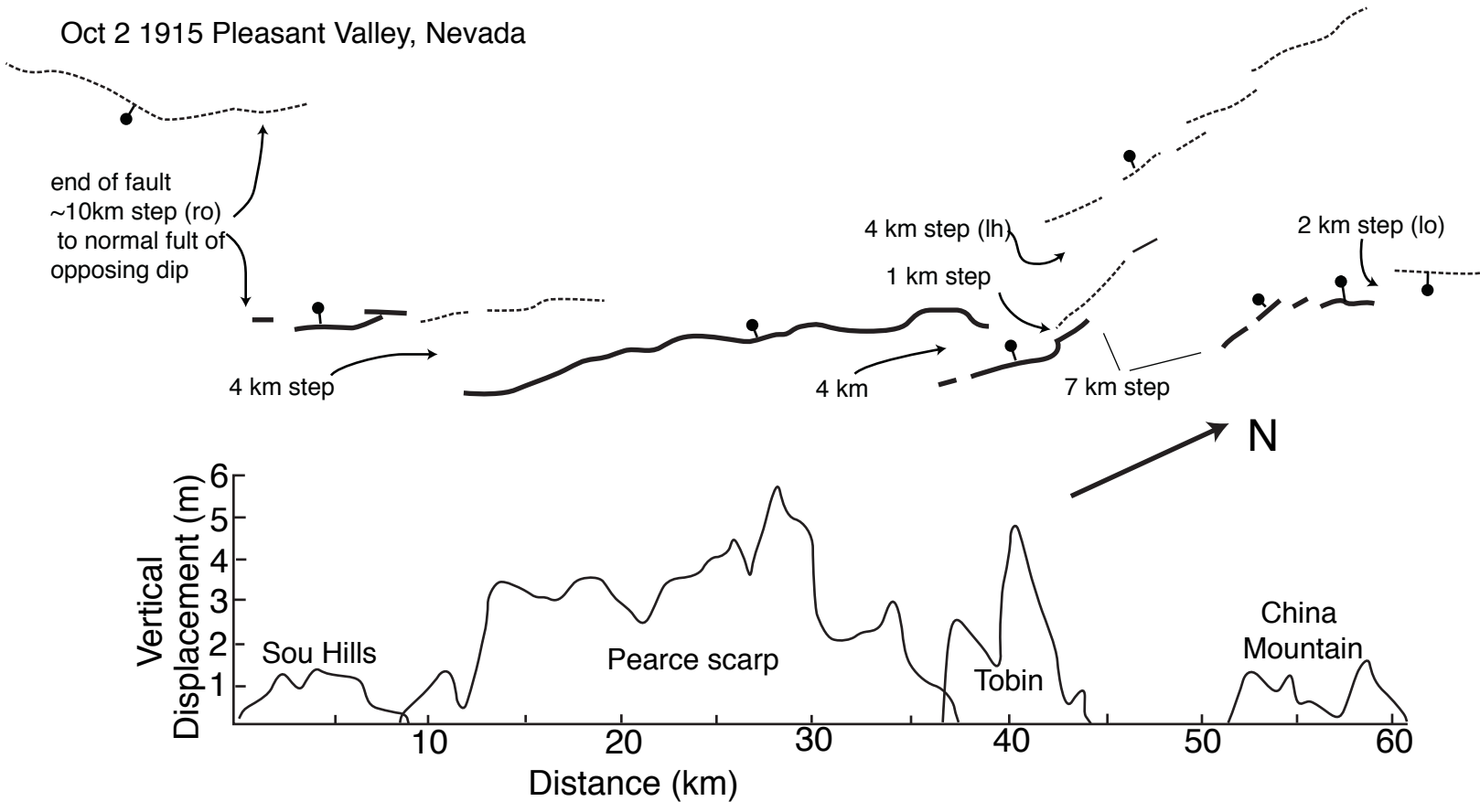

Nov 2 1930 Kita-Izu, Japan

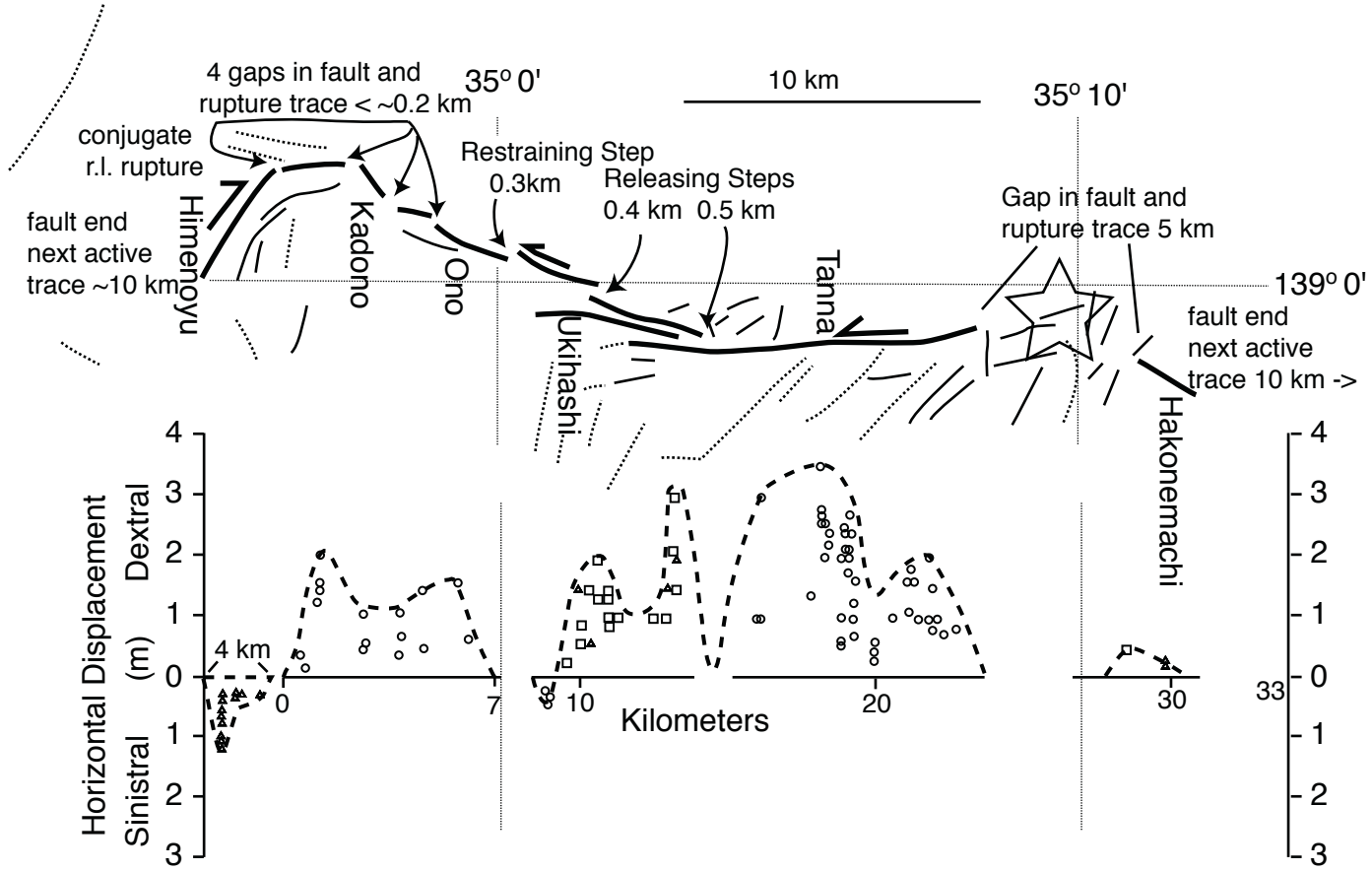

Dec 25 1939 Ercincan, Turkey

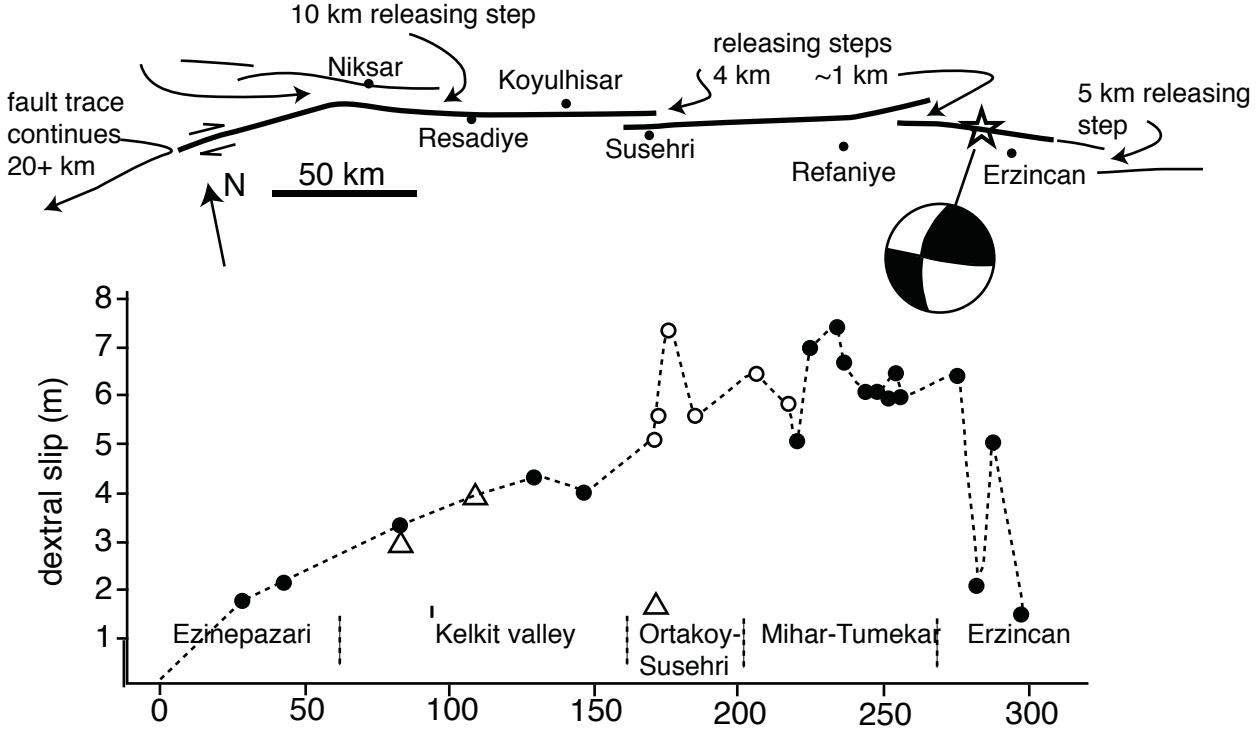

May 19 1940 Imperial, California

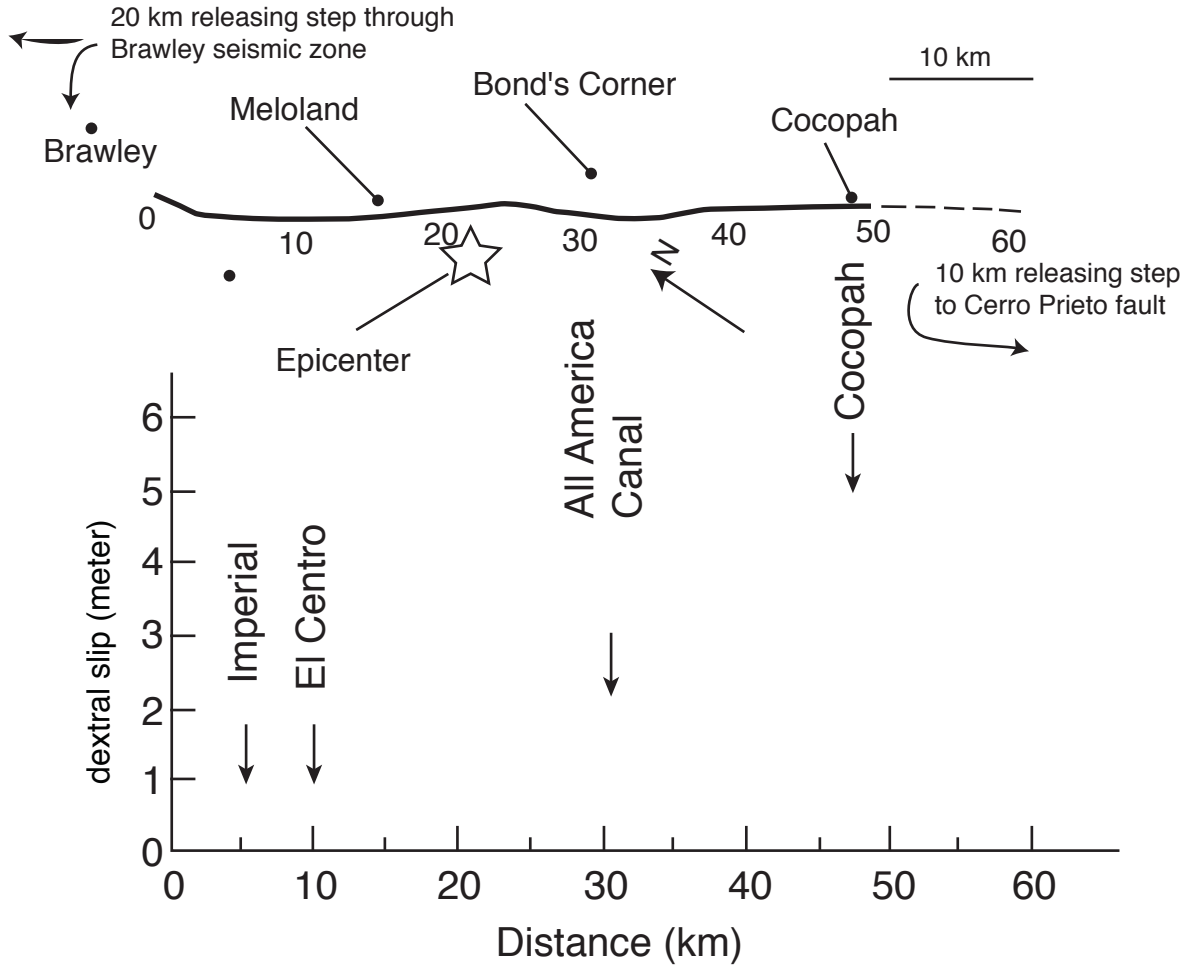

Dec 20 1942 Erbaa-Niksar, Turkey

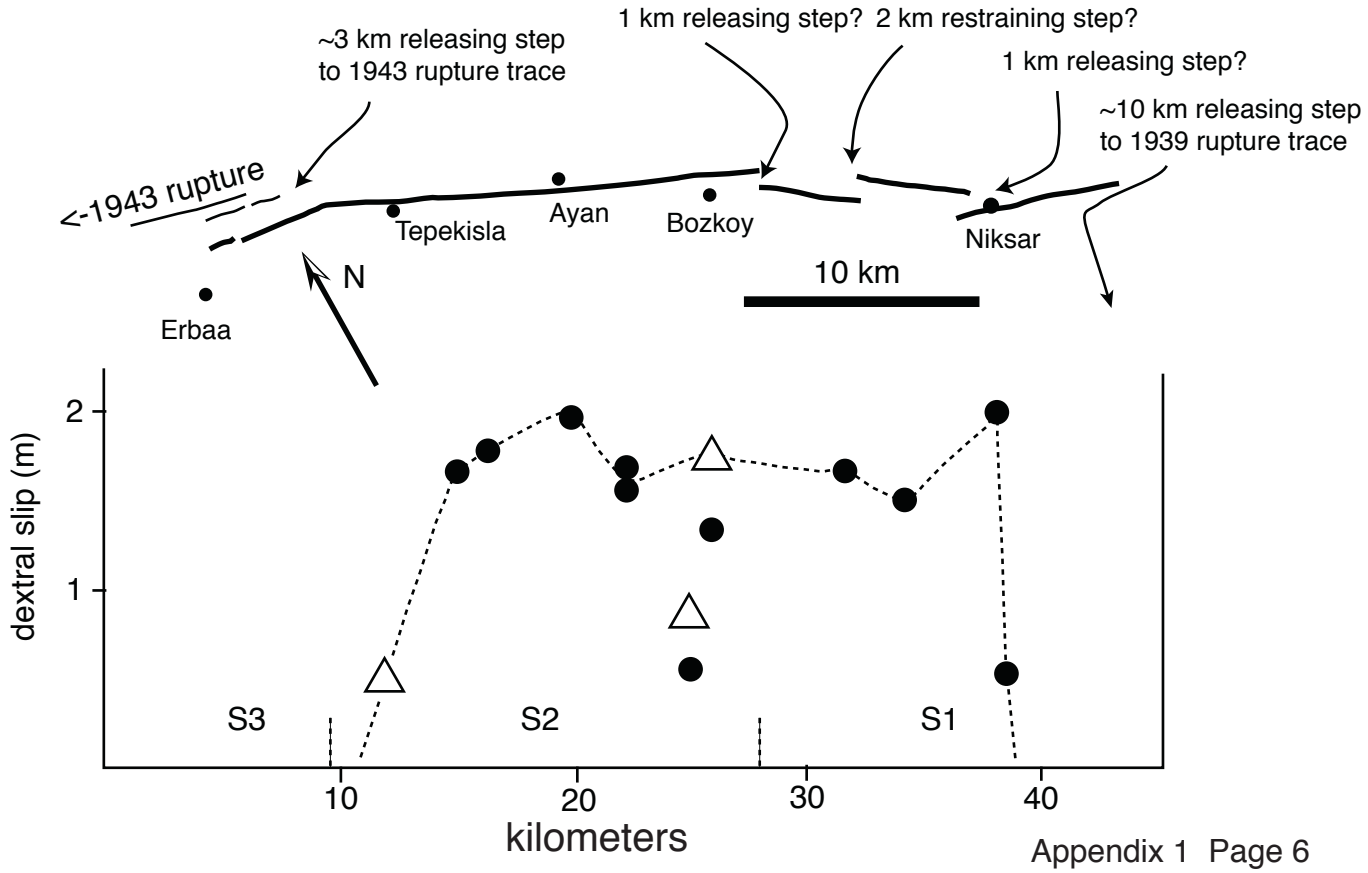

Nov 26 1943 Tosya, Turkey

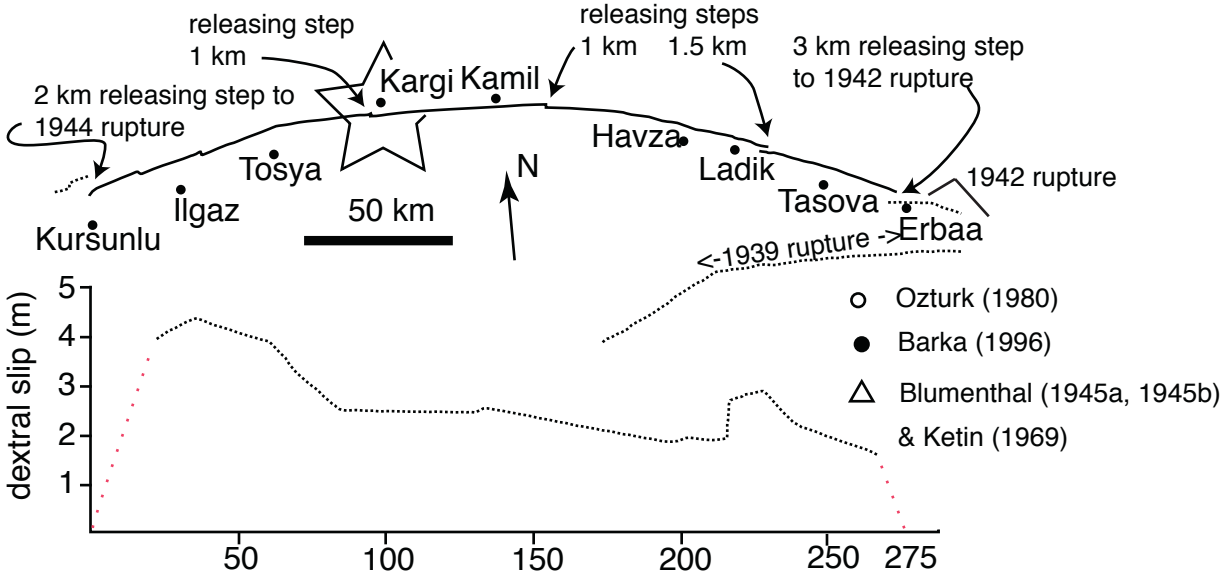

Sept 10 1943 Tottori, Japan

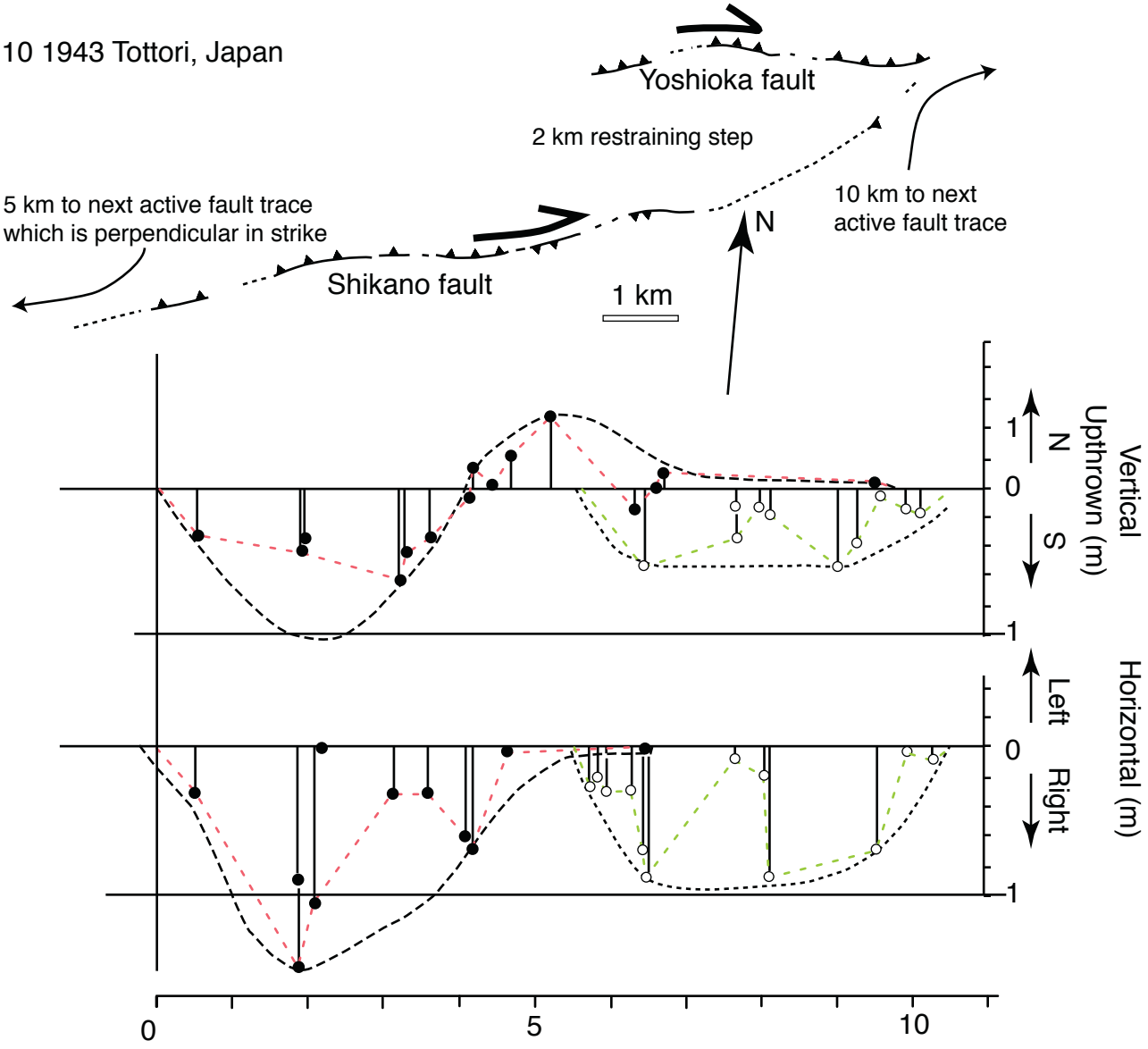

Feb 01 1944 Gerede-Bolu, Turkey

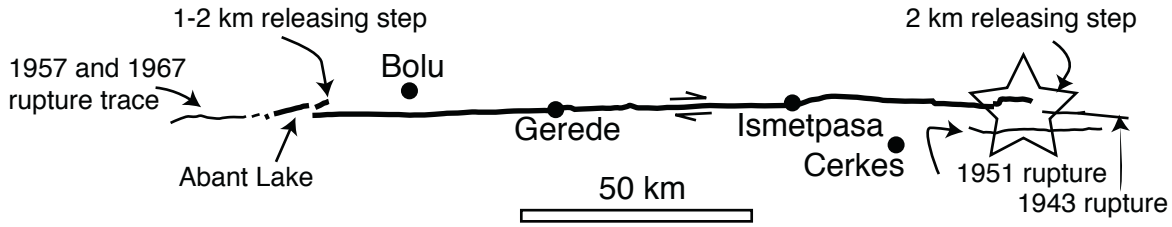

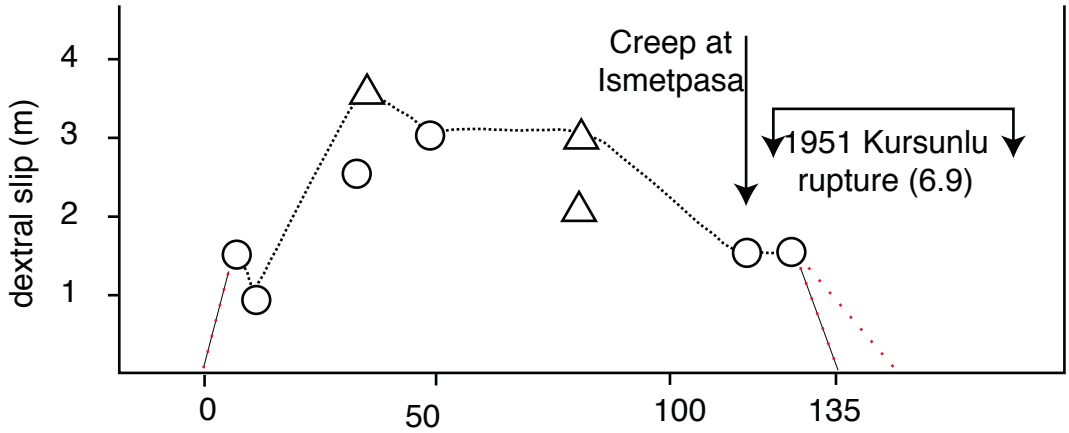

Jan 31 1945 Mikawa, Japan

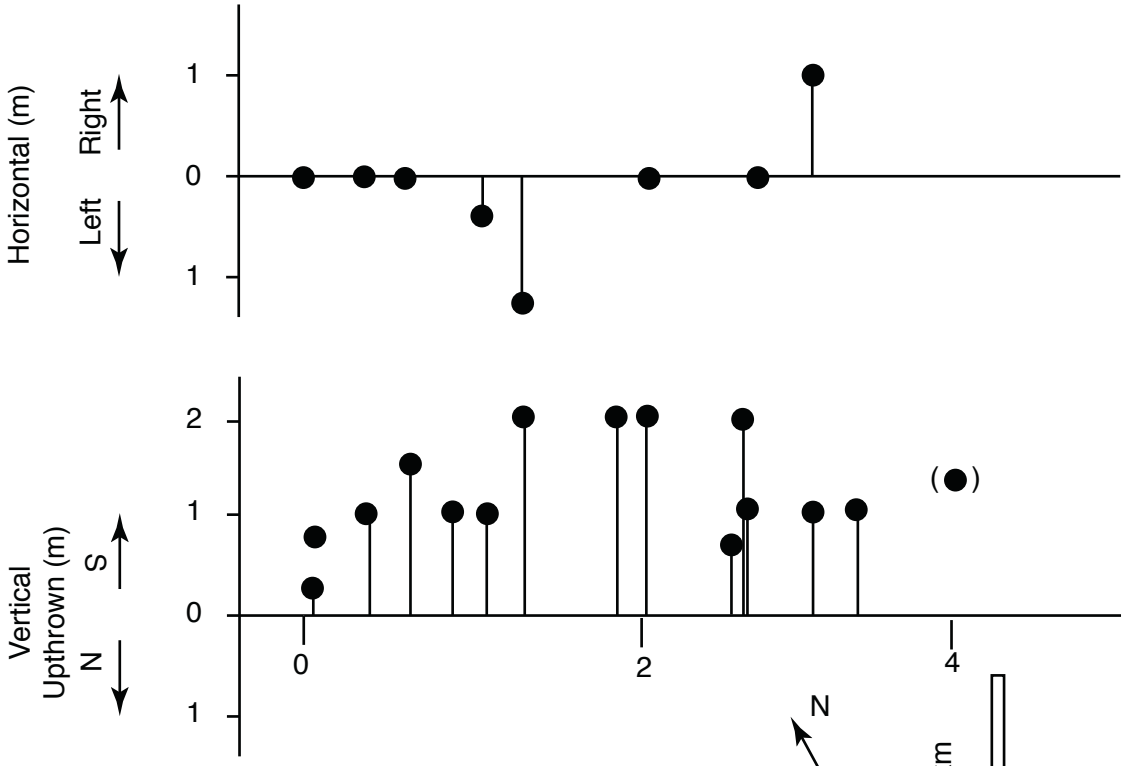

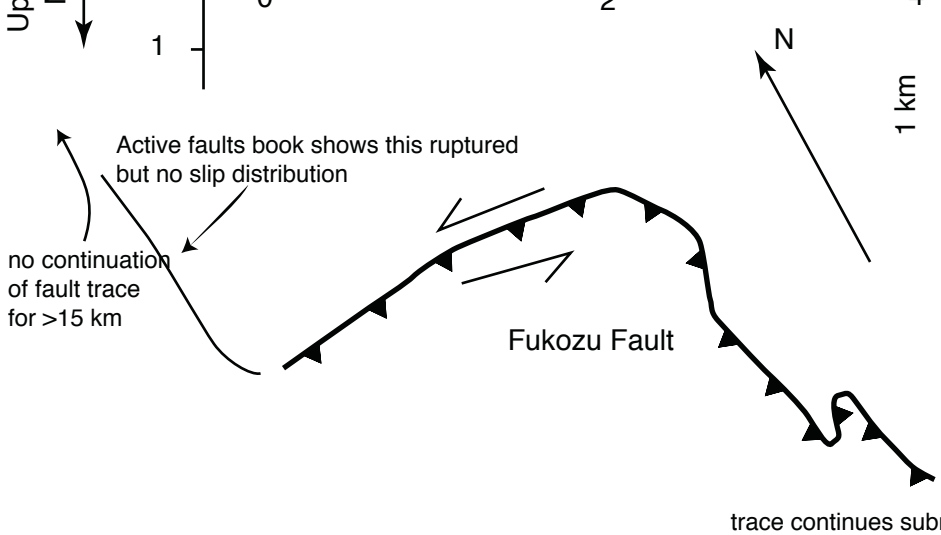

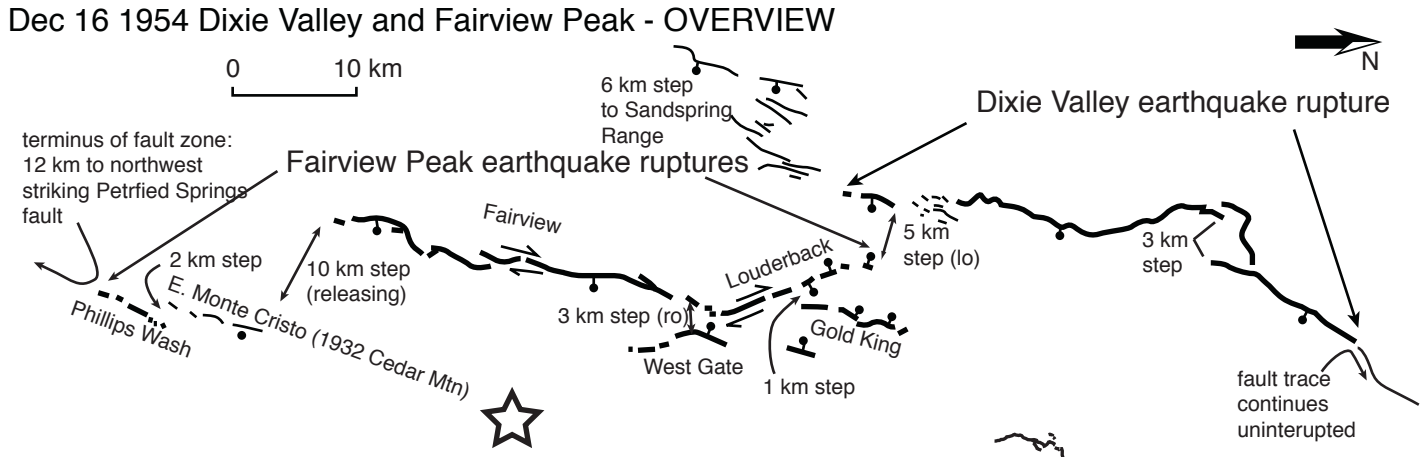
Dec 16 1954 Dixie Valley and Fairview Peak - OVERVIEW
0
10 km
N
6 km step
to Sandspring
Range
Dixie Valley earthquake rupture
terminus of fault zone:
12 km to northwest
striking Petrfied Springs
fault
Fairview Peak earthquake ruptures
Fairview
2 km step
E. Monte Cristo (1932 Cedar Mtn)
10 km step
(releasing)
Phillips Wash
3 km step (ro)
Louderback
5 km
step (lo)
3 km
step
Gold King
West Gate
1 km step
fault trace
continues
uninterupted

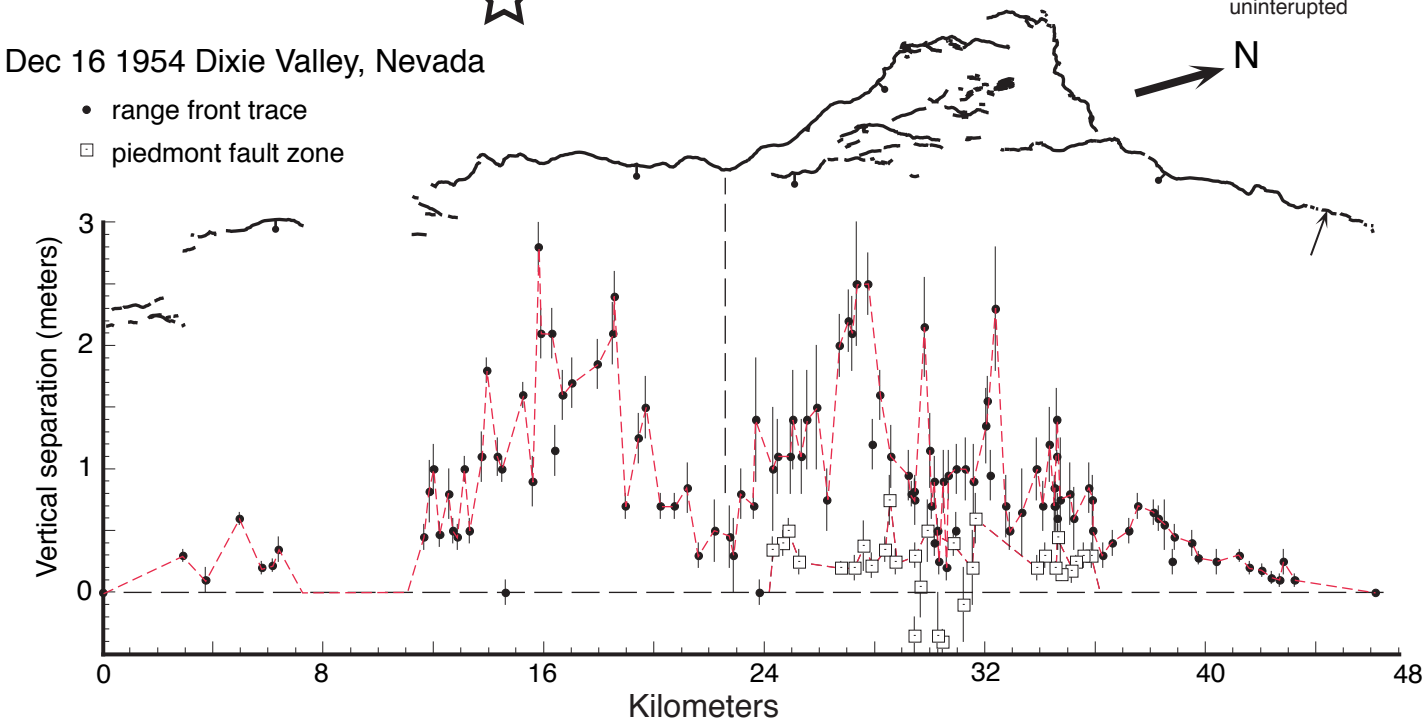
Dec 16 1954 Dixie Valley, Nevada
range front trace
piedmont fault zone
N
Vertical separation (meters)
0
1
2
3
0
8
16
24
32
40
48
Kilometers

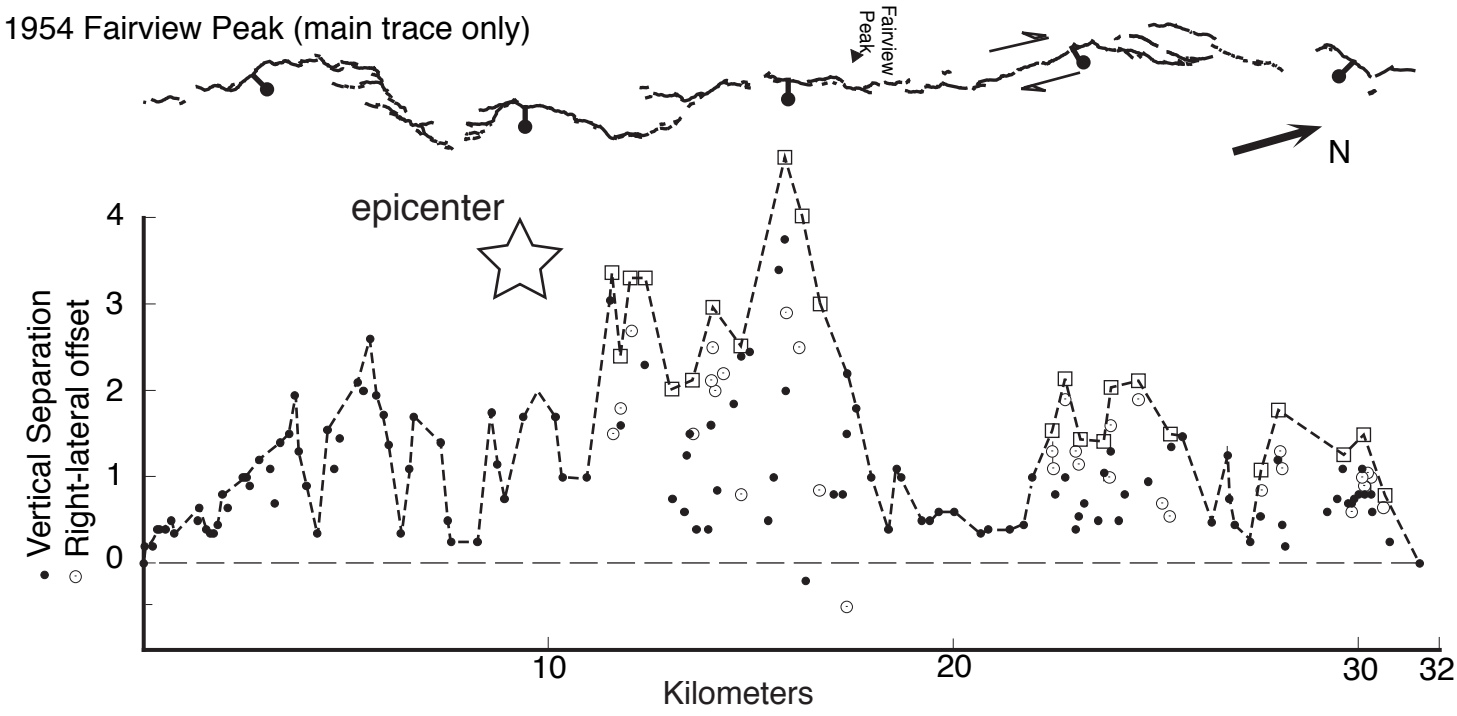
1954 Fairview Peak (main trace only)
Fairview
Peak
N
epicenter
Vertical Separation
Right-lateral offset
0
1
2
3
4
10
20
30
32
Kilometers

Aug 17 1959 Hebgen Lake, Montana

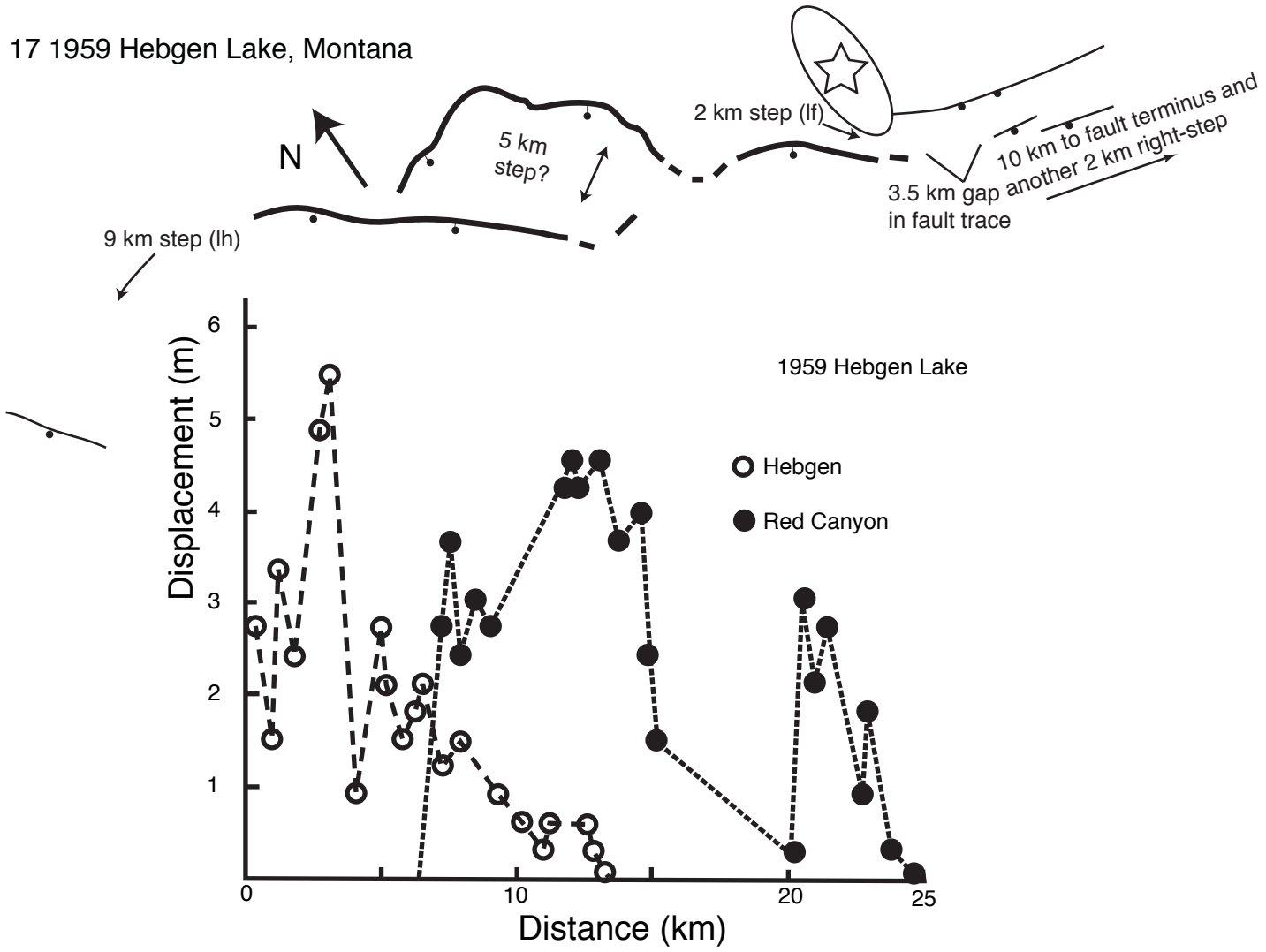

July 22 1967 Mudurnu Valley, Turkey

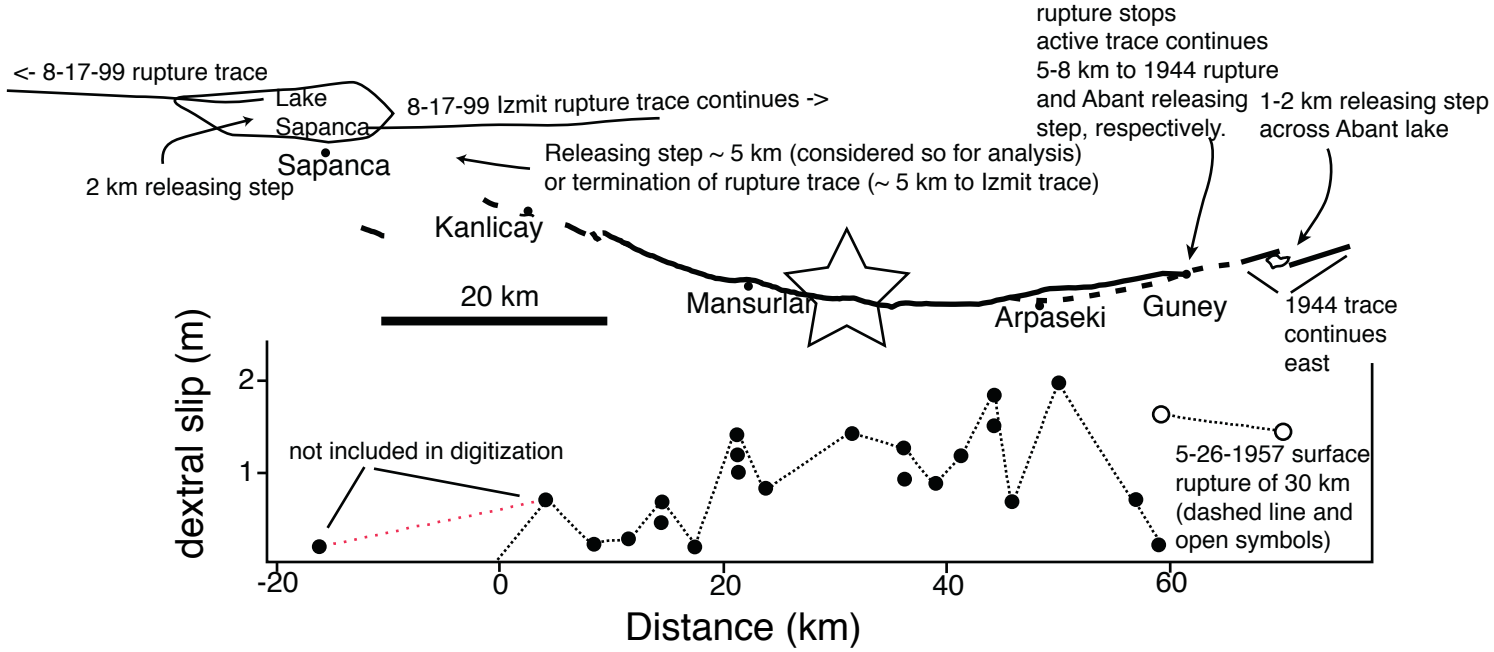

Apr 09 1968 Borrego Mountain, California

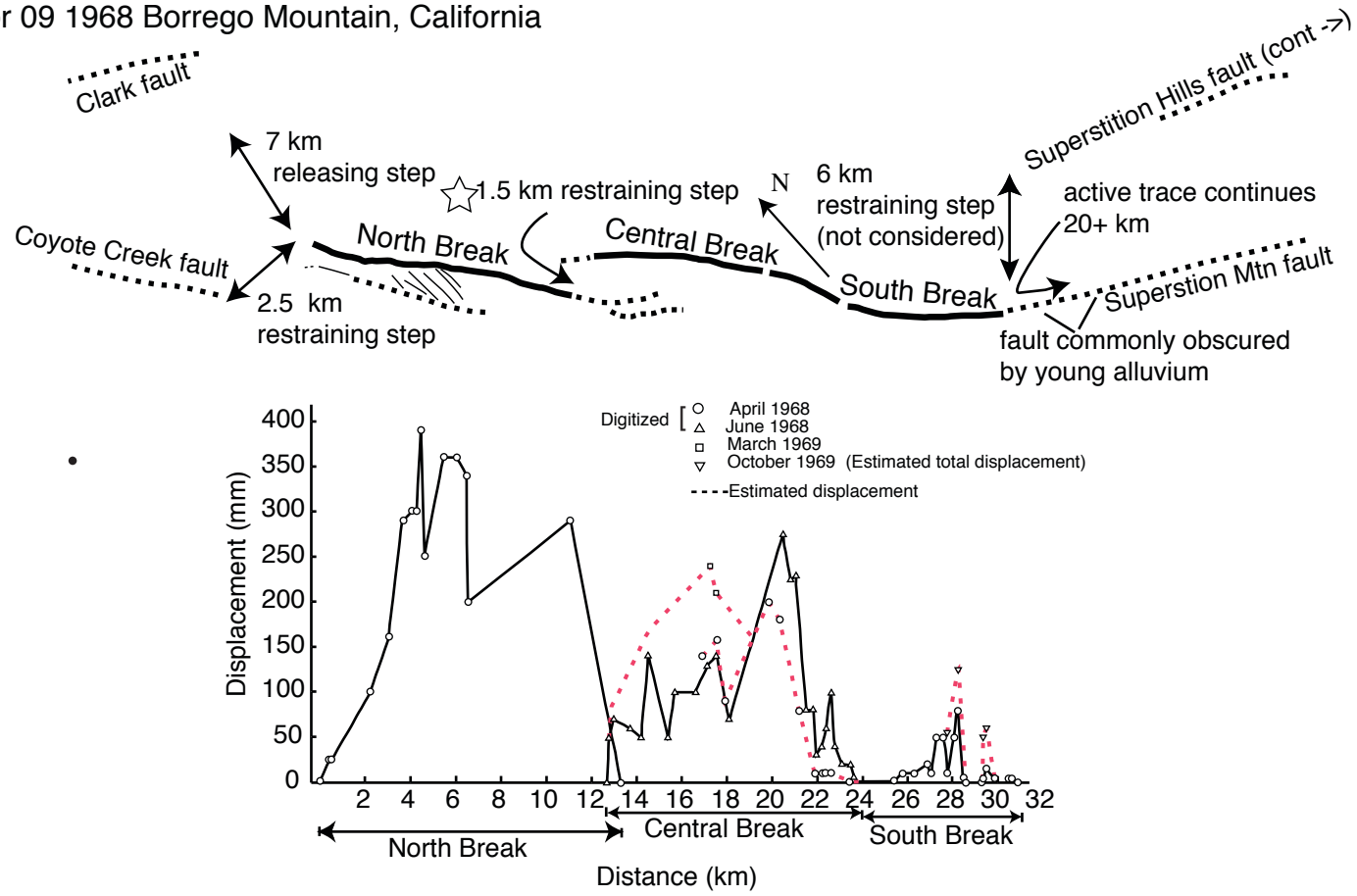

Feb 01, 1971, San Fernando, CA

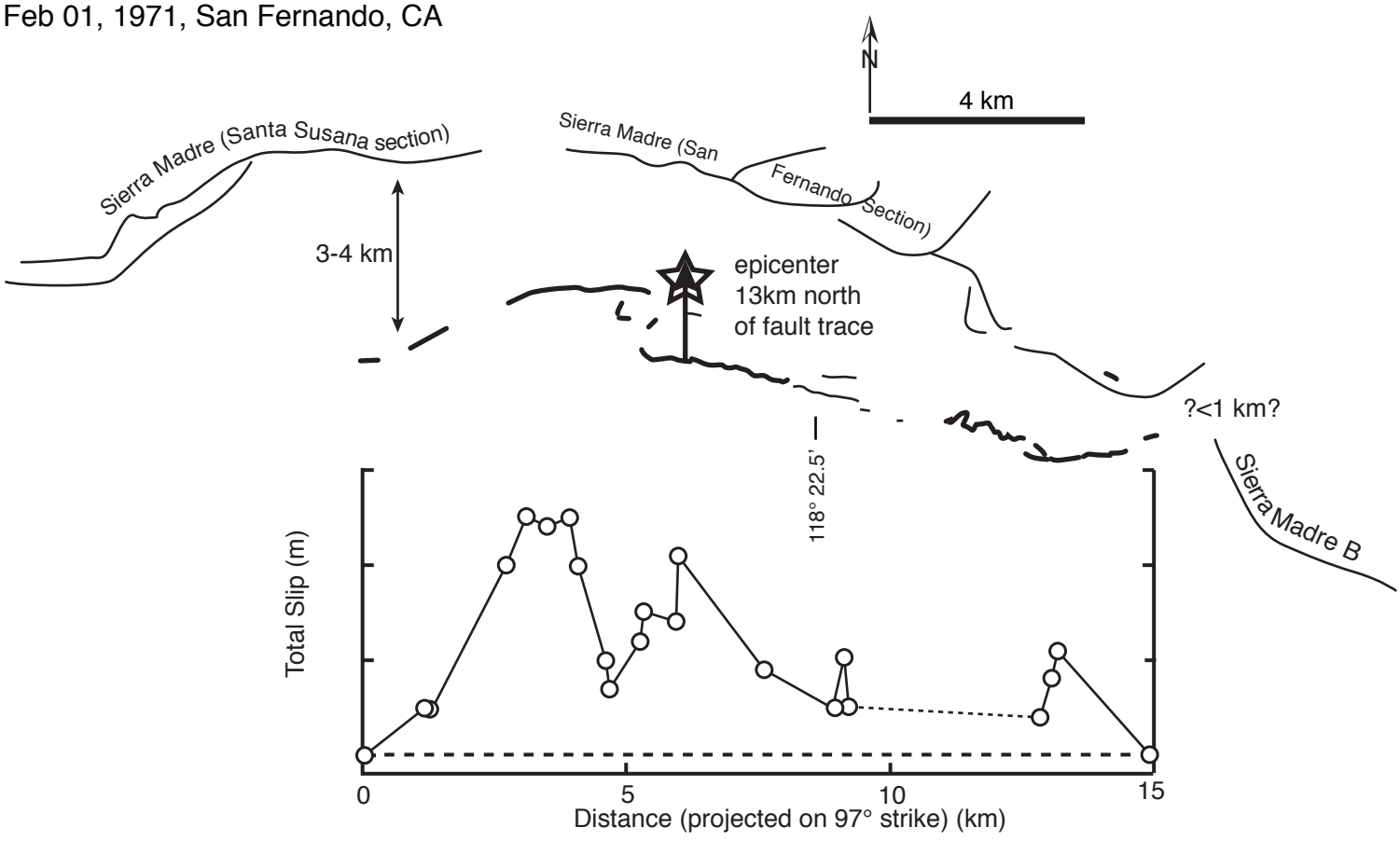

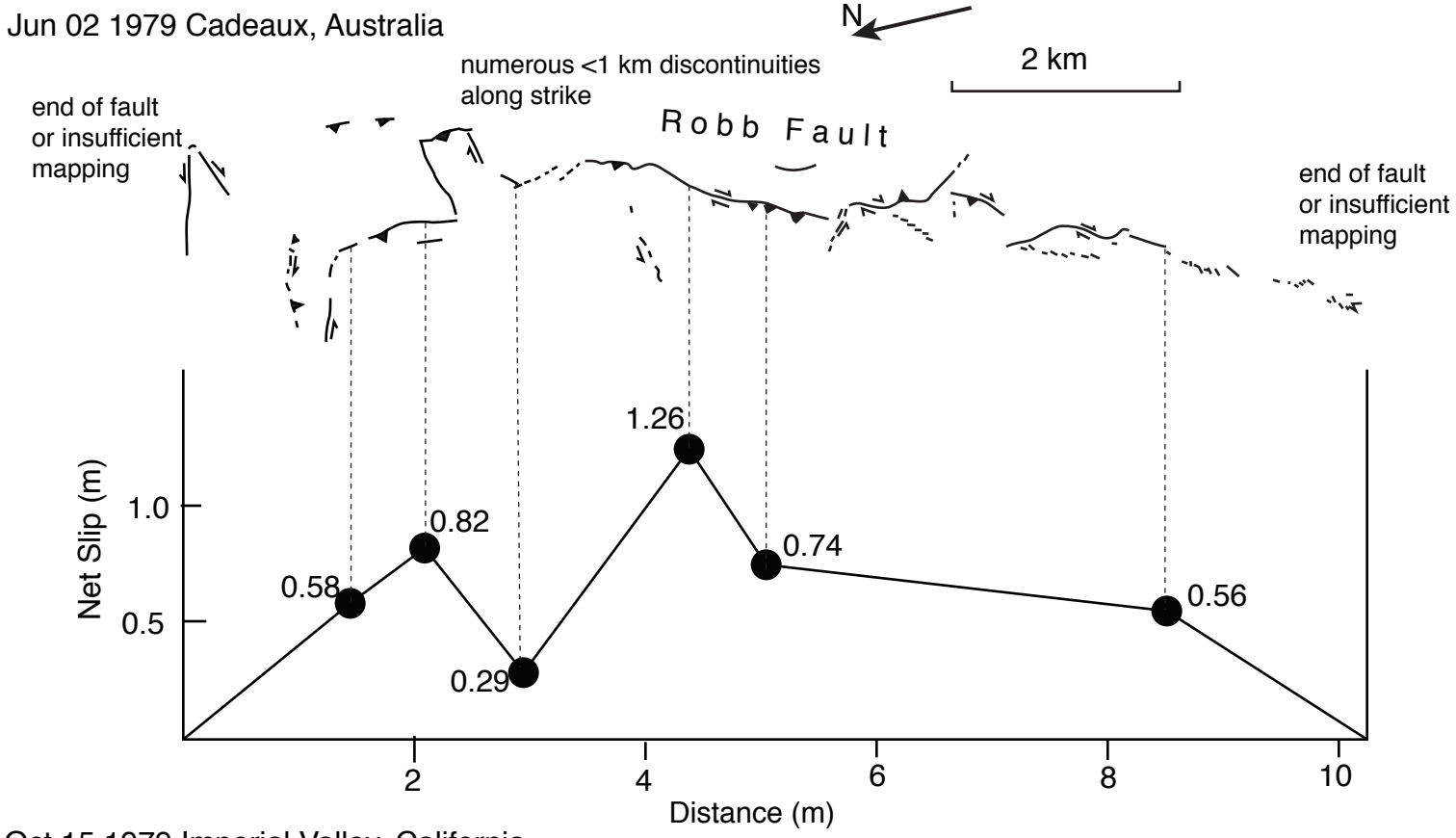
Jun 02 1979 Cadeaux, Australia
N
2 km
numerous <1 km discontinuities
along strike
Robb Fault
end of fault
or insufficient
mapping
end of fault
or insufficient
mapping
Net Slip (m)
1.0
0.5
0.58
0.82
0.29
1.26
0.74
0.56
2
4
6
8
10
Distance (m)

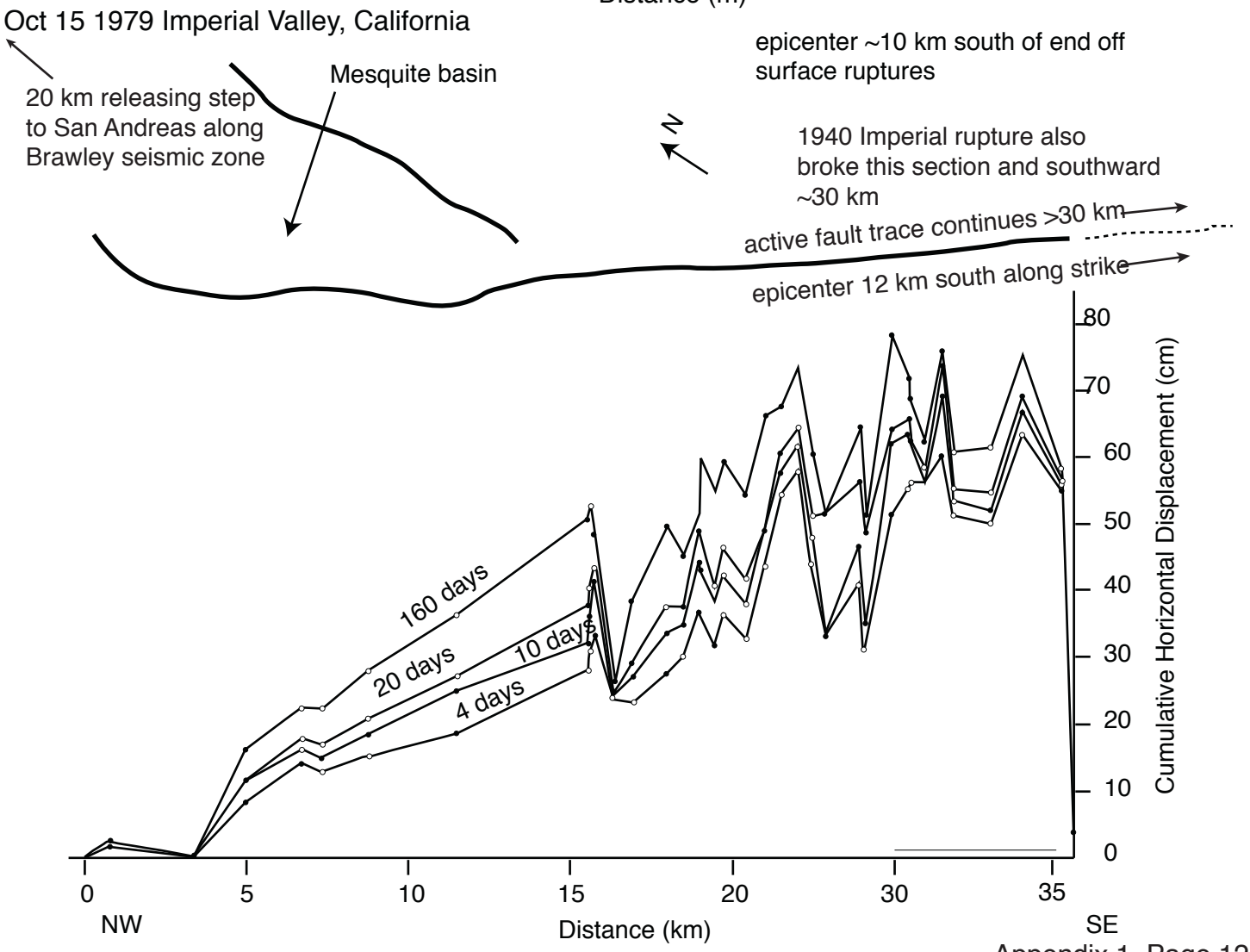
Oct 15 1979 Imperial Valley, California
epicenter ~10 km south of end off
surface ruptures
20 km releasing step
to San Andreas along
Brawley seismic zone
Mesquite basin
N
1940 Imperial rupture also
broke this section and southward
~30 km
active fault trace continues >30 km
epicenter 12 km south along strike
160 days
20 days
10 days
4 days
Cumulative Horizontal Displacement (cm)
80
70
60
50
40
30
20
10
0
0
5
10
15
20
30
35
NW
Distance (km)
SE

Oct 10, 1980 El Asnam, Algeria

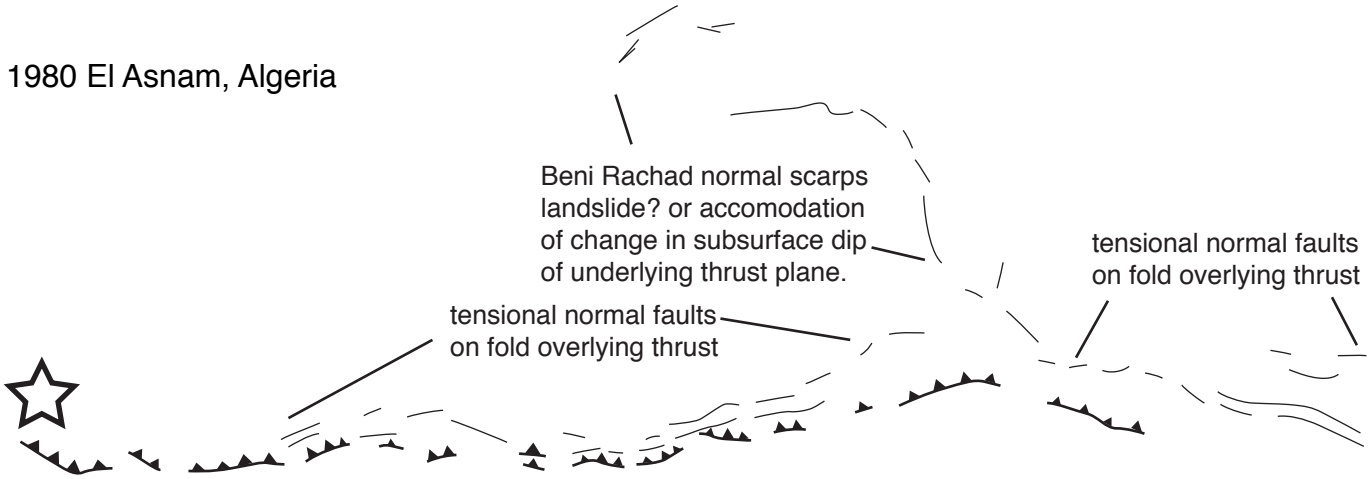

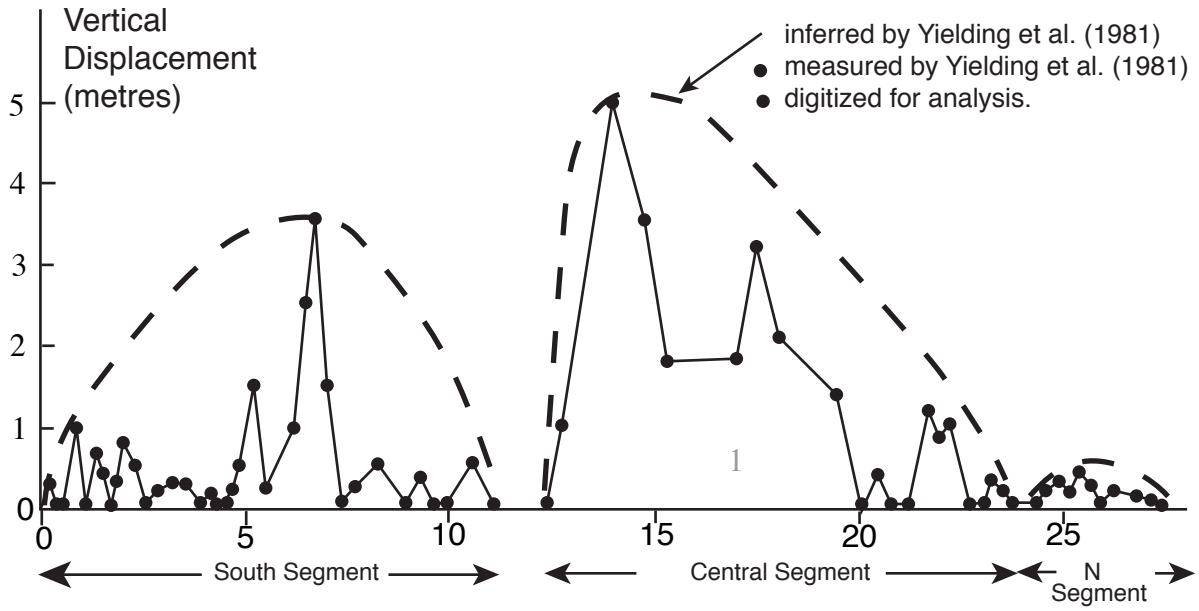

Oct 28 1983 Borah Peak, Idaho

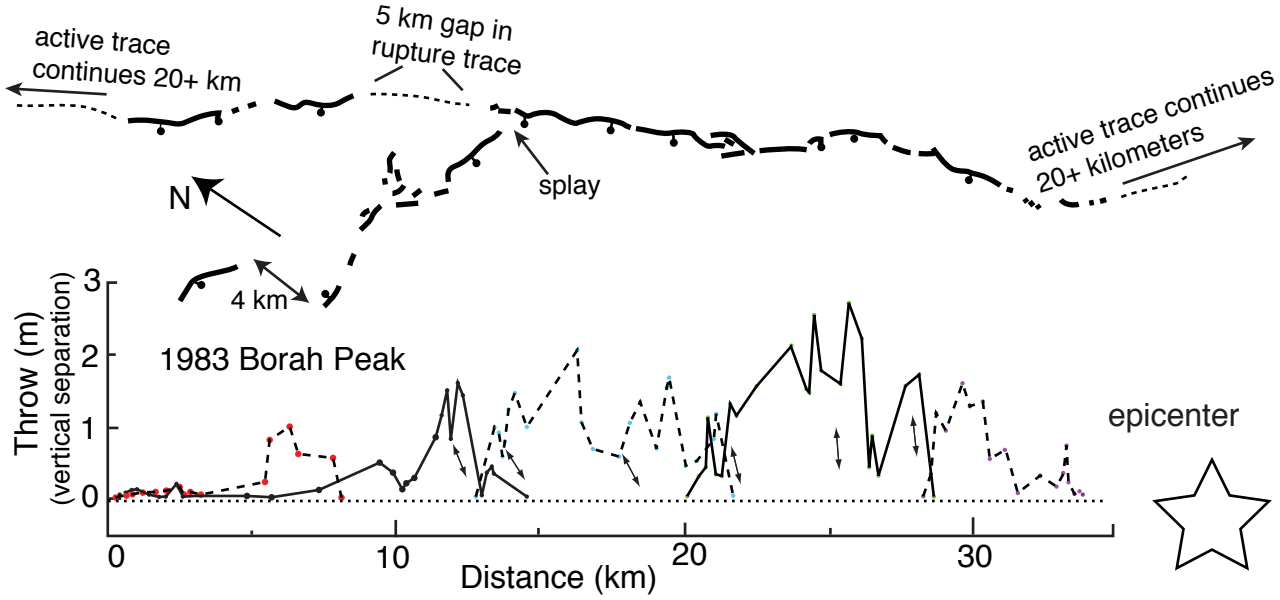

Mar 03 1986 Marryat, Australia

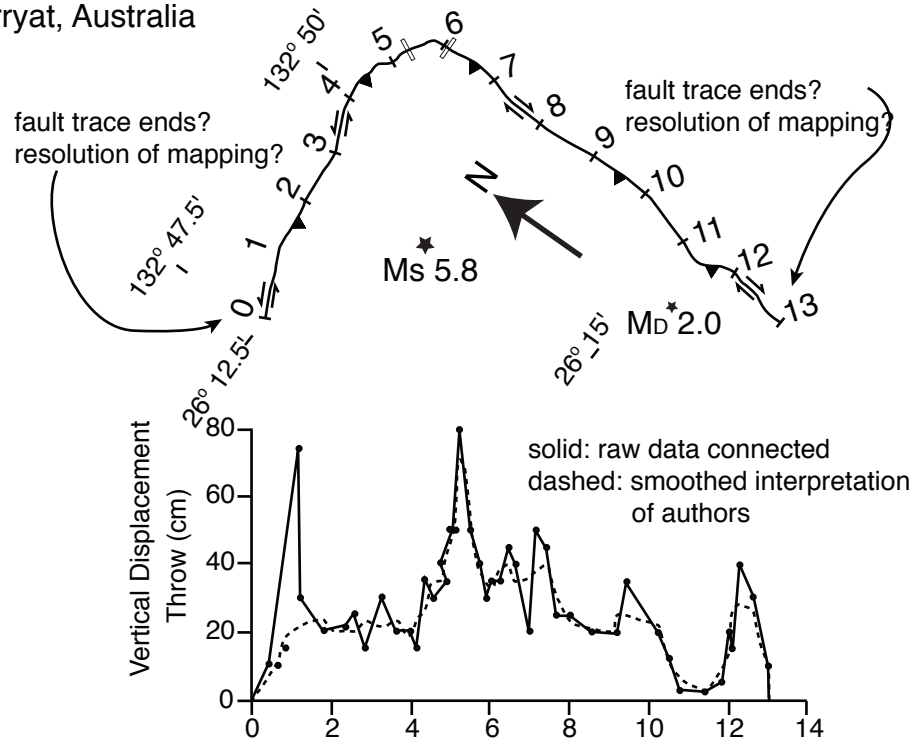

Mar 02 1987 Edgecumbe, New Zealand

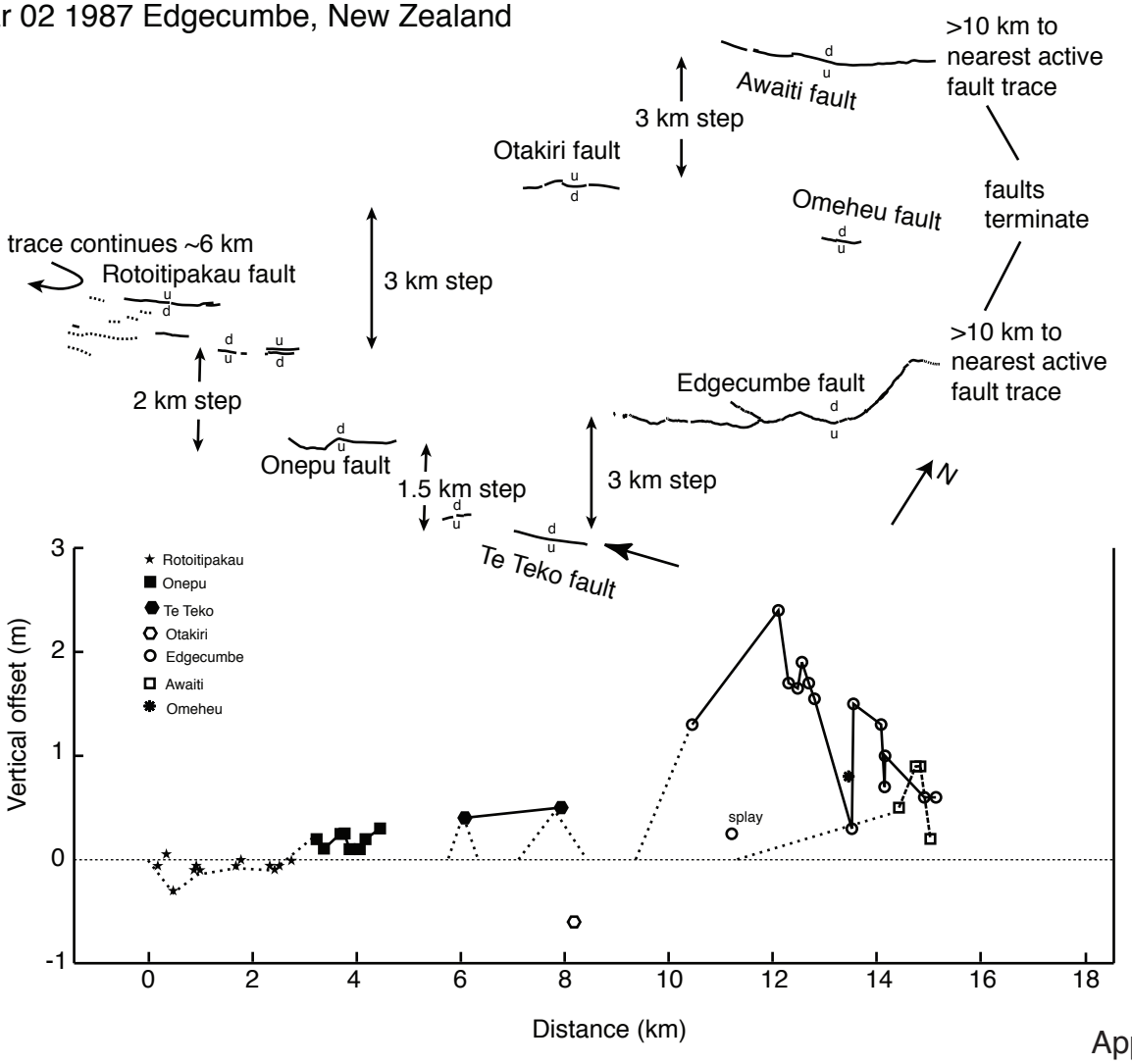

Nov 23 1987 Superstition Hills, California

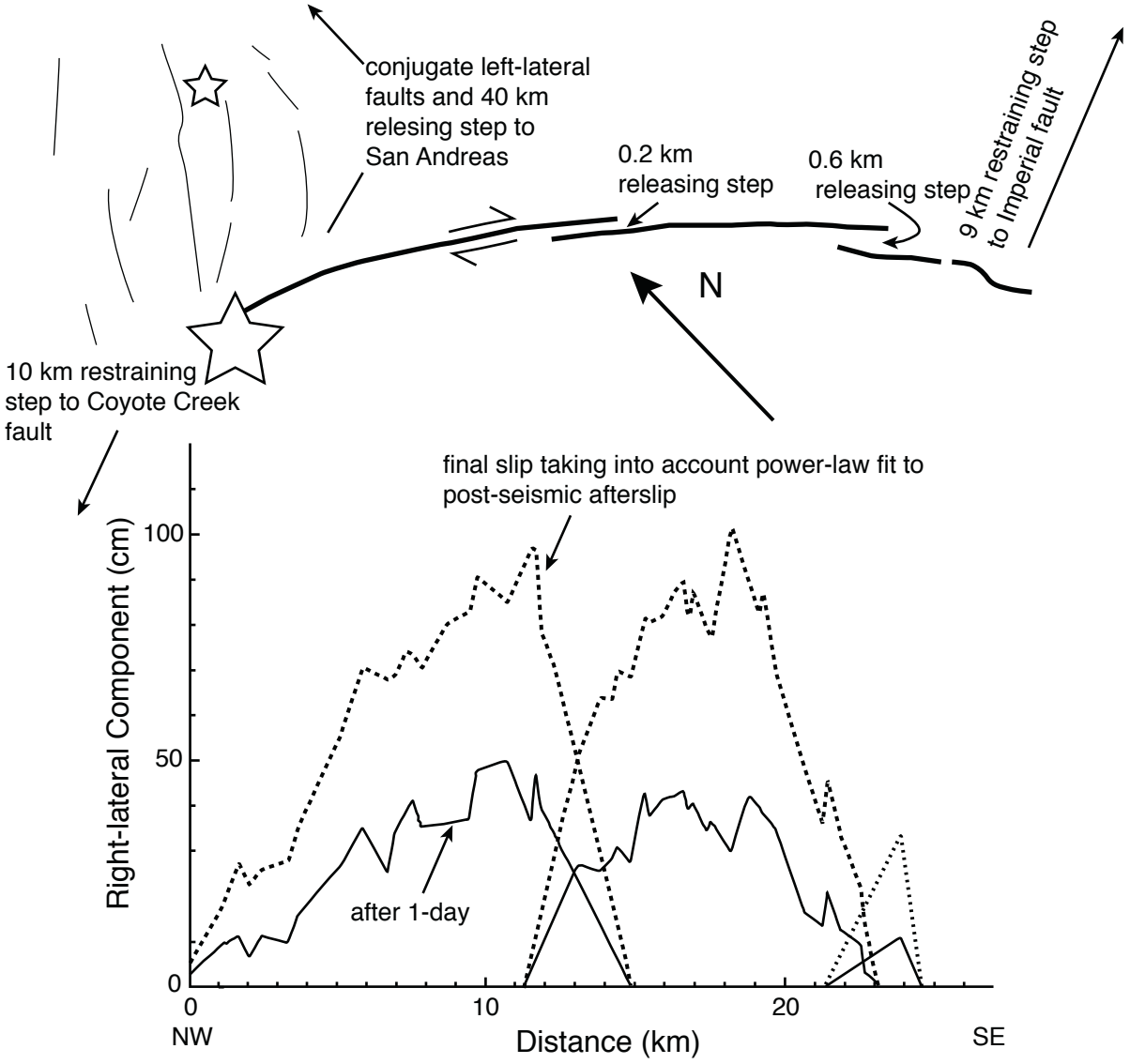

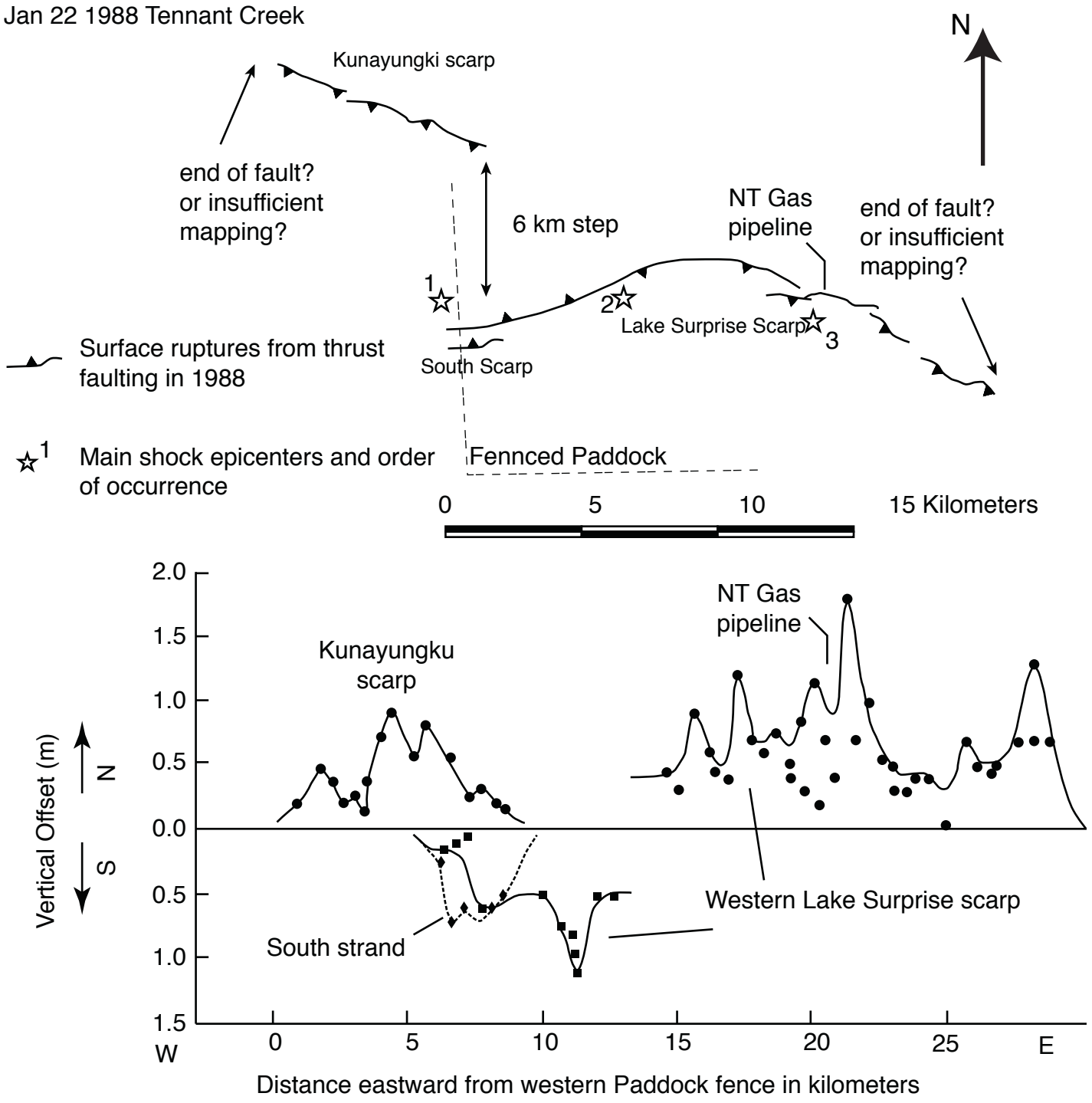
Jan 22 1988 Tennant Creek
N
Kunayungki scarp
end of fault?
or insufficient
mapping?
6 km step
NT Gas
pipeline
end of fault?
or insufficient
mapping?
1
2
3
Lake Surprise Scarp
South Scarp
Surface ruptures from thrust
faulting in 1988
Main shock epicenters and order
of occurrence
Fennced Paddock
0
5
10
15 Kilometers
2.0
1.5
1.0
0.5
0.0
0.5
1.0
1.5
Vertical Offset (m)
N
S
Kunayungku
scarp
NT Gas
pipeline
Western Lake Surprise scarp
South strand
W
0
5
10
15
20
25
E
Distance eastward from western Paddock fence in kilometers

Jul 16 1990 Luzon, Philippines

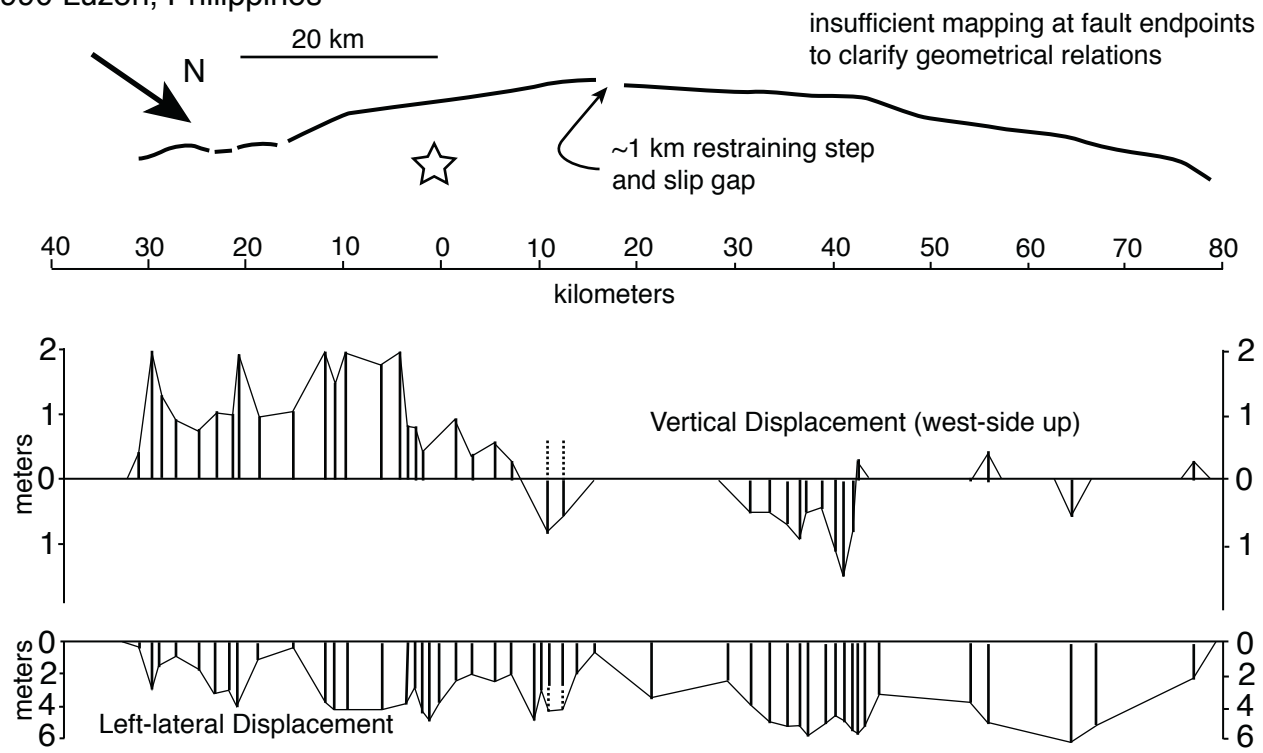

Jun 28 1992 Landers, California

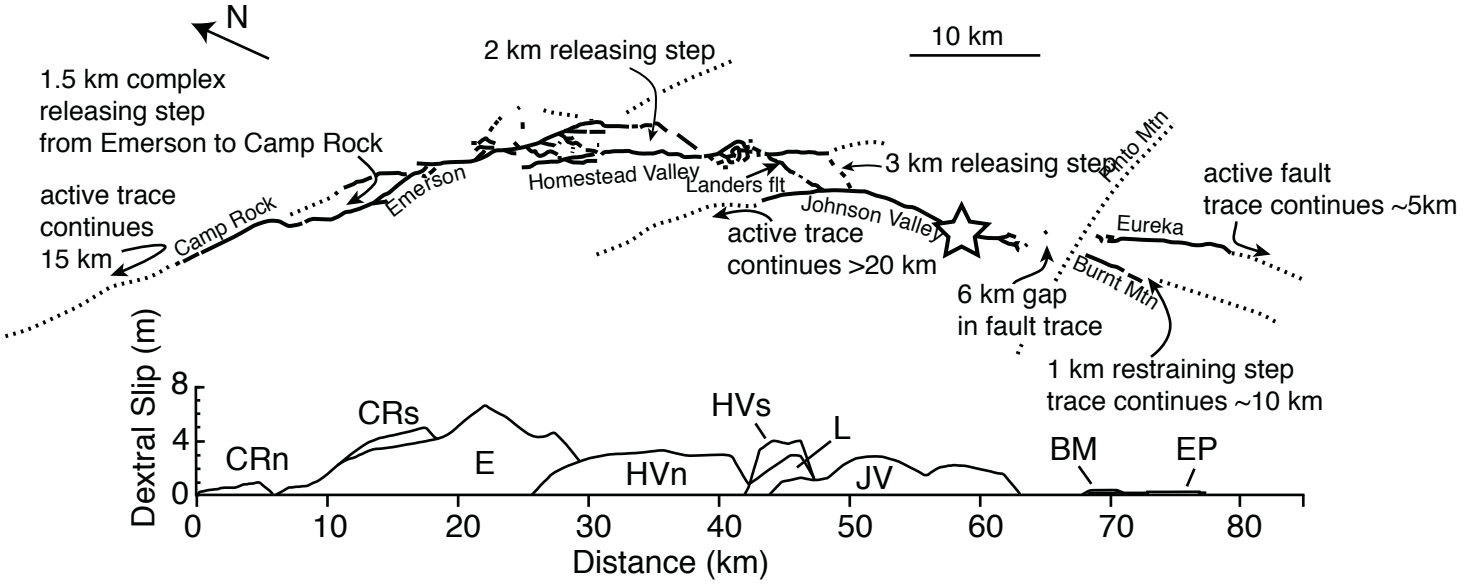

1998 March 14 Fandoqa (hachured lines) and 1981 July 29 Sirch Earthquake Fault (solid lines), Iran

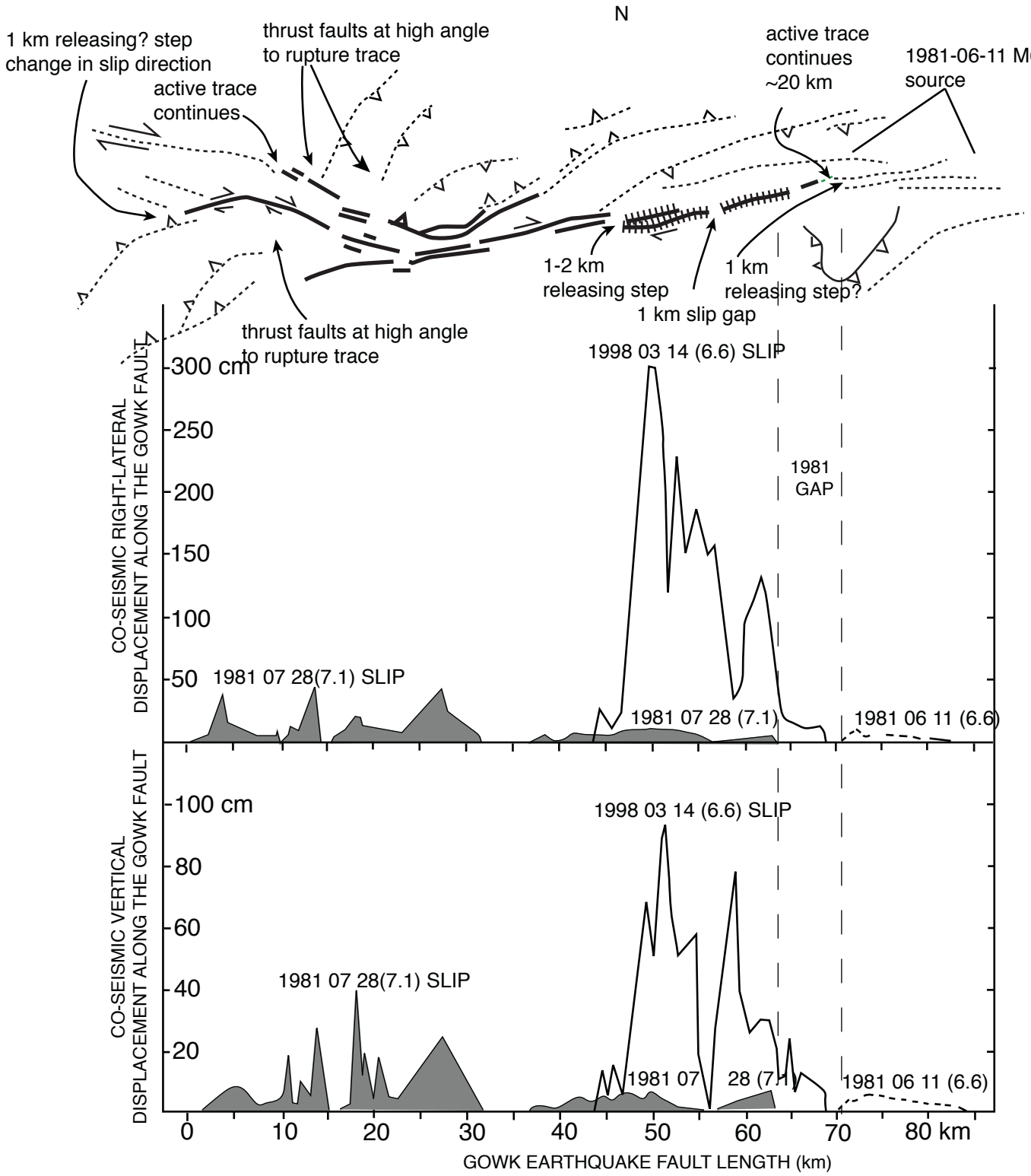

Sep 21 1999 Chi-Chi, Taiwan

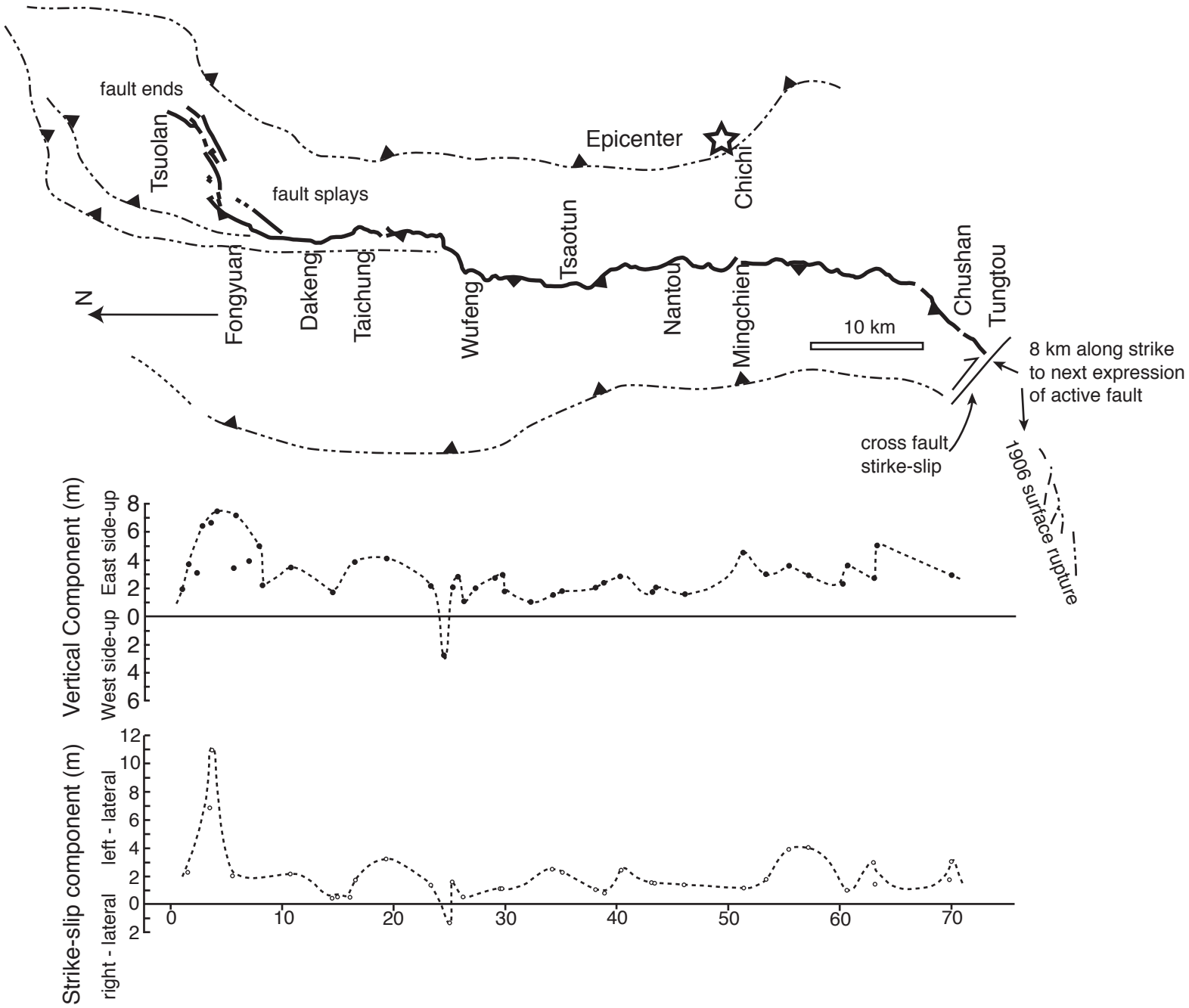

Nov 12 1999 Duzce, Turkey

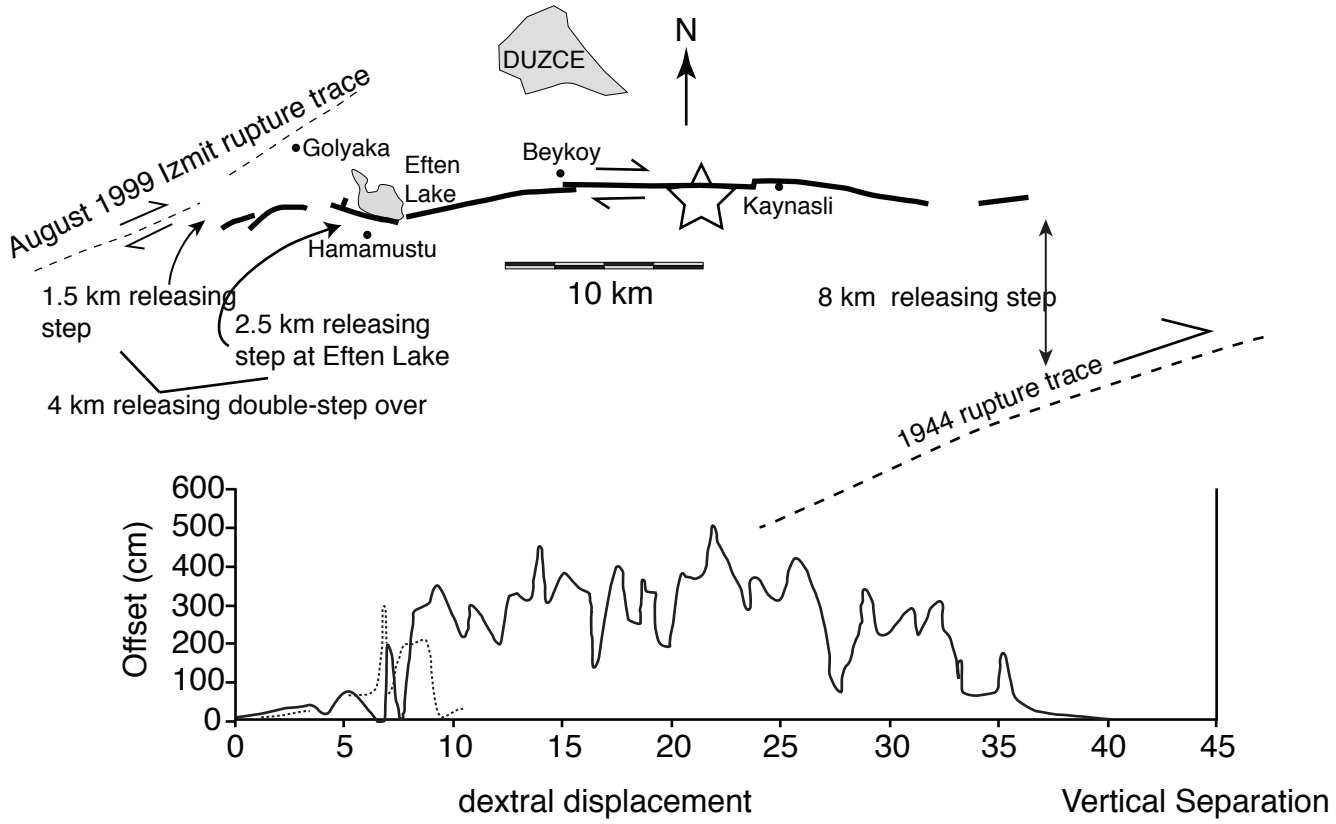

Aug 17 1999 Izmit, Turkey

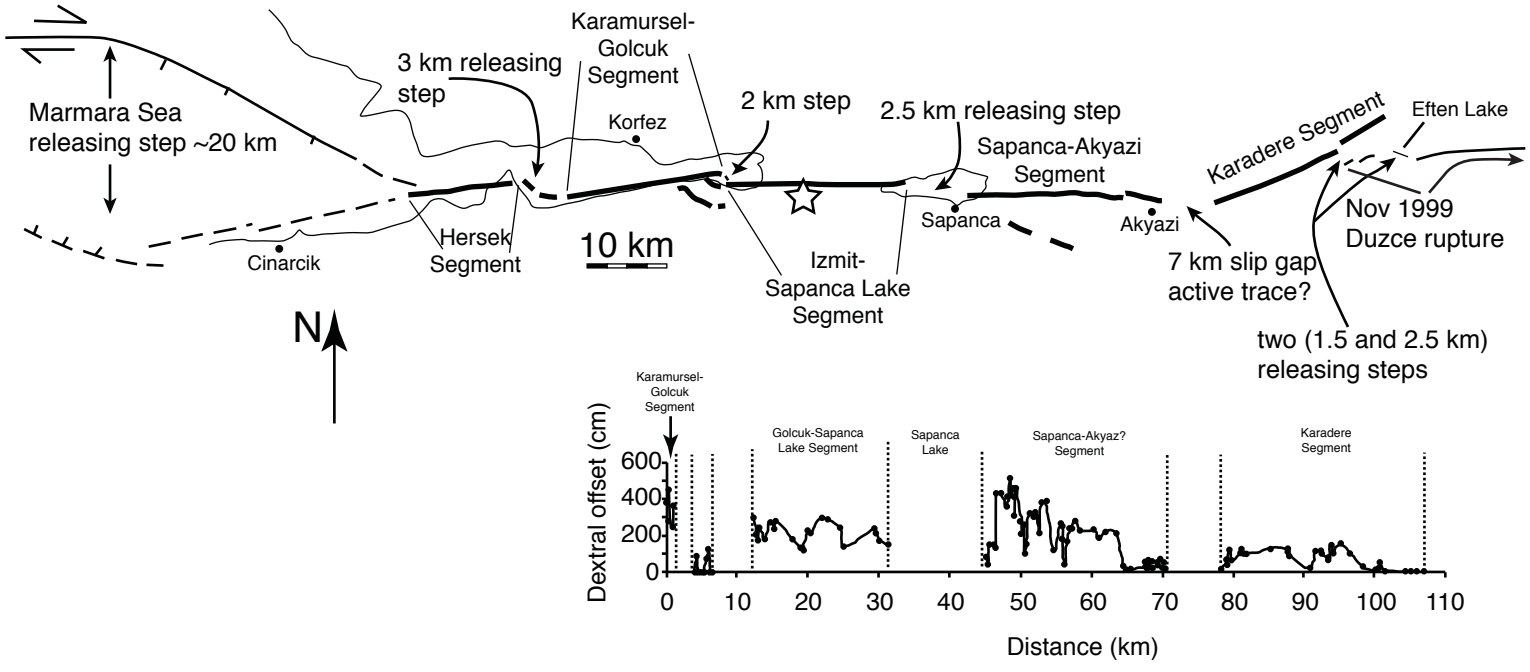

Oct 16 1999, Hector Mine, California

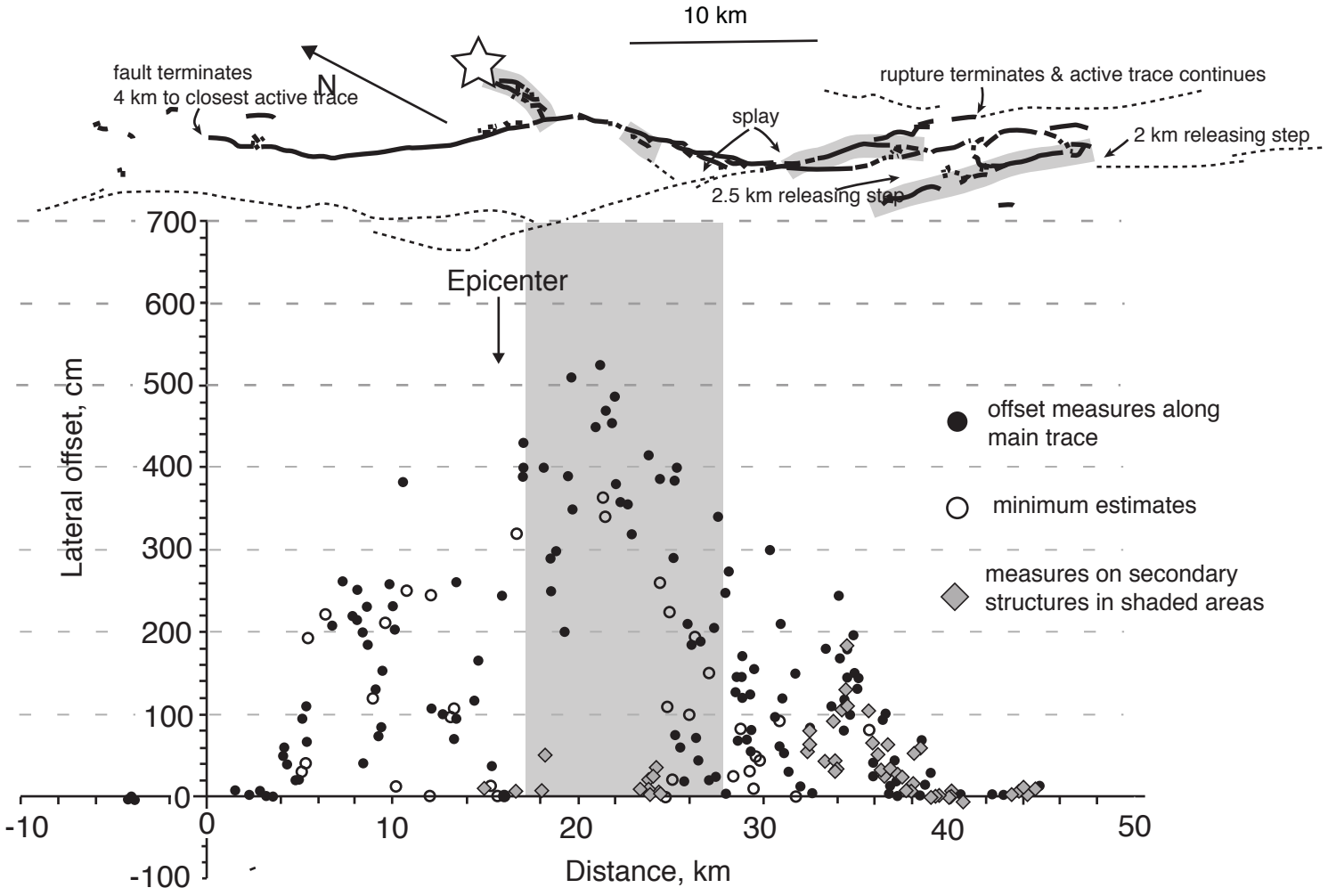

Nov 14, 2001 Kunlun, China

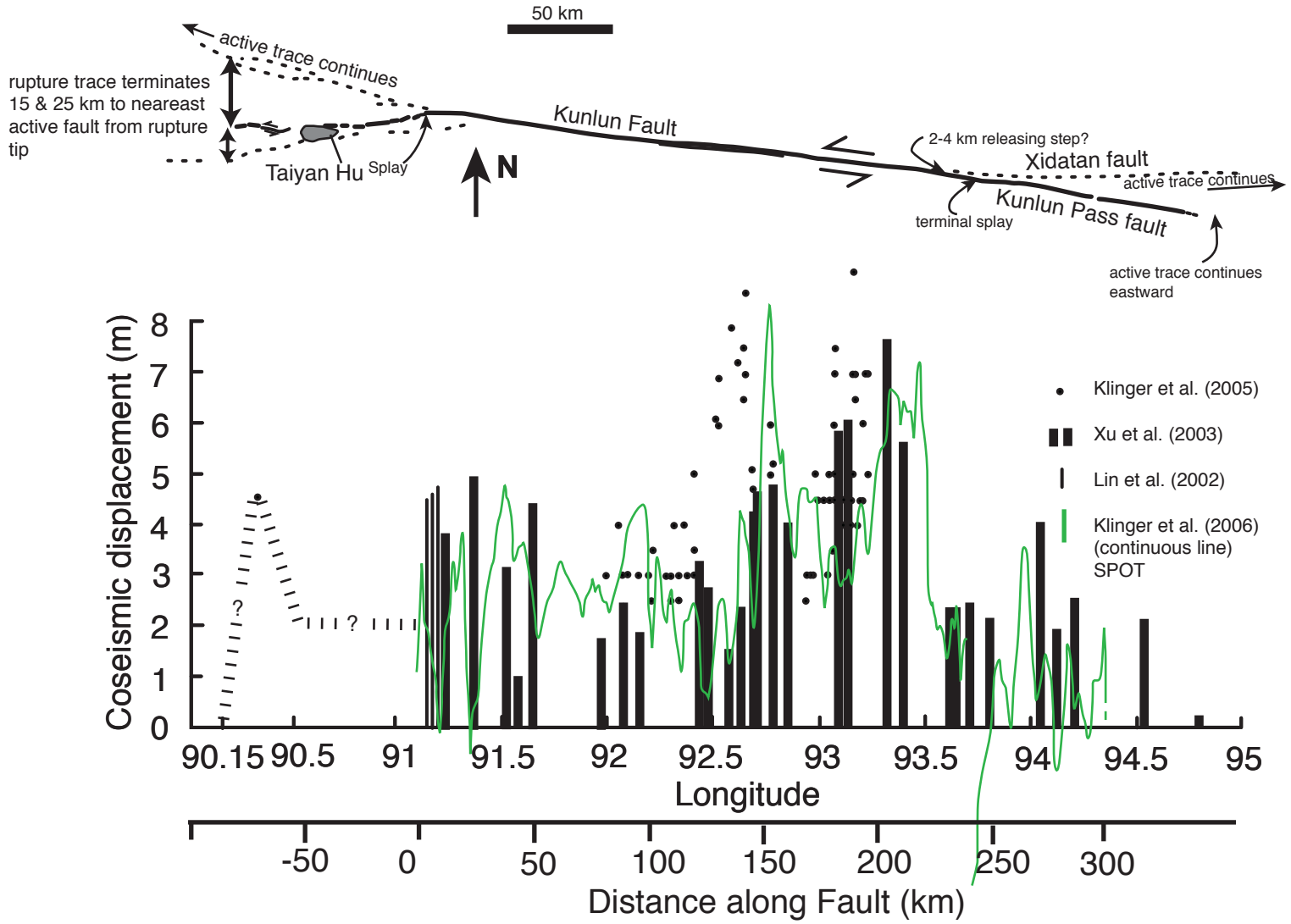

Nov 3 2002 Denali, Alaska

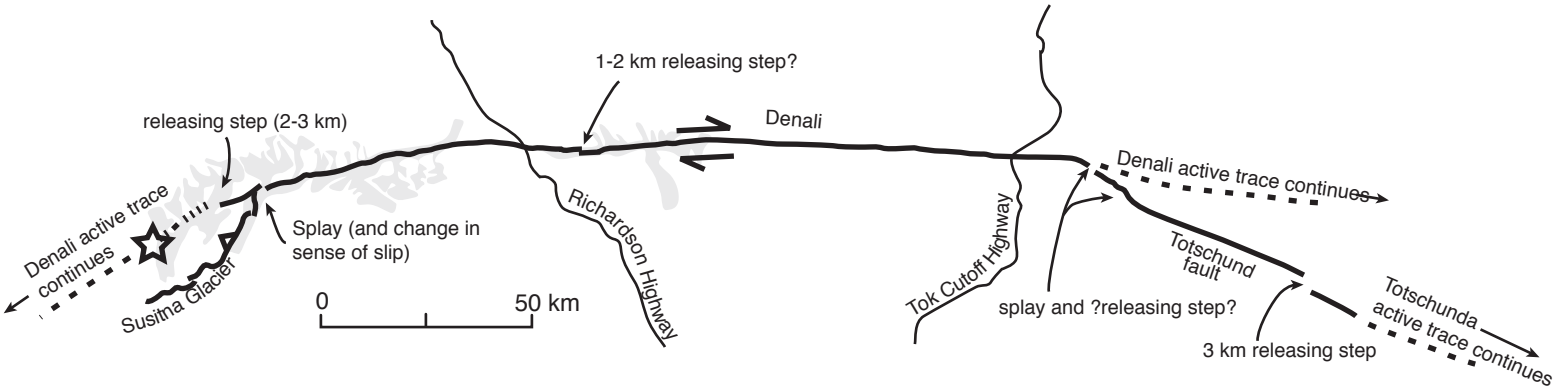

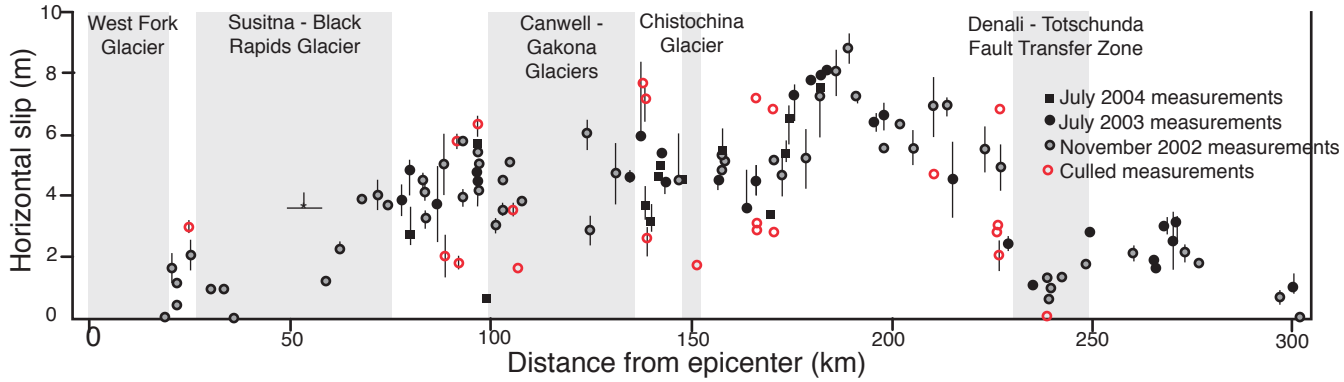

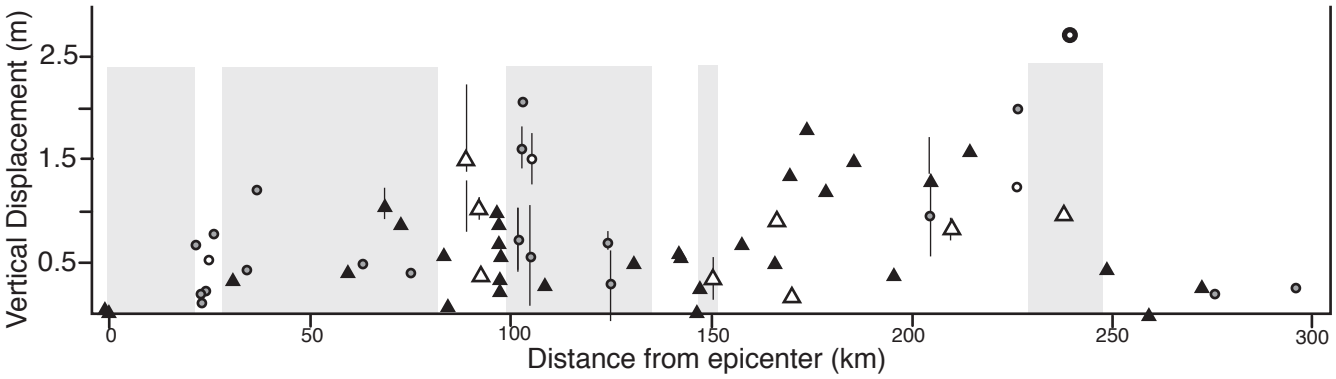

Example of Digitized Slip Distributions

Appendix 2
(anticipate that this will be provided as electronic supplement for all earthquakes)

of

Displacement and Geometrical Characteristics of Earthquake Surface Ruptures: Issues and Implications for Seismic Hazard Analysis and Process of Earthquake Rupture.

Steven G. Wesnousky
Center for Neotectonic Studies
Mail Stop 169
University of Nevada, Reno
Reno, Nevada 89557
stevew@seismo.unr.edu

2002 Nov 3 Denali (Haessler et al)

distance(km) Interpolated	slipHorizontal(m) Interpolated	slipVertical(m) Interpolated	slipTotal (sqrt(a*a+b*b)) Interpolated	distance(km) digitized	Slip Horizontal(m) digitized	distance(km) digitized	Slip Vertica
0.0000	0.021117	0.0058804	0.021921	-0.0	0.021110	-0.14164	0.00278
0.10000	0.021124	0.0089764	0.022952	18.670	0.022418	21.409	0.66999
0.20000	0.021131	0.012072	0.024337	20.585	1.6684	22.686	0.19025
0.30000	0.021138	0.015168	0.026017	21.702	0.46013	23.005	0.10302
0.40000	0.021145	0.018264	0.027941	21.862	1.1685	23.963	0.21520
0.50000	0.021152	0.021360	0.030061	25.372	2.0854	24.602	0.52053
0.60000	0.021159	0.024457	0.032339	30.319	0.98156	25.879	0.77602
0.70000	0.021166	0.027553	0.034744	33.670	0.96096	30.668	0.31505
0.80000	0.021173	0.030649	0.037251	36.064	0.023626	34.180	0.42106
0.90000	0.021180	0.033745	0.039841	53.777	3.6290	36.734	1.2062
1.0000	0.021187	0.036841	0.042498	59.043	1.2335	59.402	0.39673
1.1000	0.021194	0.039937	0.045212	62.553	2.2963	63.233	0.48406
1.2000	0.021201	0.043033	0.047972	67.979	3.9008	68.661	1.0450
1.3000	0.021208	0.046129	0.050770	71.968	4.0469	72.651	0.85813
1.4000	0.021215	0.049225	0.053601	74.521	3.7138	75.206	0.39711
1.5000	0.021221	0.052321	0.056461	77.872	3.8807	83.347	0.55307
1.6000	0.021228	0.055417	0.059343	79.787	4.8600	84.305	0.05462
1.7000	0.021235	0.058513	0.062247	80.266	2.7559	88.934	1.4941
1.8000	0.021242	0.061609	0.065168	83.138	4.5269	91.967	1.0144
1.9000	0.021249	0.064705	0.068105	83.617	4.1519	92.606	0.36013
2.0000	0.021256	0.067801	0.071055	83.936	3.2978	96.597	0.98331
2.1000	0.021263	0.070897	0.074017	86.809	3.7355	97.076	0.85870
2.2000	0.021270	0.073993	0.076989	88.404	5.0689	97.275	0.67178
2.3000	0.021277	0.077089	0.079971	93.191	5.7984	97.395	0.55340
2.4000	0.021284	0.080185	0.082961	93.351	3.9651	97.554	0.32910
2.5000	0.021291	0.083281	0.085959	96.502	5.7362	97.714	0.21071
2.6000	0.021298	0.086377	0.088964	96.702	5.4445	101.86	0.71551
2.7000	0.021305	0.089473	0.091974	96.843	4.7987	102.66	1.6003
2.8000	0.021312	0.092569	0.094990	96.952	4.5070	103.14	2.0552
2.9000	0.021319	0.095665	0.098011	97.081	5.0695	104.90	0.55358
3.0000	0.021326	0.098761	0.10104	97.281	4.2154	105.38	1.5069
3.1000	0.021333	0.10186	0.10407	101.33	3.0490	108.57	0.26705
3.2000	0.021340	0.10495	0.10710	103.08	3.5491	124.21	0.69111
3.3000	0.021346	0.10805	0.11014	104.04	4.5283	125.01	0.28613
3.4000	0.021353	0.11114	0.11318	105.00	5.1118	130.76	0.47942
3.5000	0.021360	0.11424	0.11622	107.87	3.8411	141.77	0.57937
3.6000	0.021367	0.11734	0.11927	124.15	6.0714	142.57	0.53578
3.7000	0.021374	0.12043	0.12232	124.95	2.9048	146.24	0.00624
3.8000	0.021381	0.12353	0.12537	131.17	4.7802	147.20	0.23680
3.9000	0.021388	0.12663	0.12842	134.84	4.6347	150.39	0.33657
4.0000	0.021395	0.12972	0.13147	137.55	5.9682	157.58	0.66698
4.1000	0.021402	0.13282	0.13453	138.67	3.7183	165.72	0.48024

Curve Fits to Digitized Slip Distributions

Appendix 3

of

Displacement and Geometrical Characteristics of Earthquake Surface Ruptures: Issues and Implications for Seismic Hazard Analysis and Process of Earthquake Rupture.

Steven G. Wesnousky
Center for Neotectonic Studies
Mail Stop 169
University of Nevada, Reno
Reno, Nevada 89557
stevew@seismo.unr.edu

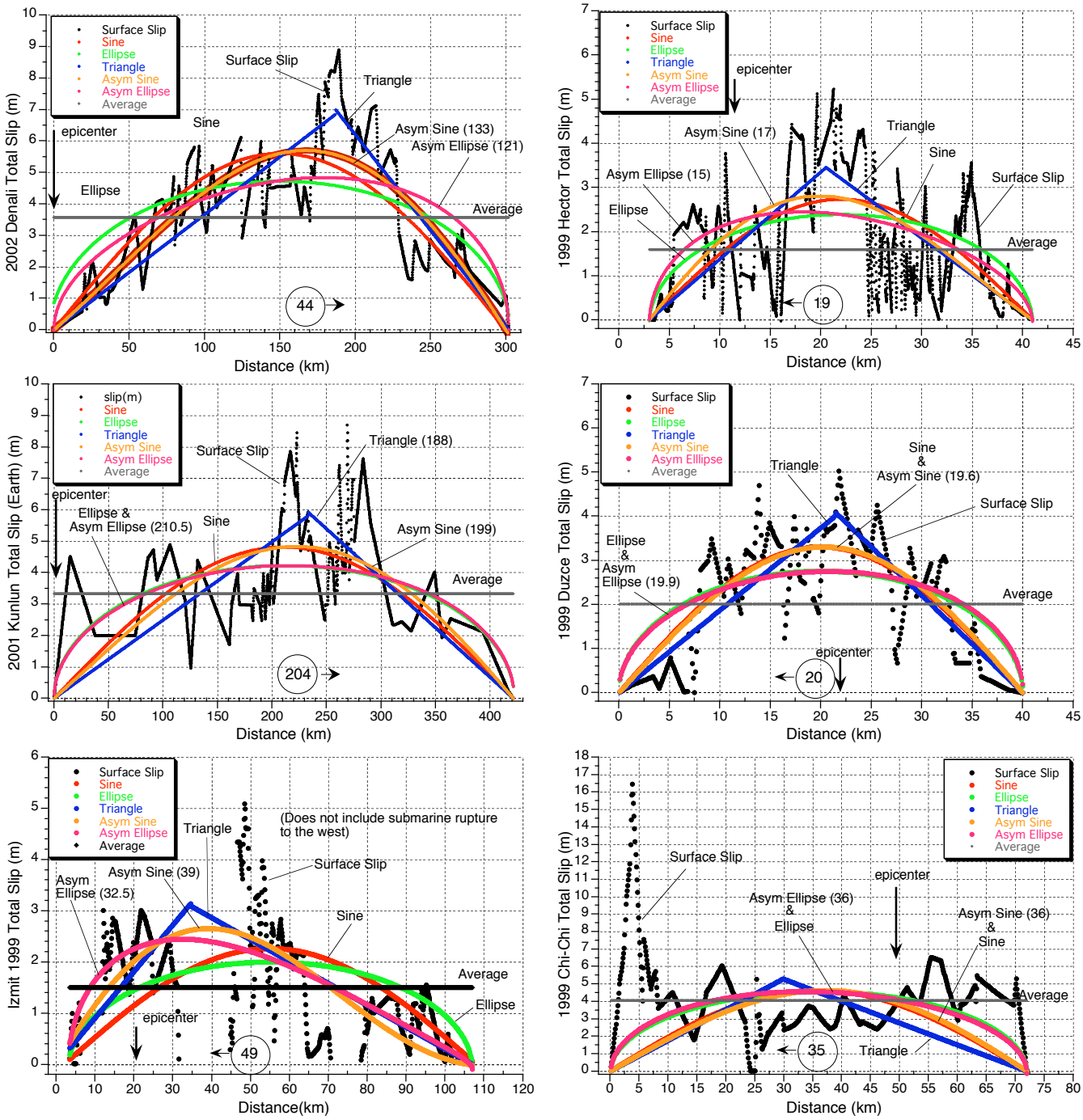

Figure A3-1. Digitized surface slip distributions of earthquakes listed in Table 1 and various curve-fits to those distributions are arranged in reverse chronological order. Type of curve-fit is labeled and discussed in main text. Position of epicenter with respect to fault strike is when available labeled and indicated by downward pointing arrow. Integration of the digitized values of surface slip allows definition of a point where half the cumulative slip falls on either side. That value is defined for each slip distribution (value in circle) by the distance in km to nearest fault endpoint. Values in parenthesis are distances in km of nearest fault endpoint of peak of the asymetric sine and ellipse curves.

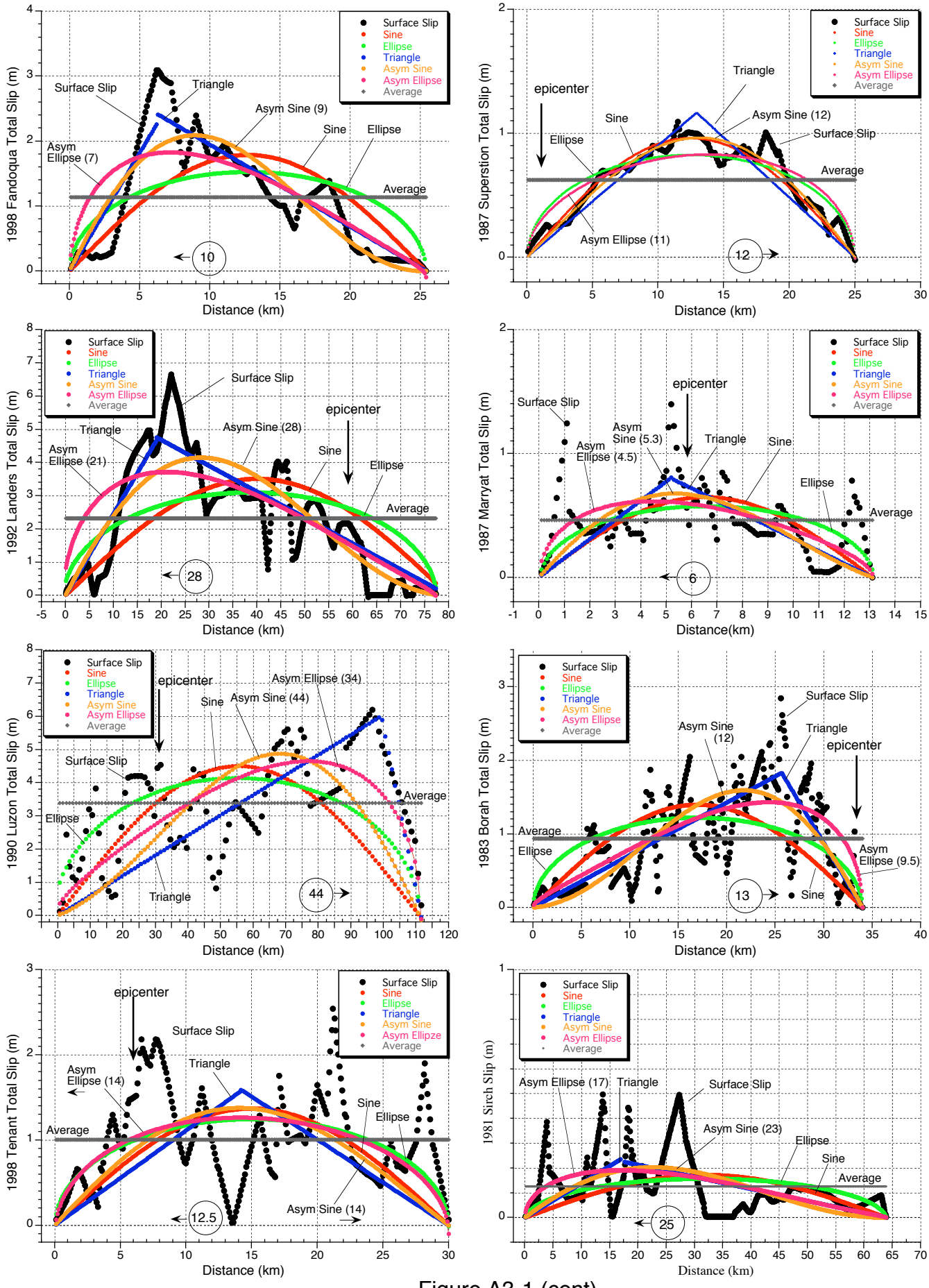

Figure A3-1 (cont)

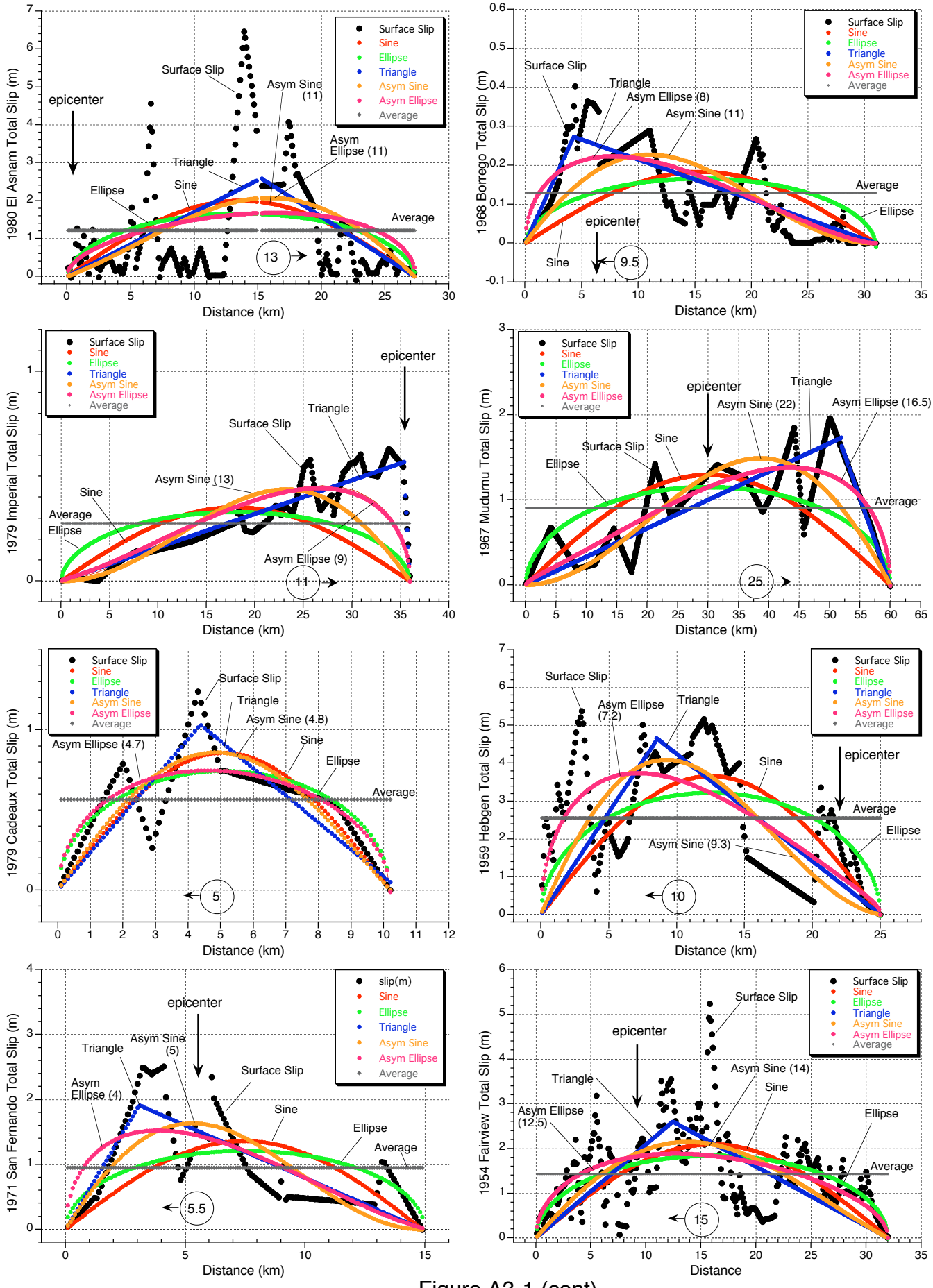

Figure A3-1 (cont)

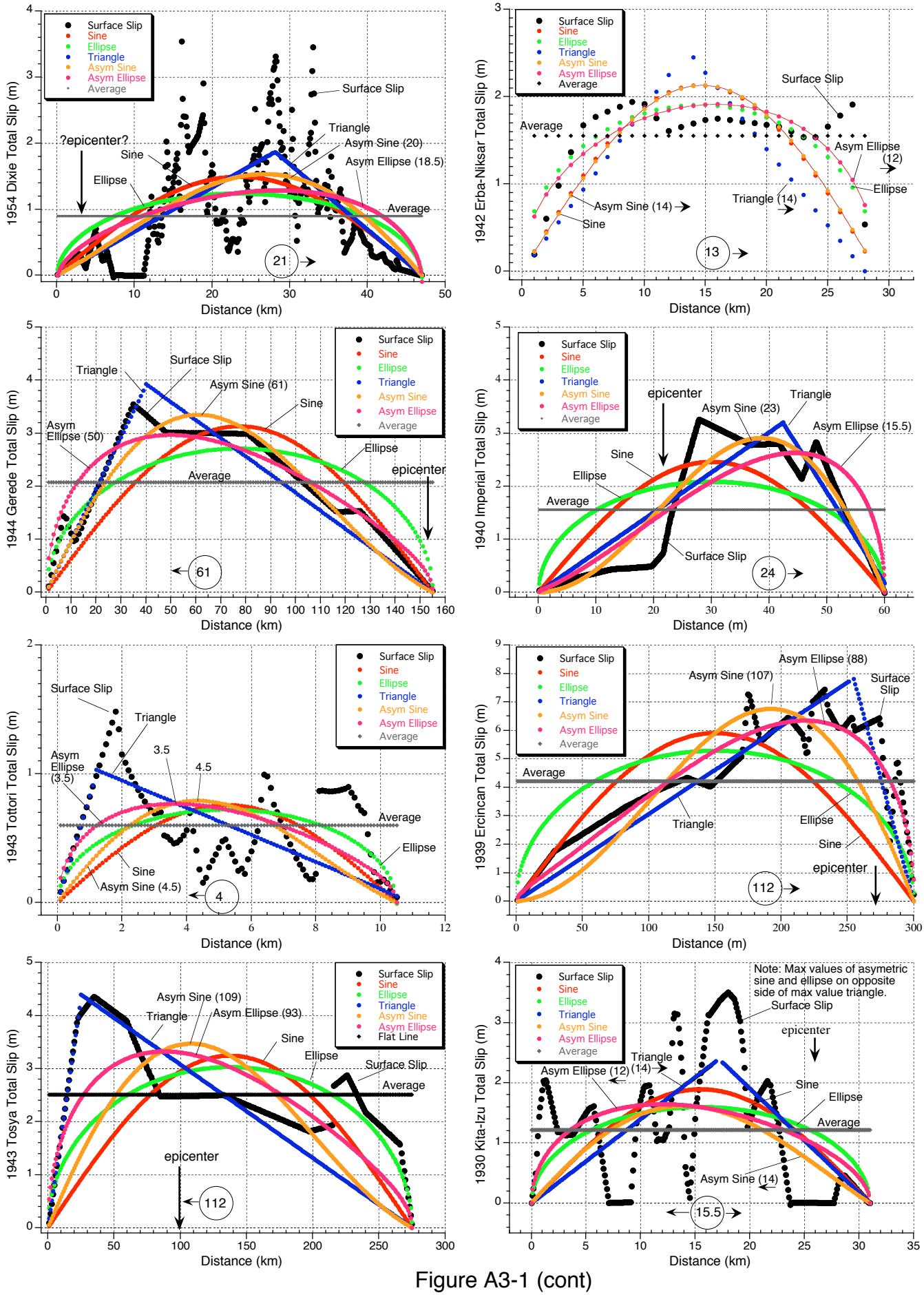

Figure A3-1 (cont)

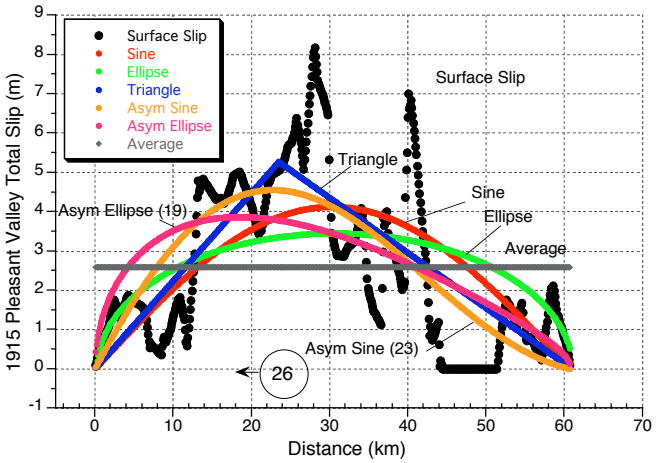

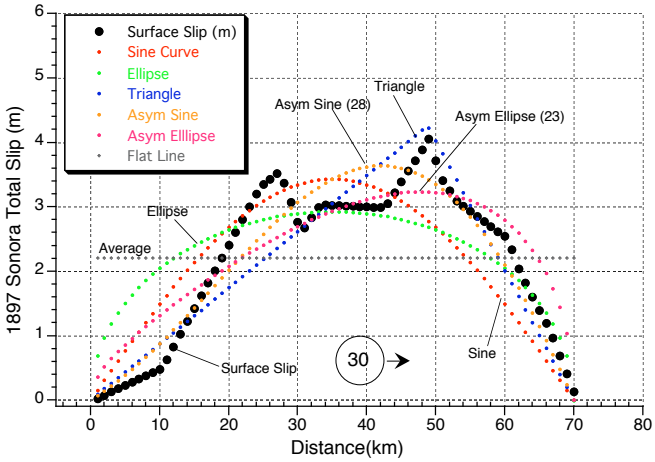

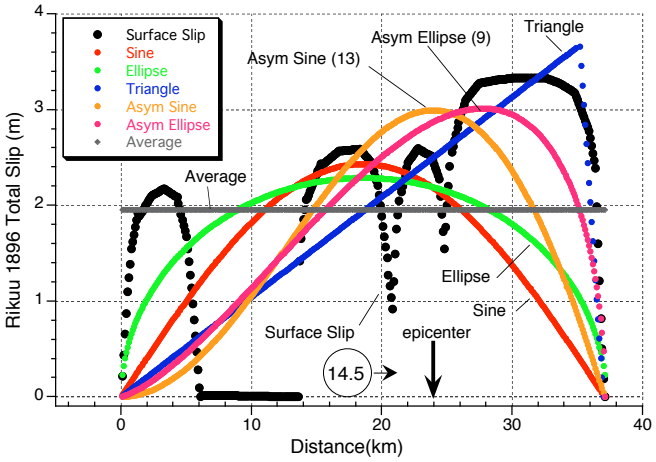

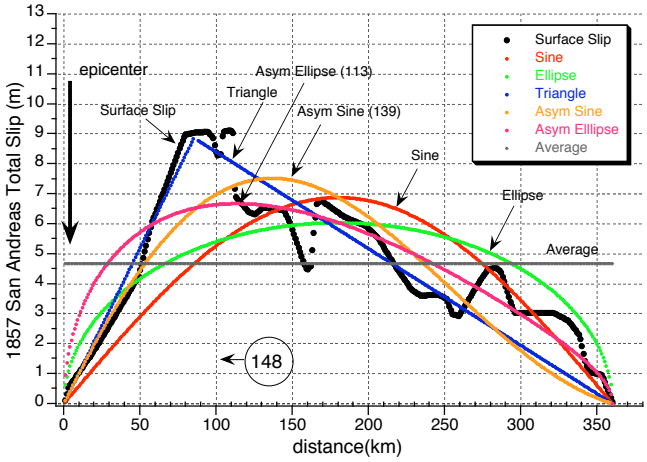

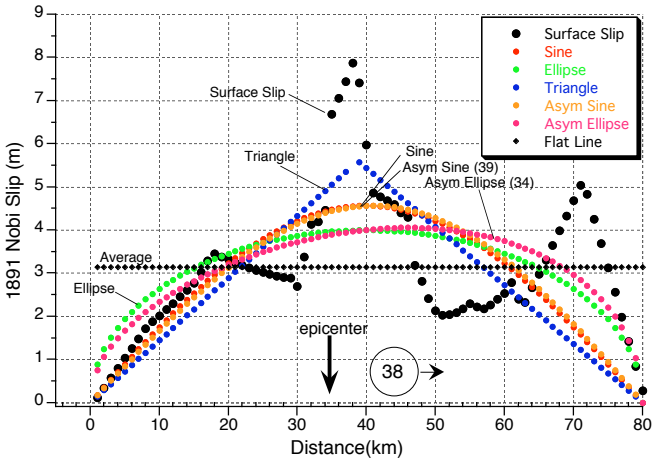

Figure A3-1 (cont)